FLORIDA INTERNATIONAL UNIVERSITY

Miami, Florida

A PRECISE MEASUREMENT OF THE TWO-PHOTON EXCHANGE EFFECT

A dissertation submitted in partial fulfillment of the

requirements for the degree of

DOCTOR OF PHILOSOPHY

in

PHYSICS

by

Maryam Moteabbed

2009

To: Dean Kenneth Furton
College of Arts and Sciences

This dissertation, written by Maryam Moteabbed, and entitled A Precise Measurement of the Two-Photon Exchange Effect, having been approved in respect to style and intellectual content, is referred to you for judgment.

We have read this dissertation and recommend that it be approved.

Werner U. Boeglin

William K. Brooks

Misak Sargsian

Julian Edward

Brian A. Raue, Major Professor

Date of Defense: March 24, 2009

The dissertation of Maryam Moteabbed is approved.

Dean Kenneth Furton
College of Arts and Sciences

Dean George Walker
University Graduate School

Florida International University, 2009

DEDICATION

To my mom, my guardian angel...

ACKNOWLEDGMENTS

For this accomplishment, I am deeply grateful to my family, all my friends and professors for their continuous support and encouragement. I could never get this far without them.

First, I wish to thank my parents. Since I was a little girl, my father, Reza, has envisioned my success. He has taught me how to set my goals high and work hard to reach them. His love and support has followed me here, and helped me through, every step of the way. I cherish the memory of my mother, Mahnaz, who inspired me, taught me to be strong and independent. She embraced me with her love and gave me all that was there to give. I am who I am because of you, mom. Thank you!

I would like to thank the love of my life, my soulmate, and my best friend, Atilla, who has been there for me through many ups and downs. He has loved me unconditionally, and brought out the best in me. He has held me when I was not strong enough, and encouraged me to carry on. Thanks for all the wonderful times together, and for being my forever love!

Also, thanks to my brother, Ali, and my aunt, Mahasti, for their love and support. Thanks for sticking together in hard times and laughing together in happy times.

Many thanks to all my friends all over the world for bringing brightness and cheer throughout my life. Thanks for all the great times and for your timeless friendship.

I truly appreciate the help and support of my major professor, Dr. Brian Raue, who has guided me through my entire graduate career. He has taught me how to "think", and become a better scientist. He has inspired me to expand the range of my skills, and never be afraid of learning. Along the way, he has always been patient, understanding and caring. Thanks for being such a great advisor and for having confidence in my abilities.

Special thanks goes to the members of our collaboration, specially Dr. William Brooks and Dr. Lawrence Weinstein for their helpful suggestions and thoughtful guidance. Thanks to Dr. Werner Boeglin for sharing his knowledge when I most needed it. I also wish to express my gratitude to the remaining members of my dissertation committee Dr. Misak Sargsian and Dr. Julian Edward for their time and helpful comments.

The financial support for my research was provided by the Department of Energy grant.

ABSTRACT OF THE DISSERTATION

A PRECISE MEASUREMENT OF

THE TWO-PHOTON EXCHANGE EFFECT

by

Maryam Moteabbed

Florida International University, 2009

Miami, Florida

Professor Brian A. Raue, Major Professor

The two-photon exchange phenomenon is believed to be responsible for the discrepancy observed between the ratio of proton electric and magnetic form factors, measured by the Rosenbluth and polarization transfer methods. This disagreement is about a factor of three at Q^2 of 5.6 GeV^2. The precise knowledge of the proton form factors is of critical importance in understanding the structure of this nucleon. The theoretical models that estimate the size of the two-photon exchange (TPE) radiative correction are poorly constrained. This factor was found to be directly measurable by taking the ratio of the electron-proton and positron-proton elastic scattering cross sections, as the TPE effect changes sign with respect to the charge of the incident particle. A test run of a modified beamline has been conducted with the CEBAF Large Acceptance Spectrometer (CLAS) at Thomas Jefferson National Accelerator Facility. This test run demonstrated the feasibility of producing a mixed electron/positron beam of good quality. Extensive simulations performed prior to the run were used to reduce the background rate that limits the production luminosity. A 3.3 GeV primary electron beam was used that resulted in an average secondary lepton beam of 1 GeV. As a result, the elastic scattering data of both lepton types were obtained at scattering angles up to 40 degrees for Q^2 up to 1.5 GeV^2. The cross section ratio displayed an ϵ dependence that was Q^2 dependent at smaller Q^2 limits. The magnitude of the average ratio as a function of ϵ was consistent with the previous measurements, and the elastic (Blunden) model to within the experimental uncertainties. Ultimately, higher luminosity is needed to extend the data range to lower ϵ where the TPE effect is predicted to be largest.

TABLE OF CONTENTS

CHAPTER PAGE

LIST OF TABLES

TABLE PAGE

LIST OF FIGURES

1 Introduction

1.1 Overview

Since late 1940's when the theory of Quantum Electrodynamics (QED) was developed, a virtual photon was assumed to be the mediator of charged particle interactions [1]. The single photon exchange was considered to be the first order approximation to a series of photon propagation terms between the initial and final scattering states. This approximation was assumed to be precise enough, as the rest of the terms were negligible. Therefore, all the particle scattering experiments based their calculations on this assumption and applied a correction to their results to compensate for the minor known radiative effects. It was not until recently when the idea of the inadequacy of this approximation occurred, as inconsistencies between experimental results were observed.

Numerous experiments that have aimed to contribute to understanding the fundamentals of the universe, have done so by conducting particle-scattering studies in many different laboratories. Protons, being one of the most basic-structured particles, have been the focus of a significant number of these studies. Several techniques have been developed to measure the charge and current distributions inside a proton, which lead to the electromagnetic form factors. One of the standard techniques to extract the elastic form factors is called the "Rosenbluth" method [2] and has been utilized for many years. However, the form factor ratio derived by this method seems to be significantly different from the more recent "Polarization Transfer" measurement [3] results at higher values of momentum transfer (Q^2). This measurement revealed a linear drop of the form factor ratio as a function of Q^2, with smaller systematic uncertainties than the "Rosenbluth" method.

This discrepancy led to much speculation and a reexamination of the theoretical assumptions, as the experimental uncertainties have already been ruled out as an explanation. Subsequently, several calculations found the "two-photon exchange" term of the radiative effects to be a likely candidate, as it can have a dramatic effect on the "Rosenbluth" measurements and bring the two methods close to agreement. This chapter offers a more detailed insight into the basics, theoretical calculations and existing evidence for this phenomenon.

1.2 Basic Concepts

This section briefly introduces some basic formalism of this dissertation's discussion, such as elastic scattering kinematics, form factor definition, and measurement techniques.

1.2.1 Elastic Scattering and Form Factors

Elastic electron scattering off light nuclei can provide precise information about charge and current distributions of the nucleons (protons and neutrons). The total scattering wave function can generally be replaced by the incident one, where a single virtual photon [1] is transfered as illustrated in Fig 1, called the Born Approximation. Here k is the initial and k' is the final momentum of the incident lepton, whereas p is the initial and p' is the final momentum of the target nucleon. The four-momentum transfer Q^2, which is a Lorentz invariant quantity that characterizes the dynamics of the scattering, is formulated as:

$$Q^2 = -q^2 = -(k - k')^2 \approx \frac{4EE'}{c^2} \sin^2 \frac{\theta}{2}, \tag{1}$$

where E is the incident and E' is the scattered electron energies, θ is the scattering angle, c=1 in natural units, and the electron mass is neglected.

The electron is a spin 1/2 point particle that is described by the Dirac equation. However, the proton is a hadron with a nontrivial internal structure and its magnetic moment is also involved in the interaction.

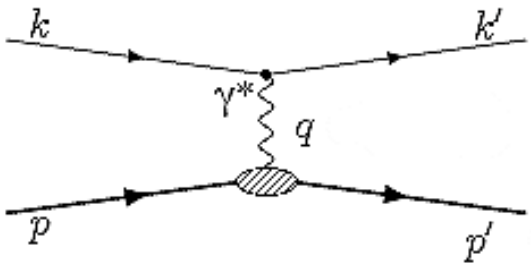

Figure 1: Feynman diagram for first order elastic lepton-nucleon scattering.

[1] A short-lived photon that carries the momentum from the incident to the target particle. Virtual photons may not obey the energy-momentum relation ($E^2 = p^2c^2 + m^2c^4$) for the time permitted by the uncertainty principle.

The lowest order cross section amplitude of the electron-proton elastic scattering can be written as:

$$T_{fi} = -i \int j_\mu \left(\frac{1}{Q^2}\right) J^\mu d^4x, \tag{2}$$

where j_μ and J^μ are the electron and proton transition currents, respectively, that are formulated as follows:

$$j^\mu = -e\bar{u}(k')\gamma^\mu u(k) e^{i(k'-k).x} \tag{3}$$

$$J_\mu = e\bar{u}(p')\Gamma^\mu u(p) e^{i(p'-p).x}, \tag{4}$$

where u and $\bar{u}$ are the spinors for the initial and scattered states of electron and proton respectively, and γ^μ is the Dirac matrix. The Γ^μ 4-vector should be constructed from p, p', q and γ^μ in such a way to make J_μ a Lorentz invariant quantity. It is therefore written as:

$$\Gamma^\mu = \left[F_1(Q^2)\gamma^\mu + \frac{\kappa}{2M} F_2(Q^2) i\sigma^{\mu\nu} q_\nu\right], \tag{5}$$

where F_1 and F_2 are the longitudinal and transverse proton form factors, κ is the anomalous magnetic moment measured to be 1.79, M is the proton mass and $\sigma^{\mu\nu}$ is a 4-tensor.

In non-relativistic approximation, form factors are Fourier transformed charge and current distributions inside nucleons. The form factors modify the scattering cross sections at high enough electron energies where the wavelength of the virtual photon is smaller than the nuclear size. Therefore, at the limit when $q^2 \to 0$ the proton form factors must become:

$$F_1(0) = 1, \qquad F_2(0) = 0. \tag{6}$$

The differential cross section of the electron-proton scattering can then be written in terms of the Mott cross section[2] and the proton form factors as follows:

$$\left(\frac{d\sigma}{d\Omega}\right)_{lab} = \left(\frac{d\sigma}{d\Omega}\right)_{Mott} \left[\left(F_1^2 + \kappa^2 Q^2 4M^2 F_2^2\right) - \frac{q^2}{2M^2}(F_1 + \kappa F_2)^2 \tan^2\frac{\theta}{2}\right]. \tag{7}$$

[2]The Mott cross section is the scattering cross section of an electron off a point-like (structureless) particle: $(d\sigma/d\Omega)_{Mott} = \alpha^2 E' \cos^2(\theta/2)/4E^3 \sin^4(\theta/2)$.

The longitudinal and transverse form factors can be substituted by the Sachs electric and magnetic form factors to avoid the inconvenient $F_1.F_2$ term in the scattering cross section defined in Eq. 7.

$$\begin{aligned} G_E &= F_1 - \frac{\kappa Q^2}{4M^2} F_2 \\ G_M &= F_1 + \kappa F_2. \end{aligned} \tag{8}$$

Using this convention, the scattering cross section can be re-written as:

$$\begin{aligned} \left(\frac{d\sigma}{d\Omega}\right)_{lab} &= \left(\frac{d\sigma}{d\Omega}\right)_{Mott} \left[\frac{G_E^2(Q^2) + \tau G_M^2(Q^2)}{1+\tau} + 2\tau G_M^2(Q^2) \tan^2\frac{\theta}{2}\right] \\ &= \left(\frac{d\sigma}{d\Omega}\right)_{Mott} \cdot \frac{1}{\epsilon(1+\tau)} \left[\epsilon G_E^2(Q^2) + \tau G_M^2(Q^2)\right], \end{aligned} \tag{9}$$

where $\tau = Q^2/4M^2$ is a kinematic factor, and $\epsilon = 1/(1 + 2(1+\tau)\tan^2(\theta/2))$ is the virtual photon polarization. This cross section is also known as the Born cross section for the one virtual photon exchange approximation.

At the limit where $Q^2 \to 0$, the electric and magnetic form factors of proton are:

$$G_E(0) = 1, \qquad G_M(0) = \mu_p, \tag{10}$$

where $\mu_p = 1 + \kappa$ is the proton magnetic moment (in Bohr magnetons) [4].

1.2.2 Electromagnetic Form Factor Measurements

The Sachs electric and magnetic form factors discussed in the previous section have been measured using several methods in different experiments. The first measurements were done using the "Rosenbluth" or "L-T separation" method, which yields the electric and magnetic form factors by determining the Born cross section for different ϵ values at a given Q^2. A more recent way to access these important quantities is by "polarization transfer" studies and calculating the form factor ratio by measuring the recoiling proton polarization, using a polarized electron beam. This section discusses these techniques in more detail.

1.2.2.1 Rosenbluth Separation Method

As seen in the previous section, Eq. 9 illustrates how the elastic scattering cross section can be parameterized in terms of electric and magnetic form factors separately. A Rosenbluth separation is performed by varying the incident electron energy and the angle of the scattered electron to keep Q^2 constant while changing ϵ. The fact that the reduced cross section can be written as:

$$\sigma_R = \left(\frac{d\sigma}{d\Omega}\right)_{Born} \cdot \left(\frac{\epsilon(1+\tau)}{\sigma_{Mott}}\right) = \left(\epsilon G_E^2(Q^2) + \tau G_M^2(Q^2)\right), \tag{11}$$

and is a linear function of ϵ, enables the extraction of the electromagnetic form factors from the slope and intercept of the fitted data points as clearly shown in Fig. 2.

It has been observed that at large Q^2 values, G_M is the dominant term in the cross section for all ϵ values, increasing the uncertainty of G_E measurement in this range [5]. Fig. 3 displays these uncertainties for both form factors. The typical uncertainty for G_M is around 1% except for at very low Q^2, whereas uncertainty for G_E reaches about $5-10\%$ at Q^2 of about $2-4$ GeV^2, and increase rapidly as Q^2 increases [6].

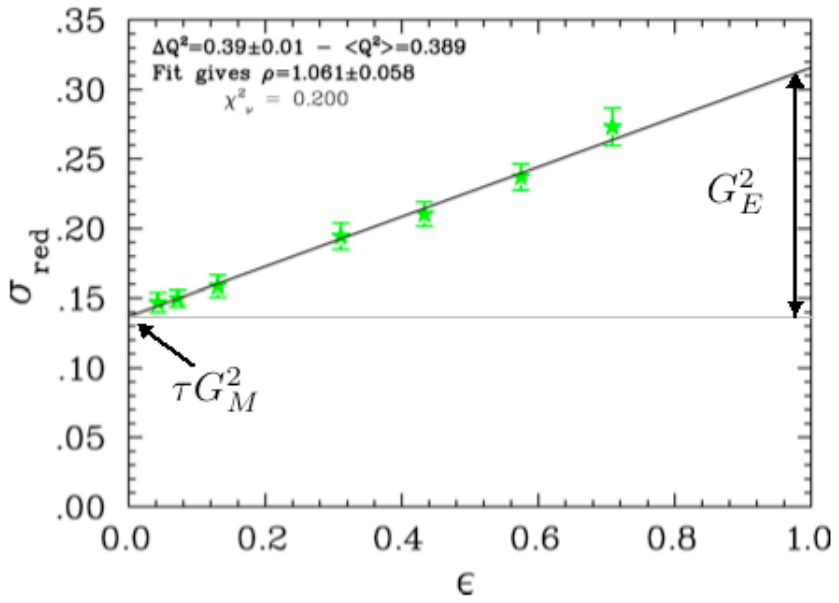

Figure 2: Extraction of electric and magnetic form factors using the Rosenbluth method. A linear fit to the reduced cross section of the proton is shown as a function of ϵ.

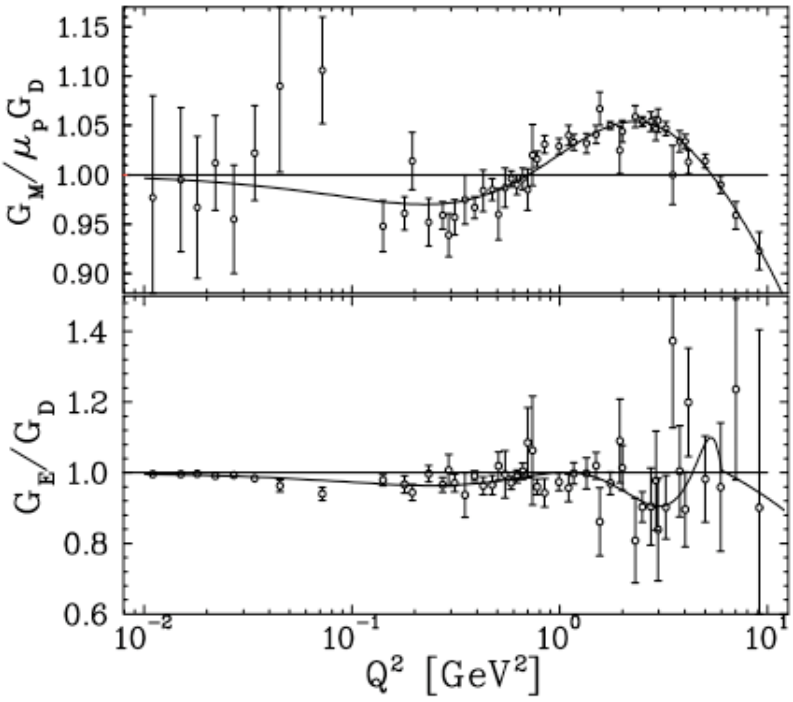

Figure 3: G_M and G_E from Rosenbluth separations. $G_D = [1 + Q^2/M_D^2]^{-2}$ is the dipole form factor, where $M_D^2 = 0.71$ GeV^2. The curves are from a global fit of all data [6].

1.2.2.2 Polarization Transfer Method

The ratio of the proton electromagnetic form factors can be obtained by performing polarization transfer (PT) measurements in the reaction $\vec{e}p \to e\vec{p}$. The recoil proton has two polarization components, one longitudinal (P_l) and one transverse (P_t) to its momentum in the scattering plane. In the Born approximation these quantities are calculated as follows:

$$I_0 P_t = -2\sqrt{\tau(1+\tau)} G_E G_M \tan\frac{\theta}{2} \quad (12)$$

$$I_0 P_l = \frac{1}{M_p}(E + E')\sqrt{\tau(1+\tau)} G_M^2 \tan^2\frac{\theta}{2}, \quad (13)$$

where I_0 is proportional to the unpolarized cross section:

$$I_0 \propto G_E^2 + \frac{\tau}{\epsilon} G_M^2. \quad (14)$$

Taking the ratio of equations 12 and 13 yields the ratio of electric to magnetic form factors:

$$\frac{G_E}{G_M} = -\frac{P_t}{P_l}\frac{(E+E')}{2M_p}\tan\frac{\theta}{2}. \tag{15}$$

This ratio is obtained by making a single measurement to find the recoil polarizations P_t and P_l, using a custom-built polarimeter. However, finding the form factors individually requires obtaining I_0 using cross section measurements. Fig. 4 represents a plot showing the data measured in Hall A Jefferson lab overlaid on other experimental and theoretical form factor ratios [7].

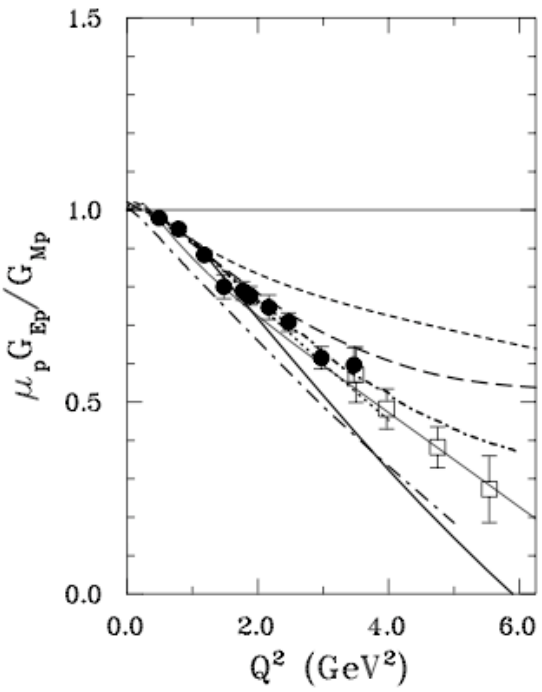

Figure 4: Comparison of the electromagnetic form factor ratio. Data were obtained by Punjabi (solid circles) [7], and Gayou (hollow squares) [8] both performed at Jefferson lab Hall A, with some theoretical calculations. Each of the curves correspond to the following references: dotted is by Chung and Coester [9], thick solid by Frank, Jennings and Miller [10], short dot-dashed by Cardarelli and Simula [11], dot-dashed and dashed by Pace, Salme, Cardarelli and Simula [12], short-dashed by Boffi [13], and thin solid is calculated by Gross and Agbakpe [14].

1.3 Beyond the Born Approximation

1.3.1 Motivation

Both Rosenbluth separation and the polarization transfer formalism have been based on the Born approximation. In the limits of this approximation, only the single photon exchange term is considered in calculating the scattering cross section, and the rest of the terms are taken into account by applying "standard" radiative corrections. However, comparison of two different sets of results for these techniques reveal an unexpected discrepancy that increases considerably at larger Q^2 values. The polarization transfer ratio seems to decrease more rapidly with Q^2 than the Rosenbluth. Fig. 5 illustrates this inconsistency, which is about a factor of three at $Q^2 \approx 5.6$ GeV^2.

Due to the Q^2-dependent nature of the discrepancy in the form factor ratio, the problem has generally been assumed to be with the cross section measurements. Moreover, a small ϵ dependent correction to the cross section can account for this difference, as G_E is suppressed compared to G_M in the large Q^2 range. Recent theoretical calculations [15, 16, 17] suggest that the two photon exchange term, which is generally ignored in radiative corrections, can in fact introduce an error in calculating the form factors from the cross sections.

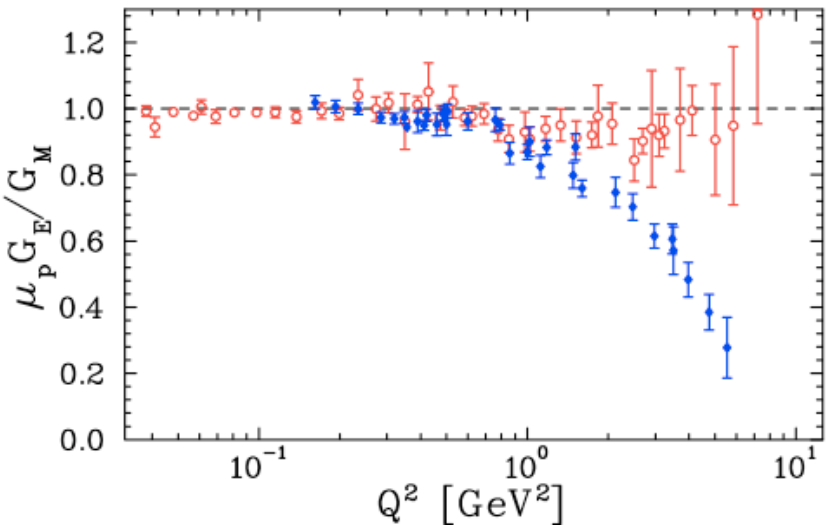

Figure 5: Comparison of Rosenbluth and polarization transfer results. The former G_E/G_M ratio is shown in hollow circles and latter in solid diamonds for $Q^2 = 0 - 10$ GeV^2 [18].

The extended studies of the two photon exchange effect show that this correction can, in fact, be large enough to explain the disagreement of the two discussed methods. These studies go beyond the limited standard radiative correction calculations and examine the effects of this poorly defined term.

1.3.2 Radiative Effects

Radiative processes (Fig. 6), except for the TPE effects (Fig. 6(e)(f)), are usually taken into account by performing radiative correction procedures during the data analysis. The terms that only involve the electron and photon can be calculated exactly in QED. Additionally, the proton vertex (Fig. 6(g)) term is a small ϵ independent value, whereas proton bremsstrahlung (Fig. 6(h)) is well understood due to the low-energy theorem [19]. Therefore, the most significant uncertainty is associated with the two photon exchange terms.

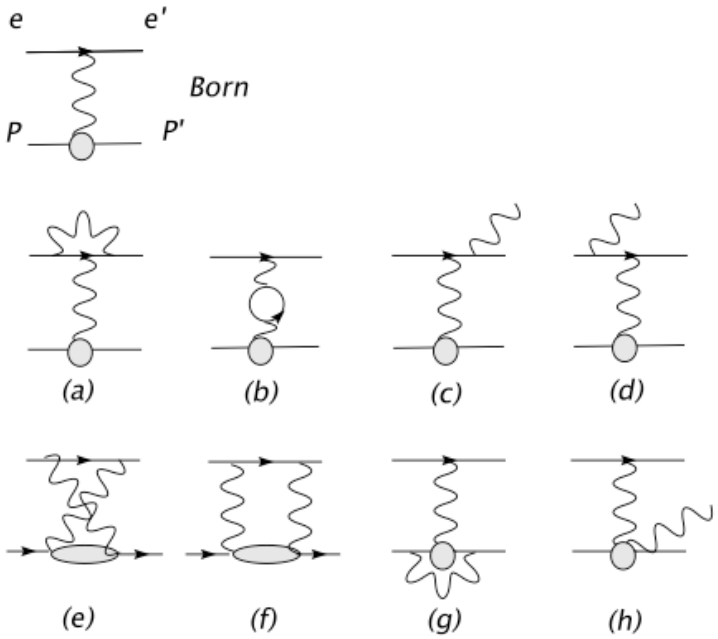

Figure 6: Feynman diagrams illustrating the radiative corrections, extending the Born approximation for the elastic electron-proton scattering. These processes are: (a,g)vertex corrections for the electron and proton, (b)vacuum polarization or loop diagram, (c,d,h)bremstrahlung radiation for electron and proton, and (e,f) two photon exchange.

1.3.3 TPE Corrections

As mentioned before, at high values of Q^2 the contribution of G_E to the cross section drops considerably. As shown in Fig. 7, in order for the Rosenbluth and polarization transfer data to come to an agreement the slope of the reduced cross section (G_E) needs to be modified. Therefore, only a $5-8\%$ correction will be sufficient for this purpose. As can also be seen, this correction should be linearly ϵ dependent and change weakly with Q^2.

Different theoretical models have incorporated the TPE effect in calculating the cross section and have observed substantial changes in the form factor ratio, despite the small size of the correction. These models will be discussed in the following section.

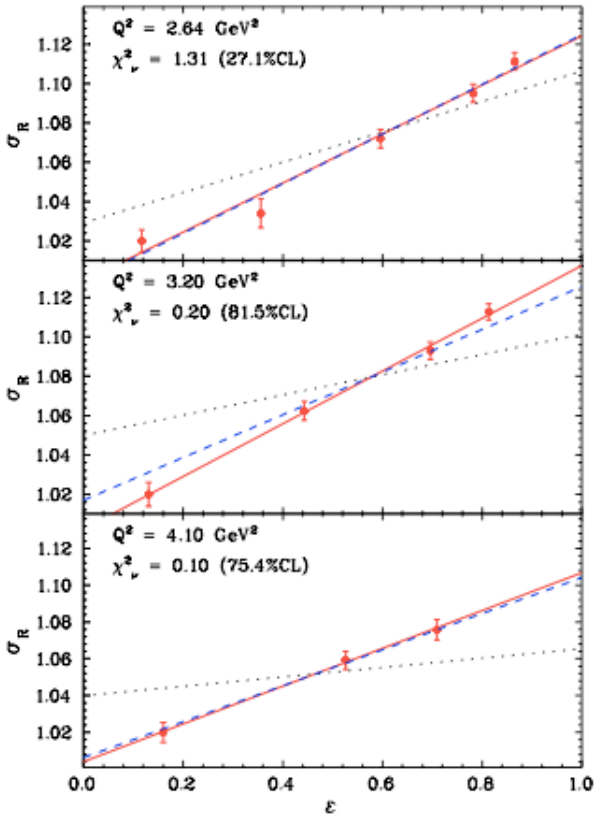

Figure 7: Reduced cross section for Rosenbluth and polarization transfer data. The solid line is a fit to the Rosenbluth data, compared to the older Rosenbluth measurements (dashed line is a fit to the data), scaled to $\sigma_R = 1$ at $\epsilon = 0$. The polarization transfer measurements (dotted line is a fit to the data) is also shown [20].

1.4 Theoretical Calculations

1.4.1 HIS Model

The Hadronic Intermediate State model developed by Blunden, Melnitchouk and Tjon [21], focuses on incorporating the radiative effects into the amplitudes (loop integrals). These modifications hence carry over to the cross section calculations and introduce a correction factor to the Rosenbluth separation results, as the PT technique measures the cross section ratio and is not as sensitive to the ϵ dependence of the correction. Of all the "factorizable" terms added to the modified amplitude, only the infrared (IR) divergent two photon exchange term contributes to the ϵ dependence of the virtual photon correction. In fact the two photon exchange contribution to the modified amplitude ($\mathcal{M}^{\gamma\gamma}$) includes all possible intermediate hadronic states.

This model uses the assumption that the proton propagated as a Dirac particle and phenomenological form factors can be used at the γp vertex to find the two photon exchange IR divergent terms for box and cross box TPE diagrams (Figs. 6(e)(f) respectively):

$$\mathcal{M}_a^{\gamma\gamma(IR)} = -\frac{\alpha}{\pi}\ln\left(\frac{2k\cdot p}{mM}\right)\ln\left(\frac{Q^2}{\lambda^2}\right)\mathcal{M}_0, \tag{16}$$

$$\mathcal{M}_b^{\gamma\gamma(IR)} = \frac{\alpha}{\pi}\ln\left(\frac{2k'\cdot p}{mM}\right)\ln\left(\frac{Q^2}{\lambda^2}\right)\mathcal{M}_0, \tag{17}$$

where $\mathcal{M}_0$ is the Born amplitude, λ is the infinitesimal photon mass, and $\alpha = e^2/4\pi$.

Therefore the full IR divergent two photon exchange correction then becomes:

$$\delta_{IR} = -2\frac{\alpha}{\pi}\ln\left(\frac{E}{E'}\right)\ln\left(\frac{Q^2}{\lambda^2}\right), \tag{18}$$

where $E = k\cdot p/M$ and $E' = k'\cdot p/M$ [21].

The modified cross section for the Rosenbluth separation is calculated using this model:

$$d\sigma = (aA)\tau G_M^2(Q^2)\left(1 + (B\tilde{R}^2 + b)\epsilon\right), \tag{19}$$

where $B = 1/\mu_p^2\tau$, and $\tilde{R}$ is the corrected ratio, a and b are the parameters of a linear fit of

the correction as a function of ϵ, and A is a proportionality constant. As Fig. 8 shows, the correction found using this model shifts the Rosenbluth form factor ratio toward the PT measurement ratio and decreases the discrepancy considerably. This correction was found to be even more effective using more realistic form factors [16].

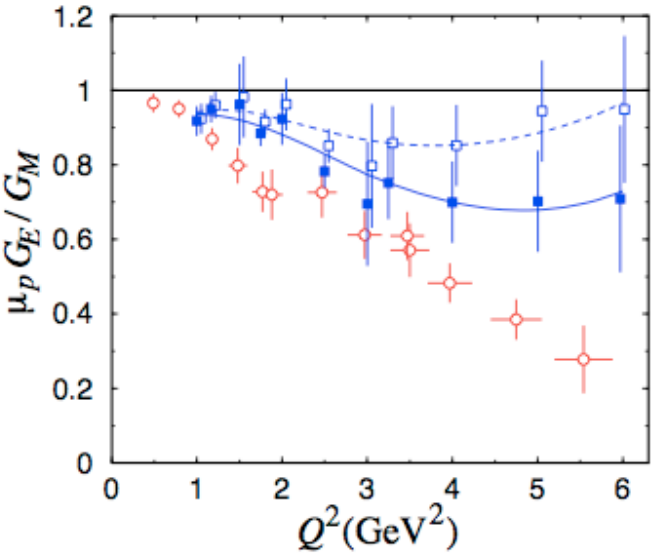

Figure 8: Form factor ratio for Rosenbluth and PT measurements. The former is shown in hollow squares and letter in hollow circles. The shift in corrected Rosenbluth ratio (solid squares) is shown as well as a global fit. The error bars have remained unchanged after the correction [21].

1.4.2 Axial-VMD Model

The axial Vector Meson Dominance model developed by Drell and Sullivan, and revised by Afanasev, relates the two photon exchange effect to the photon-nucleon coupling through light axial vector mesons such as $a_1(1260)$ and $f_1(1285)$. This model adds this coupling to the direct photon nucleon coupling and extracts the coupling parameters by fitting the difference between the Rosenbluth and PT measurements of the form factor ratio. The VMD cross section calculations introduce a two photon exchange correction term that reduces the discrepancy between the two form factor measurement methods. The value of this correction is inversely proportional to ϵ [19].

1.4.3 GPD Model

In this model, Afanasev, Chen, Brodsky and Carlson relate the scattering processes off protons to the Generalized Parton Distribution (GPD) [22]. The calculations assume that the electron scatters off a quark (parton) inside the nucleon. The scattering amplitude for a partonic subprocess contains complex form factors that include a contribution from the two photon part of the radiative effects. The real and imaginary parts of hard ($Q^2 >> M^2$) and soft scattering form factors associated with the two photon exchange amplitude are separately calculated. The real part gives rise to the corrected cross section with the two photon correction term defined as $d\sigma = d\sigma_{1\gamma}(1 + \delta_{2\gamma})$, and the 2γ correction term:

$$\delta_{2\gamma} = \frac{e^2}{4\pi^2}\left\{2\ln\left(\frac{\lambda^2}{Q^2}\right)\ln\left|\frac{\hat{s}}{\hat{u}}\right| + \frac{(\hat{s}-\hat{u})Q^2}{2(\hat{s}^2+\hat{u}^2)}\left[\ln^2\left|\frac{\hat{s}}{Q^2}\right| + \ln^2\left|\frac{\hat{u}}{Q^2}\right| + \pi^2\right] + \frac{Q^2}{\hat{s}^2+\hat{u}^2}\left[\frac{\hat{u}}{Q^2}\ln\left|\frac{\hat{s}}{Q^2}\right| - \frac{\hat{s}}{Q^2}\ln\left|\frac{\hat{u}}{Q^2}\right|\right]\right\}, \tag{20}$$

where $\hat{s} = (k + p_q)^2$ and $\hat{u} = (k - p'_q)^2$ are the invariant Mandelstam variables for the handbag approximation shown in Fig. 9. $d\sigma_{1\gamma}$ is the Born cross section.

The next step is investigating these subprocesses by placing the quarks inside the nucleon and involving GPDs in form factor and cross section calculations. The GPDs have been estimated using two different models: a Gaussian model and a modified Regge model.

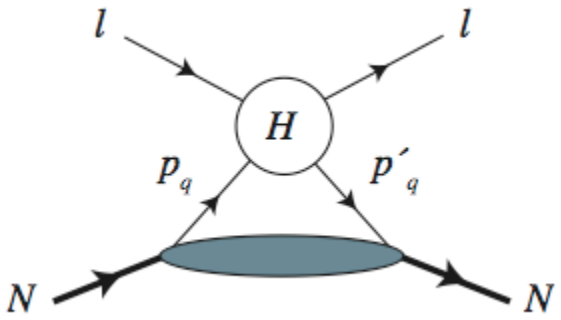

Figure 9: The handbag approximation for electron-nucleon elastic scattering. In this subprocess (with amplitude H) the hard photons scatter off the quarks, which will then be embedded into the nucleon's GPD.

As can be seen in Fig. 10, implementing the hard two photon exchange correction resulted from this study brings the Rosenbluth and PT measurement to substantially better reconciliation. This correction changes the slope of the Rosenbluth cross section effectively leaving the PT measurements with only a minor modification [23].

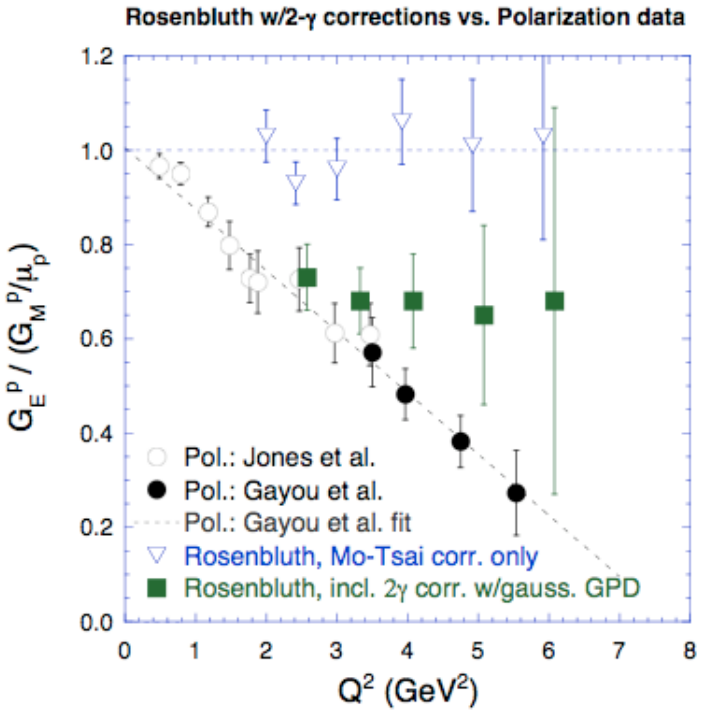

Figure 10: Corrected and uncorrected Rosenbluth data overlaid on PT measurements. The TPE corrected data (solid squares) and the uncorrected ones (hollow triangles) are overlaid on the PT measurement results (circles). The TPE correction apparently has a positive effect in reconciling the two sets of measurement [23].

1.4.4 G-V Estimate

Guichon and Vanderhaeghen [17] have estimated the size of the two photon exchange correction by adding the higher order radiative terms in the cross section amplitude and expanding those terms in power of e^2; that is the square of proton charge: $e \simeq \sqrt{4\pi/137}$. Keeping the terms to the order of e^2, only the two photon exchange terms will remain to be considered.

This model calculates the cross section and the polarization ratio as:

$$\frac{d\sigma}{C_B(\epsilon, Q^2)} \simeq \frac{|\tilde{G}_M|^2}{\tau}\left\{\tau + \epsilon\frac{|\tilde{G}_E|^2}{|\tilde{G}_M|^2} + 2\epsilon\left(\tau + \frac{|\tilde{G}_E|}{|\tilde{G}_M|}\right)\mathcal{R}\left(\frac{\nu\tilde{F}_3}{M^2|\tilde{G}_M|}\right)\right\}, \tag{21}$$

$$\frac{P_t}{P_l} \simeq -\sqrt{\frac{e\epsilon}{\tau(1+\epsilon)}}\left\{\frac{|\tilde{G}_E|}{|\tilde{G}_M|} + \left(1 - \frac{2\epsilon}{1+\epsilon}\frac{|\tilde{G}_E|}{|\tilde{G}_M|}\right)\mathcal{R}\left(\frac{\nu\tilde{F}_3}{M^2|\tilde{G}_M|}\right)\right\}. \tag{22}$$

It then defines the dimensionless quantity:

$$Y_{2\gamma}(\nu, Q^2) = \mathcal{R}\left(\frac{\nu\tilde{F}_3}{M^2|\tilde{G}_M|}\right), \tag{23}$$

where $\nu = K \cdot P$ ($K = (k + k')/2$ and $P = p + p'/2$), $\mathcal{R}$ denotes the real part, and $\tilde{F}_3$ and $\tilde{G}_M$ are the complex form factors. $\tilde{G}_E$ is defined as $\tilde{G}_E = \tilde{G}_M - (1 + \tau)\tilde{F}_2$.

To solve equations 21 and 22 for $Y_{2\gamma}$, experimental data from Andivahis [24] are examined and several approximations are made to the equations that are believed to explain the data. This calculation assumes that $\tau\tilde{F}_3$, $|\tilde{G}_M|$ and $|\tilde{G}_E|$ are independent of ϵ. Applying these approximations to the above equations gives rise to cross sections and polarization ratios with two photon effects included. The new system is then solved numerically by fitting the data with a polynomial function. Fig. 11 shows the result of this calculation for different values of Q^2. These ratios are independent of ϵ and very small (on the order of a few percent), which is consistent with the expectations for the size of the effective two photon correction.

The cross section ratios for fits of the original experimental Rosenbluth data and polarization transfer measurements are compared in Fig. 12 with the corrected experimental data using this technique. It is clearly seen that the corrections bring the two measurements closer together. However, the remaining difference between the two curves may be due to ignoring the contribution of hadronic intermediate states in this calculation [17].

This calculation was continued by Arrington [25], using the same generalized form factors and adding constraints from the existing positron dataset to calculate a more detailed 2γ correction.

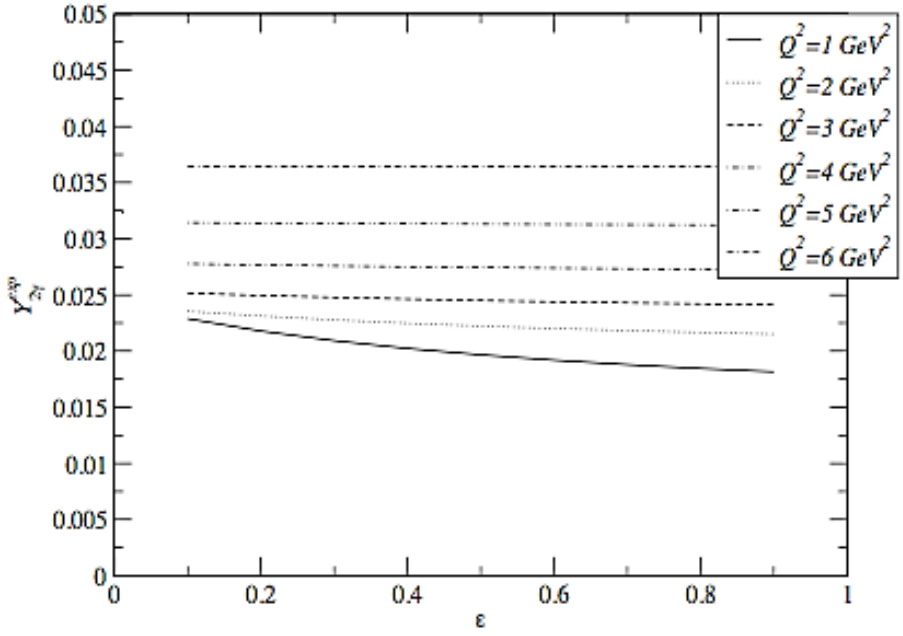

Figure 11: $Y_{2\gamma}$ distribution as a function of ϵ for different Q^2, [17].

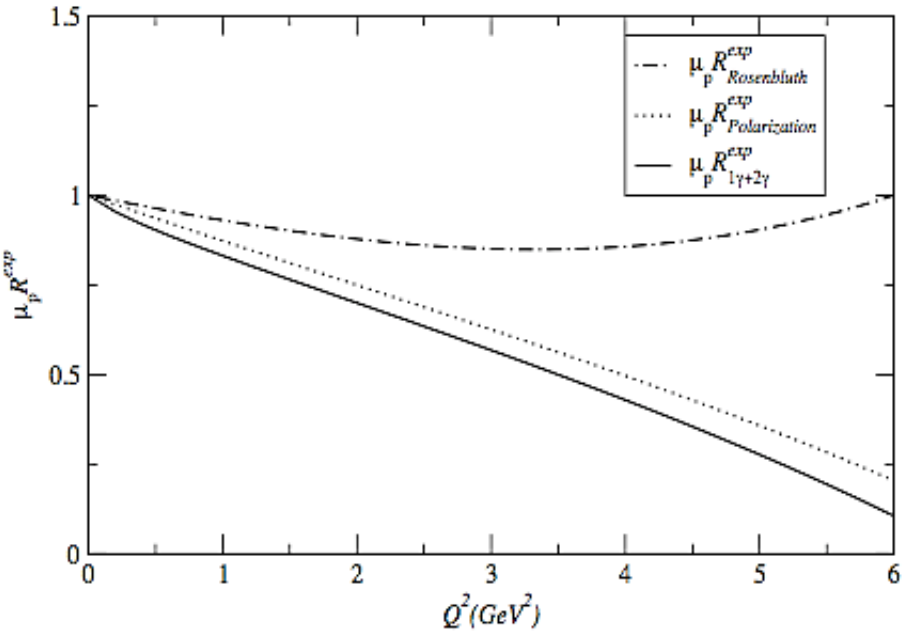

Figure 12: TPE corrected form factor ratio using the G-V estimate, compared to the original Rosenbluth and PT measurement data [17].

1.5 TPE Measurement

A direct model independent measurement of the two photon exchange (TPE) correction can be achieved experimentally by finding the ratio of the positron-proton to electron-proton elastic cross sections. It has been observed that most of the radiative effects are identical for electrons and positrons, except for the interference between electron/positron and proton bremsstrahlung, and the two photon exchange effect. Therefore, the total amplitude for electron-proton elastic scattering that contributes to the charge asymmetry only includes the amplitudes below:

$$A_{total} = e_e e_p A_{Born} + e_e^2 e_p A_{e.brem.} + e_e e_p^2 A_{p.brem.} + e_e^2 e_p^2 A_{2\gamma}, \quad (24)$$

$$|A_{total}|^2 = e_e^2 e_p^2 \left[|A_{Born}|^2 + 2 e_e e_p A_{Born} \mathcal{R}(A_{2\gamma}^*) + 2 e_e e_p \mathcal{R}(A_{e.brem.} A_{p.brem.}^*) \right], \quad (25)$$

where As stand for different radiative amplitudes, and $\mathcal{R}$ indicates their real parts. The square of the total amplitude (approximated to the e^2 order), which will be inserted in the cross section calculation, only contains the real parts of the 2γ and the interference terms, whose infrared divergent parts cancel each other out. Taking the ratio of positron- to electron-proton cross sections is a sensitive way to isolate the TPE term as the interference bremsstrahlung term is calculable. The charge asymmetry can be found as:

$$\sigma(e^{\pm}) = \sigma_{Born}(1 \mp \delta_{2\gamma}), \quad (26)$$

$$R = \frac{\sigma(e^+)}{\sigma(e^-)} \approx 1 - 2\delta_{2\gamma}, \quad (27)$$

where $\delta_{2\gamma}$ is the two photon exchange correction factor.

Fig. 13 shows the expected asymmetry ratio plotted as a function of ϵ for several different Q^2 bins. This is the result of an extended analysis using G-V estimates and existing positron data in [25]. The TPE effect is expected to increase for lower ϵ and higher Q^2 values [19].

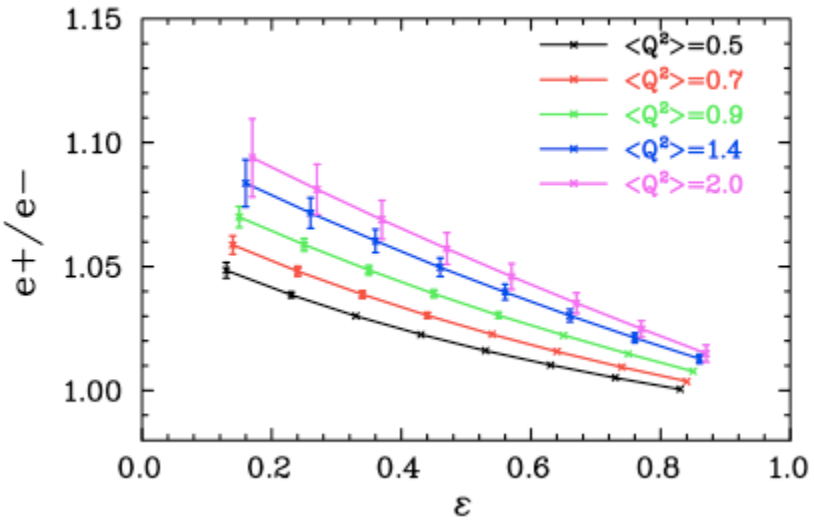

Figure 13: Cross section ratio as a function of ϵ for the full Hall B measurement, and for several Q^2 bins [19]. The error bars are the expected statistical uncertainties.

1.6 Existing Data

The charge asymmetry ratio has been previously examined by Mar *et* al. [26] at Stanford Linear Accelerator Center (SLAC) in 1960's. This measurement covered a Q^2 range that was extended to a bit higher than previously measured. Fig. 14 summarizes the result of this experiment and compares it to the older measurements.

Fig. 15 illustrates the cross section ratio for the world data as a function of ϵ. These measurements, however, are mostly at low Q^2 with a weighted average of about 0.4 GeV^2. In this Q^2 range, the increase of the correction at lower ϵ corresponds to about 2.8% effect on the slope of the Rosenbluth measurements. That is almost half the correction needed to explain the discrepancy. Higher Q^2 electron-positron comparison was recently proposed to be done at VEPP-3 in Novosibirsk, Russia. The expected data points are overlaid on the world data with a linear fit for $Q^2 \approx 1.6$ GeV^2. This measurement is expected to have more sensitivity to measure the TPE contribution [20, 27].

Also shown in Fig. 15 is the expected data from Hall-B Jefferson lab that was previously shown in Fig. 13.

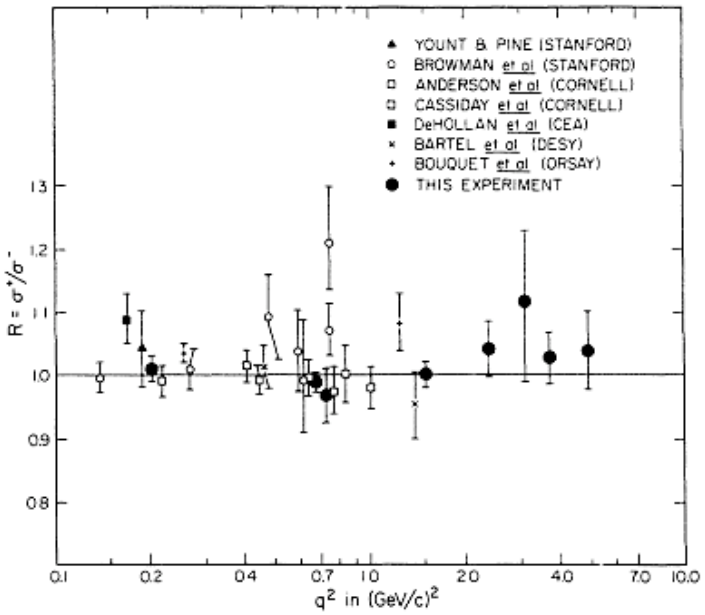

Figure 14: Charge asymmetry ratio for SLAC data and previous measurements. The SLAC data collected by Mar and collaborators (solid circles) is overlaid on the existing data (hollow symbols) as a function of Q^2 [26].

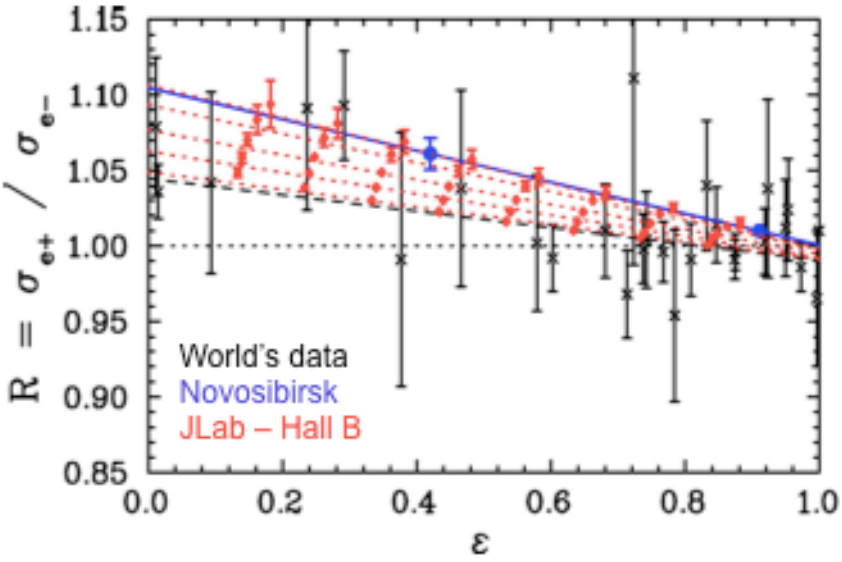

Figure 15: World data for the cross section ratio, shown by stars, overlaid by Novosibirsk (solid circles with linear fit) as well as the expected Jlab measurements for several Q^2 (dotted lines and red points) [20, 27].

1.7 Experimental Technique

In order to directly measure the real part of the two photon exchange contribution to the elastic scattering cross section at Jefferson Lab, a combined positron/electron beam was designed in Hall-B. The beam types previously used in this lab have been either electron or photon beams. The production of positrons required a somewhat more complicated beamline design.

The primary electrons were converted to bremsstrahlung photons in the usual way using an ultra thin radiator foil upon their entrance to the experimental hall. After being separated from the remaining electrons, the new photon beam was propagated into a converter material that caused the photons to pair produce into electron/positron pairs. These particles were then sent into a chicane magnet that horizontally separates and recombines them in order to stop the photons that did not interact with the converter. The secondary beam was a mixture of electrons and positrons with the same momentum and phase. The setup of all the mentioned components and the detector system will be discussed in detail in the following chapter.

The systematic uncertainties of this measurement are mainly due to the asymmetries of electron- and positron-proton scattering and detection. Having identical beam particles with the same flux is a big step toward reducing these uncertainties. However, different effects from beam attenuation and transport for the two leptons still exist. The difference in detector acceptance for electrons and positrons, or protons from the two reactions is the main contribution to the systematic errors. Despite the abundant sources of systematic uncertainty, they can mostly be avoided or accounted for. The important acceptance effects were greatly minimized by taking data with both positive and negative polarities of the detector magnetic field. Also the beam transport was monitored throughout the experiment for any asymmetries, the mixed beam was simultaneously produced and sent to the same target, and the trigger system was modified as explained in the next chapter. The details of the uncertainty analysis for the TPE test run can be found in Chapter 5. The expected uncertainties for the full experiment have been described in detail in [19].

This dissertation describes the TPE test run conducted in Hall B Jefferson Lab. The following chapters cover a full introduction to the experimental setup, background simulations prior to the test run to increase the production luminosity by identifying and eliminating the sources of secondary-beam related background, and the calibration and complete analysis of the TPE data.

2 Experimental Apparatus

This chapter summarizes the experimental setup that has been utilized for performing the two-photon exchange experiment. The CEBAF accelerator [28] is the heart of the Department of Energy's Thomas Jefferson National Accelerator Facility, which along with the CLAS spectrometer in Hall-B [29], are the main pieces of equipment for this study. The beamline for the two-photon exchange test run has been modified and will be discussed in the last section of this chapter.

2.1 The CEBAF Accelerator

The Continuous Electron Beam Accelerator Facility (CEBAF) is a superconducting electron beam accelerator that has been Jefferson lab's source of continuous-wave (CW) beam for many years. It consists of two linear accelerators (LINACs) and two circulating arcs to form a 1.4 km underground race track sweeping around the Jefferson Lab site. The superconducting radio-frequency (SRF) nature of the accelerator allows the production of a continuous beam that can then be simultaneously sent to three separate end stations, known as experimental halls A, B and C. The separate CW beams can be up to 180 μA, with energy ranges from 0.6 to 5.7 GeV. An energy upgrade to 12 GeV is currently being planned [30]. The current, energy and orientation of the beam polarization can be different for the three halls, with current differences between the halls approaching six orders of magnitude. See Fig. 16 for a schematic overview of the accelerator.

CEBAF is a five-pass re-circulating accelerator with a very high duty factor that results in a low background rate in coincidence experiments with small cross sections, while delivering high-quality beam for use with high-resolution spectrometers. The continuous nature of the beam is also suitable to achieve a higher luminosity that improves the statistics of the collected experimental data.

The CEBAF gun-based injector is where the electron beam actually originates. It consists of a photo-emission electron gun, an RF accelerating cavity and a chopper. The gun is driven by laser light and uses photons to strip electrons from a gallium arsenide

photocathode. It includes three diode lasers, one for each experimental hall, that allows for independent control of each hall's beam current and polarization. Each laser is pulsed at 499 MHz frequency, with a 120° relative phase shift. Therefore, every hall receives a packet of electrons every 2 ns. After leaving the photocathode, the electrons are packaged by an optical chopper before being injected into the main accelerator track [28].

Each CEBAF LINAC consists of twenty cryomodules, each containing eight superconducting radio-frequency cavities (Fig. 17(a)) made of niobium, which is a superconductor at very low temperatures. Therefore these cavities are cooled to −271°C (2 K) within the LINACs. A 5 kW permanent-magnet-focused klystron generates the RF power for each cavity. It sets up a 1497 MHz RF standing wave in the cavity, in phase with the electron beam bunches. This provides a positive electric force on the electron packet as it moves through that cavity. Fig. 17(b) shows this process more clearly.

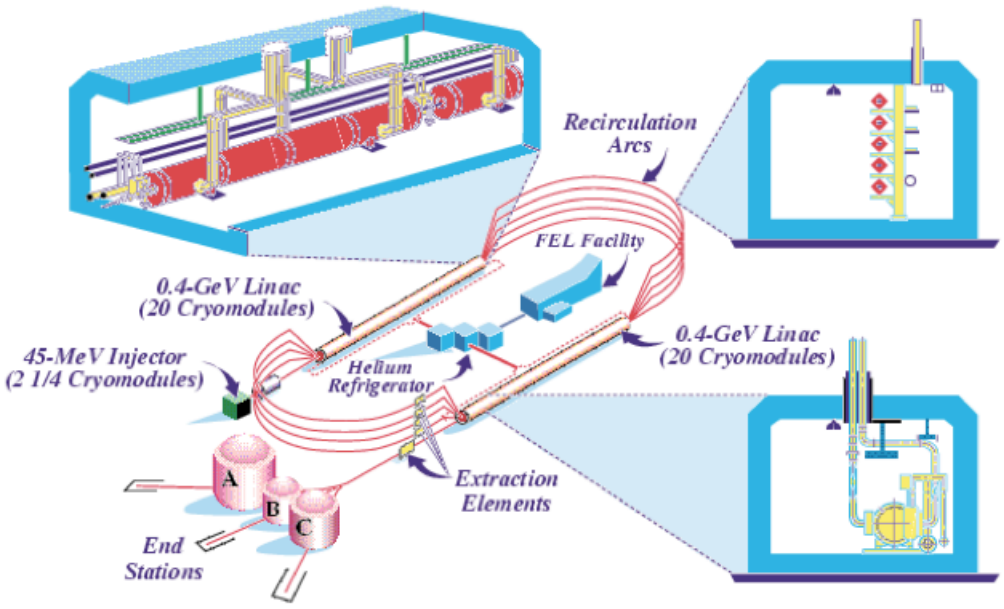

Figure 16: An overview of the Jefferson Lab site and the CEBAF accelerator, which sends the accelerated electrons to three experimental halls A, B and C. Cross sections of LINAC cryomodules and recirculating arcs are zoomed in for more clarity [29].

The two parallel LINACs are joined by 180° circulating arcs with an 80 m radius. This combination recirculates the beam up to 5 times and increases the energy about 1.2 GeV in each pass. Quadrupole and dipole magnets are used to steer and focus the beam through the arcs. The resulting beam is very precisely positioned and tightly focused.

After the second LINAC, the 499 MHz RF separator cavities extract the beam for the experimental halls. They choose every third electron bunch to send out to each hall. Furthermore, the halls can choose on which pass along the accelerator to extract the beam according to the desired incident electron energy.

(a)

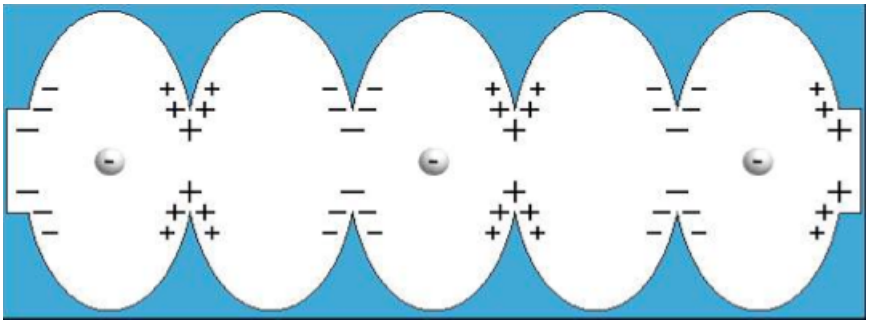

(b)

Figure 17: CEBAF accelerator cavities, (a) These cavities are made of niobium, which is superconducting when cooled down to -271°C. There are 338 of such cavities used at CEBAF. (b) The electrons accelerate through the cavities' oscillating standing microwaves that induce charges on the inner surface of the cavities such that the electrons always have a net positive charge in front of them. Therefore, they feel a continuous positive force and accelerate.

2.2 Hall B and the CLAS Detector

Experimental Hall B, which is the smallest of the three underground experimental halls, has a unique set up. Unlike the other two halls, the detector system in Hall B is a sphere-shaped multi-layered apparatus, positioned in the center of the hall. This detector has an almost 360° polar and azimuthal angle coverage. Another distinctive feature of Jefferson lab's Hall B is the photon tagger system that can produce a real photon beam and use it in a variety of photo-production experiments. Fig. 18 illustrates Hall B, whose components will be discussed in detail in this chapter.

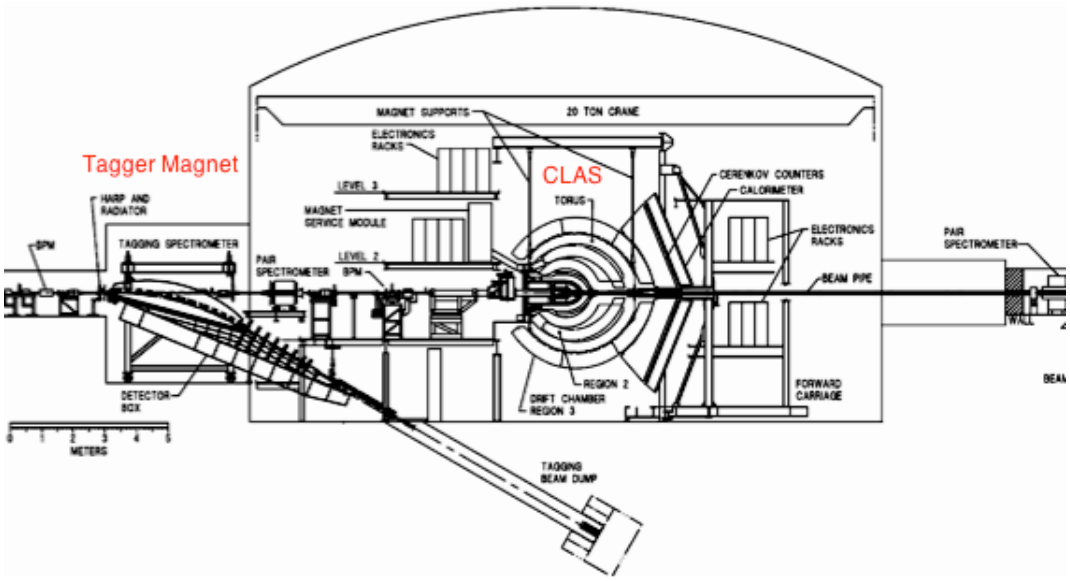

Figure 18: Side view of Hall B Jefferson lab. It is an underground dome where a branch of the beamline enters (left) and faces the detector system (CLAS) at the center of the hall.

2.2.1 Beamline and Tagging System

2.2.1.1 The Photon Tagger

As it enters Hall B, the electron beam encounters the photon tagging system [31]. In electron runs the tagger is turned off and is not in use. Bremsstrahlung photons are produced in a thin radiator foil before the electrons are bent and swept underground using the tagger magnet. These real photons then continue their way towards the target. This system can

tag photon energies of 20% to 95% of the initial electron energy with an energy resolution of 1×10^{-3} of the initial electron energy (E_0). The components of the tagger are explained below in order of their appearance to the beam traveling downstream. Fig. 19 presents a diagram of the Hall B tagger system.

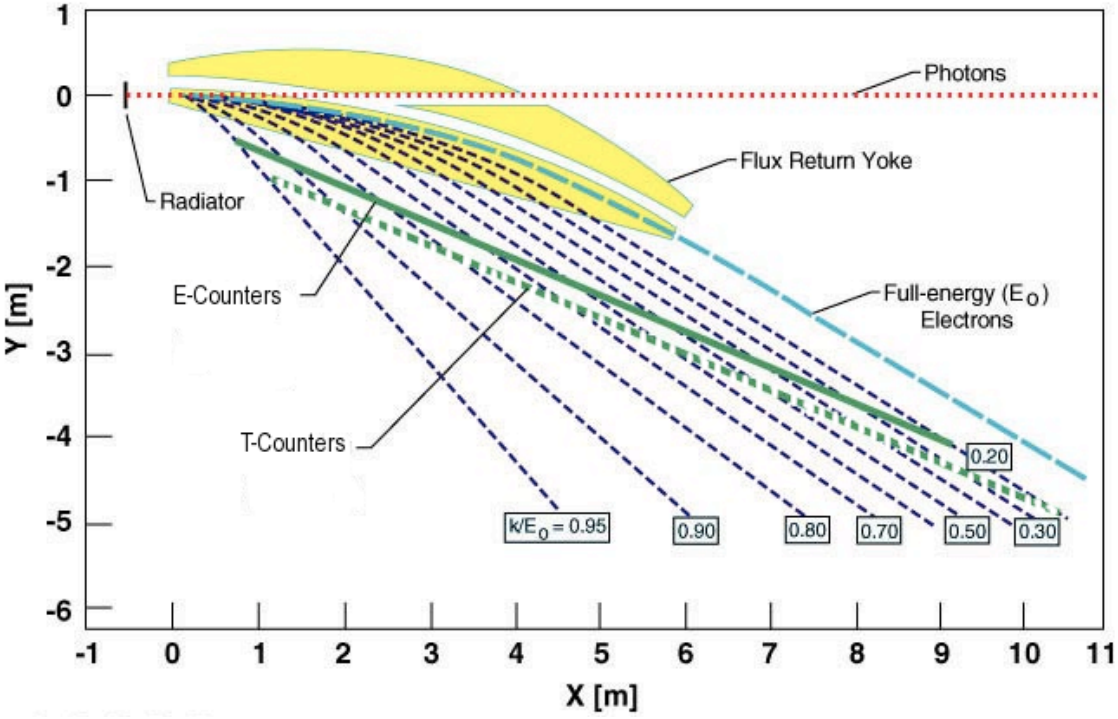

Figure 19: Layout of Hall B photon tagging system. The radiator produces real photons from bremsstrahlung radiation of the incident electrons. The tagger magnet removes the remaining electrons and leave a pure photon beam that gets trimmed by passing through several collimators.

Radiator

The most upstream component of the tagger is the radiator. The radiator ladder consisted of four different very thin gold foils ranging from 10^{-6} to 10^{-4} radiation lengths, during the TPE test run. The large atomic number of gold insures higher bremsstrahlung cross section, and the small thickness keeps the energy loss of recoil electrons as low as possible and therefore increases the energy resolution.

Tagger Spectrometer (Magnet and Hodoscope)

In order to separate the electrons from the bremsstrahlung photon beam, a uniform-field dipole magnet follows the radiator with a maximum deflection angle of 30°, while the photons proceed straight through the beamline and toward the target. The magnet can operate at a full field of 1.75 T (6.1 GeV energy) with a current of 2400 A and an intrinsic momentum resolution of 2×10^{-4}. This magnet has been designed to send full energy electrons (ones that have not interacted in the radiator) directly down to the tagger dump. The scattered electrons that have less energy, are bent with a larger angle and hit two hodoscope planes for energy and timing measurements. These measurements will serve in tagging the photons and precisely relating them to the correct beam bunch. See Fig. 19 for a schematic drawing of the Hall-B tagger.

The focal-plane hodoscope consists of two planes made of scintillator detectors. The first plane is called the "E-plane" for energy measurements and the second plane "T-plane" located directly below the E-plane is used for timing measurements.

The information from these counters is used for coincidence studies to identify the good event trajectories [31]. The tagger magnet was simply used for disposing of the electrons in the TPE experiment, and the spectrometers were not in use.

2.2.1.2 Beam Monitors

Different types of monitoring devices have been positioned along (upstream or downstream) the Hall B beam pipe to measure the beam quality and position, and try to improve it as much as possible. They are briefly discussed below.

Beam Position Monitors

Three beam position monitor (BPM)s each made of three position sensitive RF cavities operate along the beamline at 1497 MHz. The cavities are designed similar to the CEBAF separator cavity and achieve a high sensitivity to beam position. They are normally located at 36.0, 24.6 and 8.2 m upstream from the CLAS target. Each BPM provides a measurement of (x, y) position coordinates and intensity of the beam with a rate of about 1 Hz.

This system has a resolution better than 1 μm and is capable of handling beam currents from 1 nA to 1000 nA. The recorded position and current information is continuously used in feedback loops to keep the beam centered on the target at all times and inserted into the data stream every 20 s [29].

During the TPE experiment only the most upstream BPM was in use to measure the incident electron beam position before it hit the radiator where the beam has a non-zero net charge [32].

Harps

The harps consist of two very thin wires (20 and 50 μm W, 100 μm Fe) that lie along the x (horizontal) and y (vertical) axes and move across the beam to monitor the beam profile. This is done by detecting the scattered electrons via Cherenkov light using PMTs. The motion of a harp is controlled by a stepper motor. Because harp scanning interferes with the beam, it should be done at the time when the experiment is not running.

There are three harps positioned at 36.7, 22.1 and 15.5 m upstream from the CLAS target. However, the TPE experiment only utilized the second harp (harp-tagger) just upstream from the tagger magnet. The typical width of the beam was about $\sigma < 0.5$ mm, at the tagger harp position.

2.2.1.3 The Cryotarget

The target is positioned along the beamline at the center of the CLAS detector. Many targets with different materials and sizes have been used in different run periods according to the particular needs of the experiments. The TPE experiment used a cylindrical 20-cm-long, 6-cm-outer diameter mylar cell filled with liquid hydrogen. The hydrogen was kept in liquid phase by the use of a cryogenic system. This system included a copper heat exchanger bolted to the target cell that was kept cool by liquid hydrogen and liquified the target hydrogen. The temperature of the target was kept at about 20.5° K and the average pressure was 1160 mbar. The target density was 0.0708 g/cm^3. Fig. 20 shows the actual TPE target cell as well as an engineering drawing showing the design and dimensions [33].

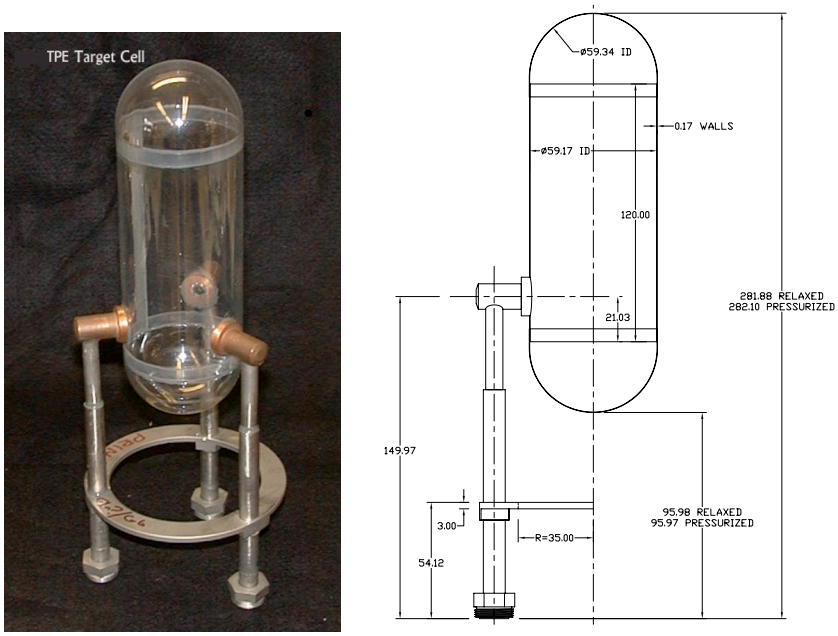

(a) (b)

Figure 20: TPE liquid hydrogen target cell, (a) Photograph of the TPE target cell. The mylar container is attached to hollow stainless steel legs with copper nozzles. (b) Engineering drawing of the TPE target with dimensions in mm [33].

2.2.2 Detector System: CLAS

The CEBAF Large Acceptance Spectrometer (CLAS) is the Hall B detector system used for observing the reaction products of the beam and the target. It is composed of several types of detectors, each of which helps define particle characteristics such as type, trajectory, momentum, energy, and timing. The unique design of CLAS has a number of important advantages. It allows good momentum resolution for charged particles ($\delta p/p = 0.45 - 0.75\%$) and has a large angular coverage. Fig. 21 shows a schematic picture of CLAS. Each detector layer will be discussed in detail in this section.

2.2.2.1 The Toroidal Magnet

The super-conductiong toroidal magnet can be considered the heart of CLAS detector system. This magnet is 5 m in length and 5 m in diameter and is made of six kidney-shaped super-conducting coils that are arranged around the beam-line with the target at

the center point. Therefore, the magnetic field produced is in the azimuthal angle (ϕ) direction. The geometry of the magnet (shown in Fig. 22), provides a field-free central volume that allows the use of polarized targets. At the maximum design current of 3860 A, the magnetic field can reach 3.5 T. However, the routine runs do not exceed 87% of the maximum current (3375 A). The current was ±1500 A during the TPE experiment. Each of the six coils consist of 4 layers of 54 turns of NbTi/Cu conductor. Super-critical helium is used to cool them to temperatures of about 4.5° K.

The magnetic field produced by the CLAS torus bends charged particles in the Region 2 drift chambers thus enabling reconstruction of particle momenta, which is very important in data analysis [29].

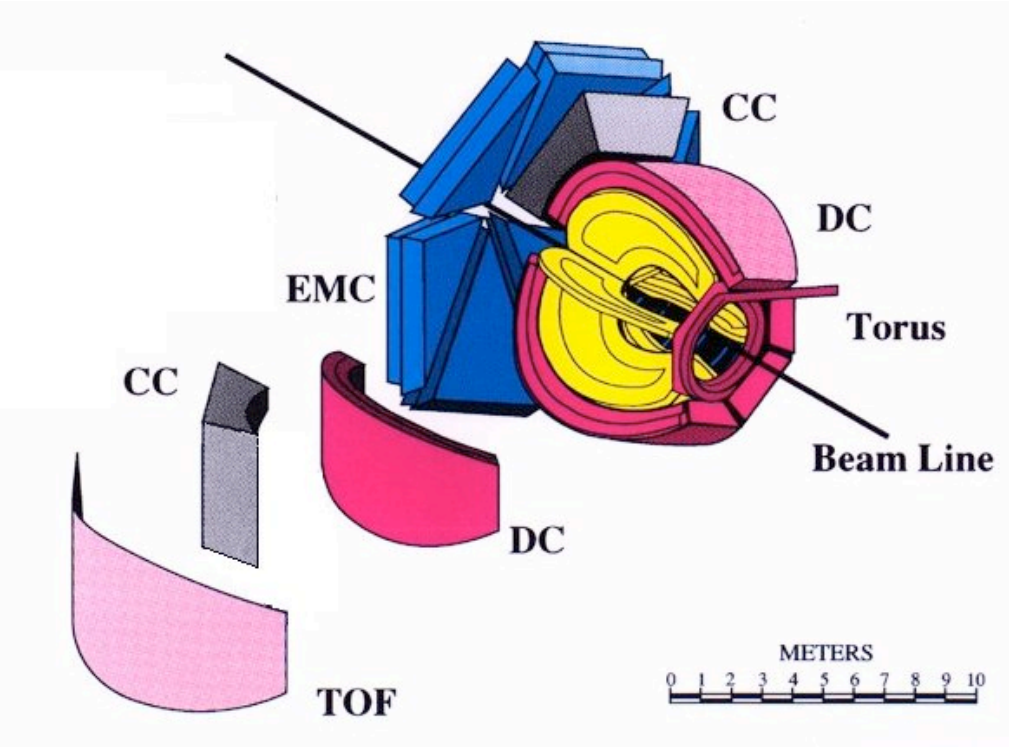

Figure 21: Schematic view of CLAS detector in Hall B. The target is located at the center point of the spectrometer, surrounded be 3 regions of drift chambers (DC) (pink), torus magnet coils (yellow), Cherenkov counters (CC) (grey), time of flight counters (TOF) (purple) and electromagnetic calorimeters (EC) (blue) as shown.

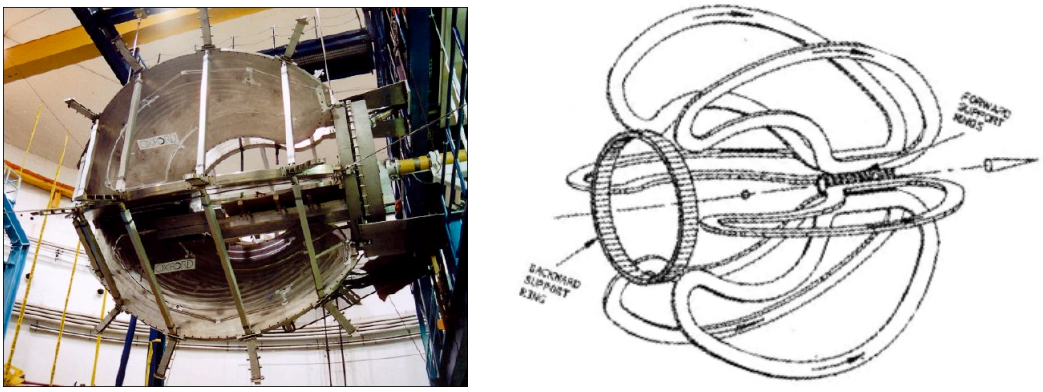

(a) (b)

Figure 22: CLAS toroidal magnet coils, (a) A photograph and (b) schematic drawing of these coils that produce a toroidal magnetic field in azimuthal direction about the beamline.

2.2.2.2 Drift Chambers

Tracking of the charged particles within the CLAS detector system is provided by three layers of drift chambers (DCs) stretched from 8° to 142° in the polar angle. These layers are called "regions" and are placed at radial distances of 0.7, 2 and 4 m from the target for regions 1, 2 and 3 respectively. Each region is divided into six independent chambers by the geometry of the torus magnet. These are called "sectors". The six "Region 1" sectors are placed inside the magnet coils, surrounding the target in an area of low magnetic field. The "Region 2" sectors are located in between the coils in a high magnetic field area, and "Region 3" sectors are outside the magnet coils to determine the final track positions. Wires are strung between the two endplates inside each wedge-shaped sector (see Fig. 23) that are parallel to their adjacent magnet coil. Thus, the endplates of a chamber are at a 60° angle with respect to each other. The wires display a hexagonal pattern called drift cells. Each cell consists of a 20 μm gold-coated tungsten sense wire surrounded by six 140 μm gold-plated aluminum field wires. All sense wires are kept at a positive potential and field wires at a negative potential by a high-voltage system. The absolute value of the negative potential is half of the positive one. There are a total of 35,148 individual drift cells within the 18 drift chambers.

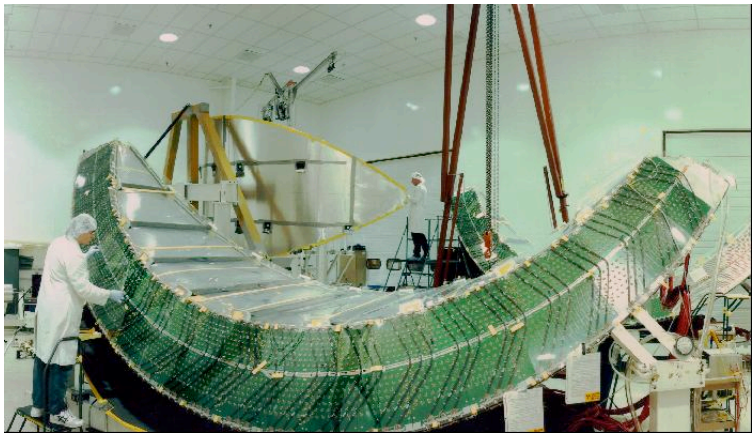

Figure 23: The process of stringing wires for a single DC Region 3 sector. Each R3 sector contains 2,304 cells and the same number of sense wires [34].

For better tracking resolution, each region is grouped into two "superlayers" each consisting of six layers of wires. The axial superlayer wires are along the magnetic field and stereo superlayer wires are tilted by a 6° angle to determine azimuthal information. The Region 1 axial superlayer is an exception and consists of four sense wire layers. In addition, a layer of guard wires surround every superlayer and their voltages were adjusted to reproduce the electric field of an infinite grid of cells. This layout helps minimize the effect of nearby grounded surfaces. Additionally, the electric field is the same for all the sense wires in a sense wire surface [35]. Figs. 24(a) and 24(b) show the wire layout in detail.

Each of the 18 chambers is filled with a mixture of 90% Argon and 10% CO_2 and maintained at constant pressure. This mixture was selected because of the high saturated drift velocity (> 4 cm/μs), minimal multiple scattering, and good efficiency.

When a charged particle passes through the drift chamber volume, it causes the gas to ionize into electron-ion pairs. The electrons then drift toward the sense wires and produce signals, which are sent to a series of readout electronics. First, the signal is fed to preamplifiers located on printed circuit boards that are mounted on one side of each chamber. They are then read out by amplifier/discriminator boards (ADBs). Discriminated pulses are transfered to time to digital converters (LeCroy 1877 TDCs) for timing information and digitization.

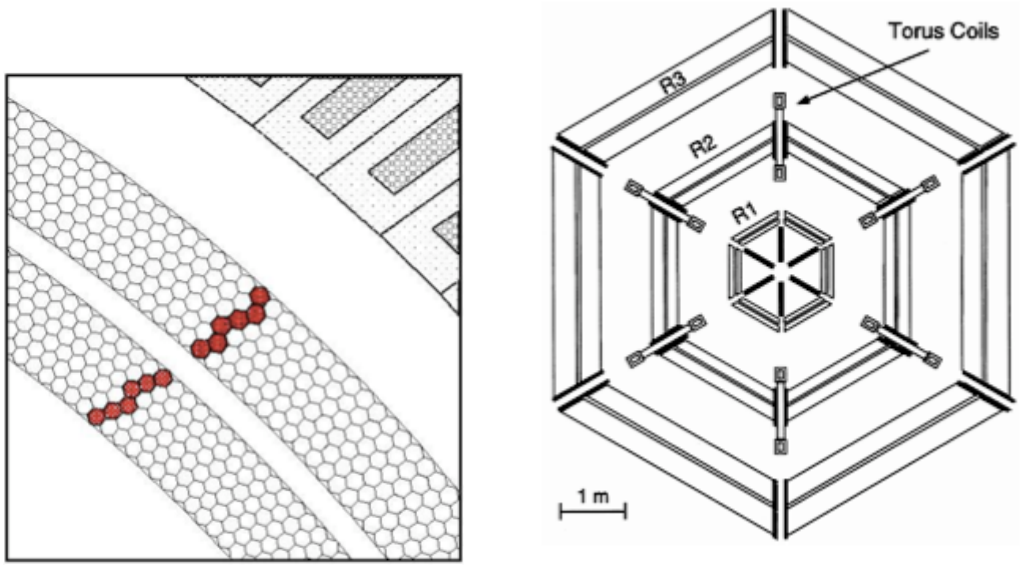

(a) (b)

Figure 24: Drift chamber layers, superlayers, and sectors.(a) A drawing of the two superlayers of Region 3 drift chambers. Each superlayer consists of six layers of drift cells. Each hexagonal cell has a sense wire in the center and six field wires at the vertices. The red trail shows a reconstructed track passing through this region. The front edge of Cherenkov counters are visible on the top right. (b) Cross-sectional view of the CLAS drift chambers looking down the beamline that shows the six different sectors, enforced by the geometry of the torus coils [29].

Track reconstruction is performed in two stages. The first is called "hit-based" tracking where the wire hits are connected across all regions of a sector to form a track. In the second stage that is "time-based" tracking, the flight time information of tracks from the target to the time of flight counters are used to correct the drift times. These are then converted to drift distances. The corrected hit positions are fit to give rise to the final track parameters. This procedure is called DC calibration and will be discussed in detail in chapter 4.

The tracking efficiency is the probability of a track being identified as it passes through the drift chamber. It is typically more than 95%. The tracking resolution affects the angle and momentum resolution and is smeared as a result of: multiple scattering along the particle trajectory, geometric misalignments, and the single-wire position resolution. The single-wire or chamber resolution is the uncertainty in the track position within a cell and is about 310, 315 and 380 μm for Regions 1, 2 and 3 respectively [29, 34].

2.2.2.3 Cherenkov Counters

In order to trigger the electronics and to separate electrons from negatively charged pions, six individual Cherenkov counters (CCs) are used in each of the six sectors of CLAS. The CLAS Cherenkov counters are threshold counters and give a signal only when the traversing particle's momentum exceeds a certain limit. They are located approximately 4 m from the the target and designed to cover the polar angle range of 8° to 45°. The photomultiplier tubes (PMTs) are placed in the regions shadowed by the magnet coils to ensure that the solid angle is maximized. Also, as much available space as possible is filled with mirrors for the same reason. The light collection optics are designed to focus the light in the ϕ direction. Each sector is divided into 18 segments in polar angle (θ) and each segment into two modules by the symmetry plane. There are 12 modules in each θ segment for all the sectors combined and a total of 216 modules in the Cherenkov detector. The layout of a single CC sector is shown in Fig. 25.

Each light collection module includes two focusing mirrors (one elliptical and one hyperbolic), one cylindrical mirror, a "Winston" light collection cone, and a 5 inch Phillips PMT that is attached to the Winston cone and used to detect the Cherenkov light.

The detector is filled with perfluorobutane (C_4F_{10}) for several reasons. This gas has a high index of refraction (n=1.00153), which results in high photon yield, high pion momentum threshold of about 2.5 GeV/c and very good light transmission ability at short wavelengths. The gas system maintains a constant pressure in the chambers at all times.

When a electron passes through the gas in the Cherenkov chamber with a velocity higher than the velocity of light in that medium, a forward going cone of light is produced. The number of produced photoelectrons depend on the index of refraction of the medium and is about 4-5 for an indending electron. The PMTs then gather these photons, producing a signal that is sent to the readout electronics.

The anode signal from all PMTs are split into two signals, one of which is fed to a discriminator whose threshold is set manually. The discriminated signal is then sent to a 64-channel FASTBUS time to digital converter (TDC) for timing information. The other signal is brought to an analog to digital converter (ADC) to determine the number of pho-

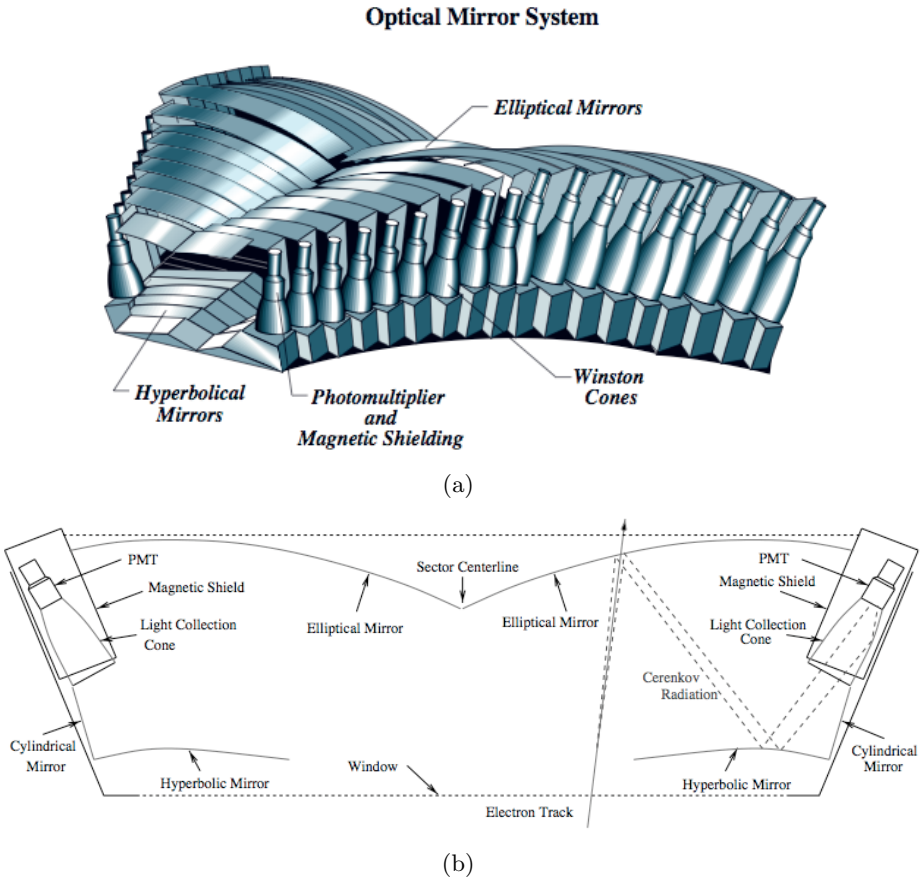

Figure 25: A single sector of the CLAS Cherenkov counter. (a) An overall picture of a single CC sector, showing the 18 separate segments. The PMTs are located on two sides of the chamber, hidden in the area obscured by the magnet coils, (b) Diagram of a segment that consists of two modules each have a separate PMT. A typical electron track is shown that produces Cherenkov light that is collected by the PMT [29].

toelectrons from the PMTs. The signal from the PMT dynodes for individual detector segments are summed by overlapping two segments of each adjacent four segments. Therefore, each sector contains 8 sums of 4 overlapping segments. The signal from each of the sums is split and sent to two CAMAC discriminators with individual threshold settings to "high" and "low". The information is used in the Level I trigger system within 200 ns. Each Cherenkov signal in coincidence with the electromagnetic calorimeter readout provides enough information to identify possible electron hits. More detailed information is available in [29, 36]. The Cherenkov detectors were not in use during the TPE run.

2.2.2.4 Scintillating Time of Flight Counters

The scintillating time-of-flight counter consists of arrays of scintillators arranged in 4 panels for each of the six CLAS sectors. It is a very important part of the detector used to determine the time-of-flight (TOF) for particle identification and also to provide information to the Level I trigger system. The scintillator semi-spherical shell is located at almost 4.5 m from the cryotarget, sandwiched between the Cherenkov counters and electromagnetic calorimeter, and spans 8° to 142° in polar angle. The scintillators are 5.08-cm-thick and give a large signal for the minimum-ionizing particles passing through. Fig. 26 shows a single sector of the TOF counter that consists of 57 scintillators. Scintillators 1-23 are 15 cm wide, mounted on the first panel, which corresponds to scattering angles less than 45° and is therefore called "forward angle". The remaining 3 panels are "large angle" and are 22 cm wide. The scintillator lengths vary from 32 to 445 cm. Due to the fast time response and low light attenuation, Bicron BC-408 was used as the scintillator material. The choice of this material optimizes the time resolution over the volume of the counters.

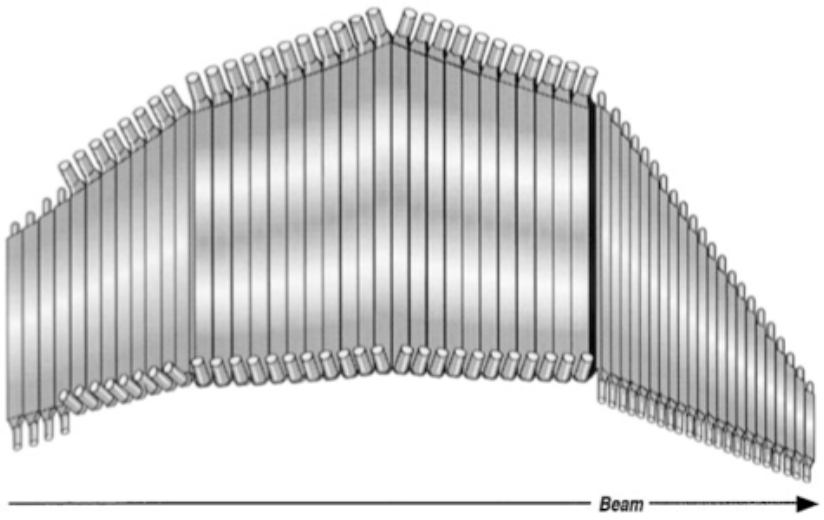

Figure 26: A single sector of the TOF counter, showing the four panels and scintillator paddles within each of them. The panel 1 scintillators are narrower than the others.

To collect the light from scintillators, two kinds of photomultiplier tubes were utilized. For the forward angle region, 2-inch Thorn EMI 9954A PMTs were connected to both ends of the scintillators. Philips XP4312B/D1 PMTs are used for the large angle region where the requirement for time and angular resolution is reduced by the longer particle flight time. The non-active regions of the TOF counters are hidden behind the toroidal magnet coils and well shielded from the effect of fringe magnetic fields.

The TOF readout electronics are triggered when a track passes through with energy higher than a certain preset value. Signals from the two PMT dynodes are combined in a pre-trigger board and sent to be used in Level I trigger. The anode signals are discriminated and sent to LeCroy 1872A FASTBUS TDCs in order to determine the time for the event. Time resolution for each scintillator depends on its length and ranges from 80 to 160 ns. Longer counters have poorer (larger) resolution. The time information in combination with the track lengths from DCs, determine the particle velocities [29, 37].

2.2.2.5 Electromagnetic Calorimeter

The forward electromagnetic calorimeter (EC) is the outermost component of CLAS, located downstream of the TOF counters at a radius of about 5 m from the cryotarget. The main purposes of the EC is to identify and trigger on electrons with energies higher than 0.5 GeV, to detect the photons with energies above 0.2 GeV, and to detect neutrons. The EC covers the forward polar angle range of 8° to 45° just like the CC. To match the rest of the CLAS detectors, the EC is divided into six separate modules, one for each sector. Each module has the shape of a nearly equilateral triangle, and is made of alternating layers of 10-mm thick BC412 scintillator strips and 2.2-mm thick lead sheets (for shower conversion). The total thickness has been chosen to be 16 radiation lengths. The EC displays a "projective" geometry with the area of the successive layers increasing as the distance from the target increases.

Each scintillator layer consists of 36 strips parallel to one side of the triangle, for readout purposes. These strips are oriented with a 120° relative angle in successive layers. The different scintillator orientations (views) labeled U, V and W are shown in Fig. 27(a). Each

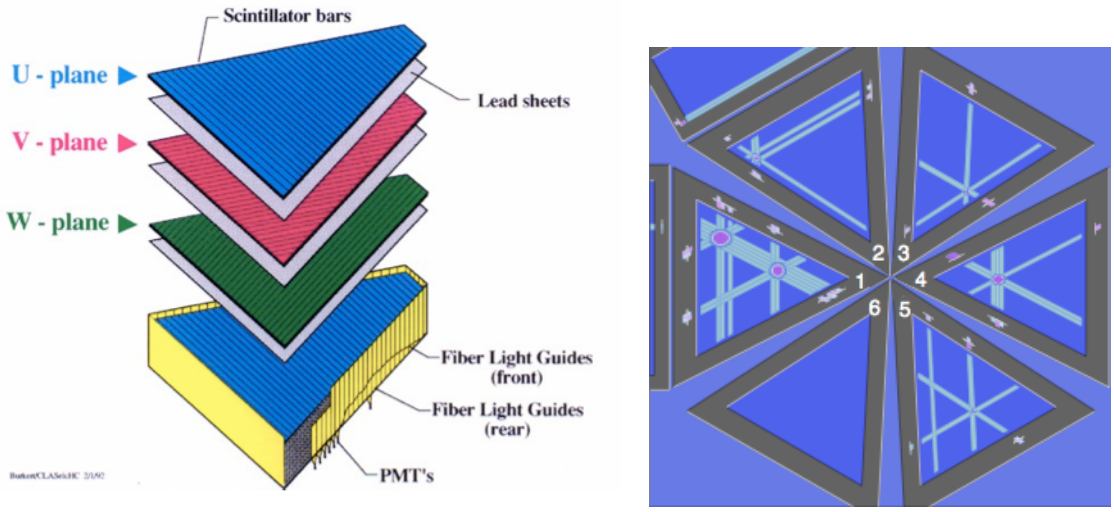

(a) (b)

Figure 27: Exploded view of a single EC module, showing (a) U, V and W orientations, (b) Hit reconstruction in EC sectors. Sectors 2, 3, 4 and 5 display one hit whereas sector 1 shows 2 hits.

view is further divided into 13 layers to provide stereo information on the location of energy deposition. These sub-layers are grouped into 5 layers of inner and 8 layers of outer stacks, for longitudinal sampling of the shower to improve electron/hadron separation. This configuration allows fine hit position, as shown in Fig. 27(b), and energy spread reconstruction. Each module requires 36(strips)×3(views)×2(stacks)=216 of photomultiplier tubes, which are coupled to the scintillator strips using fiber-optic light readout units, and mounted on the back of the calorimeter.

The first signal split from the PMT anodes are read out by LeCroy ADCs and TDCs. The TDC signals are provided by leading edge discriminators and used for timing information. The ADC signals are used to determine the energy deposited. The second anode signal runs to the pre-trigger board to be used in Level I trigger system. Electron triggers depend on the total energy deposited in the calorimeter, therefore fast analog sums of all the PMTs in every module are obtained. Different combinations of U, V and W views are obtained for inner and outer stacks. Level I electronics can trigger on different sectors using different combinations of total or partial energy deposit sums that pass a certain threshold.

The photons and neutrons within the calorimeter are differentiated by using their timing information, whereas electrons and pions are distinguished by observing their energy deposition pattern (electrons deposit most of their energy in the inner EC layers but pions deposit it uniformly). Particles are further identified using parallel information from DC, CC and TOF counters. The energy resolution of the calorimeter is determined to be $\sigma/E = 10.3\%/\sqrt{E(GeV)}$. The average RMS position resolution for electron showers with deposited energies higher than 0.5 GeV is 2.3 cm. The average timing resolution for electrons is 200 ps over the entire calorimeter [29, 38]. The EC information was not used in TPE data analysis.

2.2.3 Trigger and Data Acquisition System

To acquire and record the events of interest while running the experiment, a two-level trigger system is used [29]:

- The Level I trigger processes all prompt signals from the fast PMT channels of CLAS detectors such as CC, SC and EC (as explained before). These detector patterns are compared to preloaded patterns in memory tables for fast response. This trigger is adjustable for individual experiment's needs.

- The events that satisfy the Level I trigger condition, move to Level II for further filtration. It uses DC information for each sector to find "likely tracks" by comparing track segments in each DC superlayer. The Level II trigger is satisfied by either the logical "OR" of the sectors, or by correlating the tracks with Level I trigger information.

In the next readout stage, the trigger supervisor (TS) inputs signals from Level I only (CLASS1) or both Level I and Level II triggers (CLASS2). These signals are used to gate the electronics, which generates a start signal to the PMT TDCs, a gate signal for the PMT ADCs, and after a delay, a common stop signal for DC TDCs. In case of CLASS2 trigger, the trigger supervisor waits about 3.2 μs for the Level II confirmation. If this trigger fails,

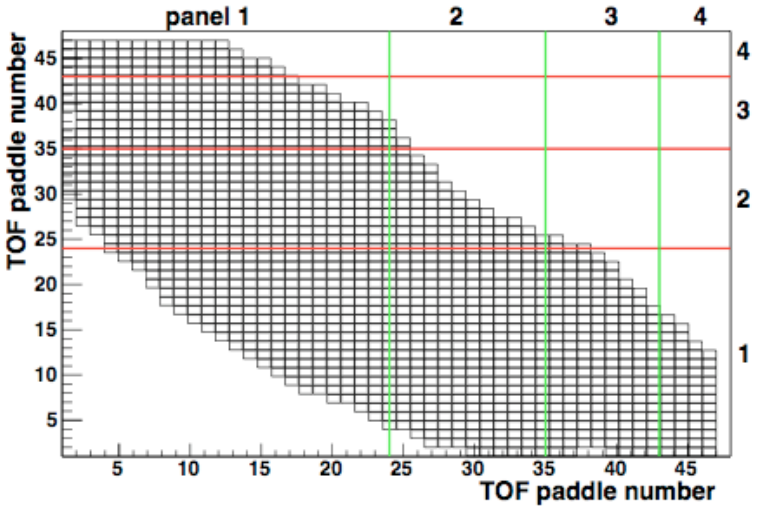

Figure 28: Kinematically allowed TOF panels in the opposite sector trigger configuration. Green and red lines represent the panel borderlines.

it sends a fast-clear to the electronics and resets them. Otherwise it places the event on the readout queue to be sent to the data acquisition system.

The TPE experiment has not utilized the standard CLAS single-electron trigger. That trigger was not appropriate because both elastic scattering products needed to be detected as the photon beam energy was unclear. The usual trigger would cut out a lot of larger angle leptons and therefore limit the kinematic coverage. A new trigger configuration was designed for the TPE experiment and was set to record events with charged tracks in two opposite sectors of CLAS time of flight counters. To avoid TOF occupancy difficulties experienced in the previous background tests, the trigger was set to one hit on panel 1 of TOF ($\theta < 45°$) with the second hit on any panel of the opposite sector (see Fig. 28). Also a minimum ionizing signal was required in the same EC sector as the panel 1 TOF hit. For a few runs only, an additional Level II (drift chamber) trigger was required as well [19].

The CLAS Data Acquisition system (DAQ) receives the data from the trigger supervisor after the required triggers are satisfied and transforms it in several stages. Fig. 29 shows a schematic of the CLAS data flow. The digitized data are collected by 24 Readout Controllers (ROCs) in the detector electronic crates in the experimental hall where the information is translated into arrays of tables for each detector module. These fragments are

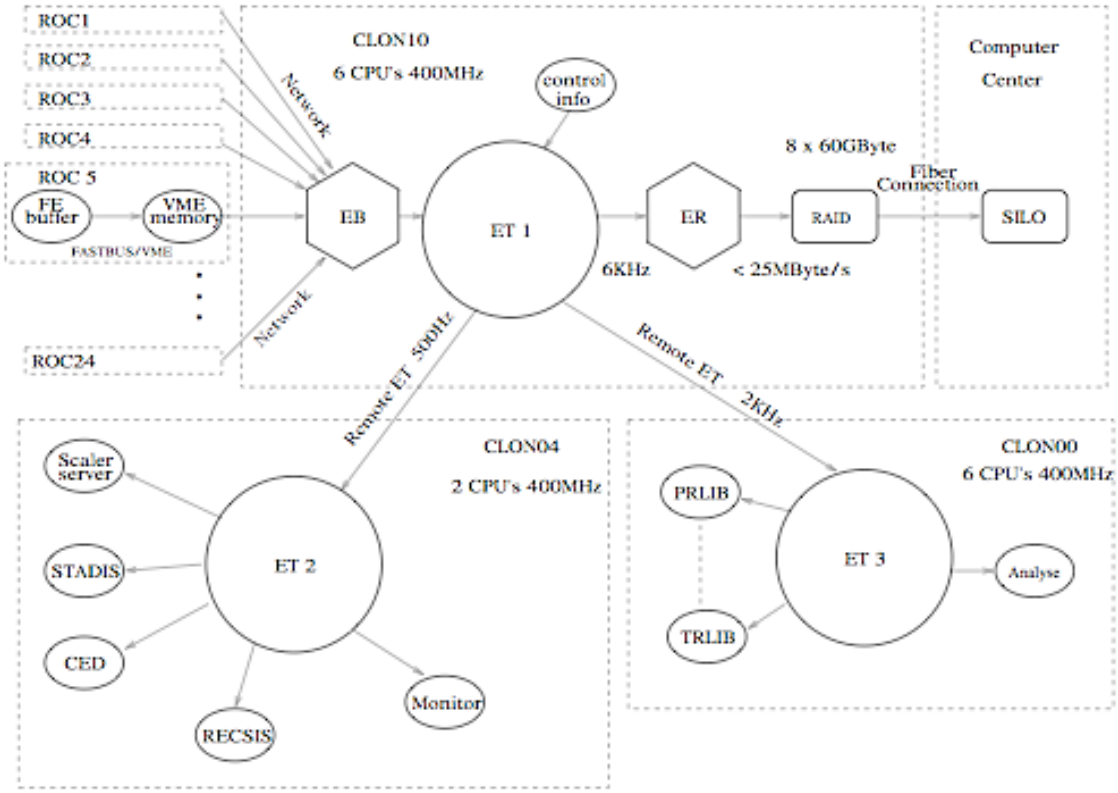

Figure 29: CLAS DAQ data flow schematics, data from the readout controllers are packaged into events by the event builder (EB), accessed remotely using shared memories (ET2,ET3), and eventually saved to silo by the event recorder (ER).

then sent via fast Ethernet line to the CLAS online acquisition computer (CLON10) in the control room. The first acquisition process is the Event Builder (EB), which combines the received fragments and arranges the data into "banks". These are larger tables labeled with the run number, event number, event type, etc. These formatted events are then passed to shared memory where the Event Transport (ET) allows them to be accessed by remote systems. At the final stage, the Event Recorder (ER) places the events in magnetic media (RAID disks) from where it is transferred to the tape silo for permanent storage via optical fiber links. The stored data files are then ready to be accessed by users for offline analysis.

2.3 TPE Beam-line Modifications

As explained in the previous section, due to the unique beam requirements of the TPE experiment, several new components have been added to the standard Hall B setup. These components were carefully designed and installed prior to the run period, and successfully utilized to obtain a combined electron/positron beam. The most important additions to the Hall B beamline discussed in this chapter are the converter, the chicane magnet and the beam profile monitor. In addition, significant changes to the tagger beamline and the shielding configurations were done. Those modifications are discussed in Chapter 3.

2.3.1 Converter

The purpose of the converter is to generate electrons and positrons from the incoming photon beam through the pair production process. The TPE run tested several converters with different materials and thicknesses, installed on a movable stick to find the optimal configuration. The desired converter was required to help increase the luminosity while decreasing the DC occupancy as much as possible. The ladder contained a 1.8×10^{-3} radiation length (RL), a 4.5×10^{-3} RL and a 1.6×10^{-2} RL converter. The first one was replaced with a 5.1×10^{-2} RL gold converter during the configuration tests. The converter stick was placed about 15.8 m upstream of the target. The optimal converter was found to be the latter one of the above, and was chosen due to the smaller background rate and higher luminosity achieved during the testrun.

2.3.2 Chicane Magnet

The best strategy to remove the photons that do not interact in the converter from the beam was found to be the use of a 3-dipole chicane magnet inserted in the beamline just downstream of the converter. The original design was a 4-dipole magnet chicane where the first two served to separate the electrons and positrons, and the next two recombined them while the uncharged photons were stopped by a blocker. In the TPE test run, however, the two middle dipoles were replaced by the pair spectrometer (PS) magnet, which converges

the leptons before they get to the third magnet. The pair spectrometer is conventionally used to measure the beam flux in higher current production runs. The PS magnetic field was set to about ± 0.38 T with a current of ± 590 A. The two surrounding magnets were the so-called "Italian Dipoles" (ID1, ID2) positioned about 2 m upstream and downstream of the PS respectively, with magnetic fields of about ∓ 0.4 T. All the chicane magnet polarities were reversed periodically during the experiment to reduce the systematic uncertainties as will be discussed in the following chapters. The oppositely charged leptons were separated horizontally through the chicane and the photon beam was absorbed by a narrow 20-cm long tungsten photon blocker positioned at the entrance aperture of the PS magnet. The aperture is 0.5 m which is crucial for the experimental acceptance. Either of the separated lepton beams can also be blocked by inserting one of the two "low-energy collimators" as the beam is diverging. They can partially or fully block each lepton beam to limit the low-energy luminosity or to study the energy dependence of the flux for individual lepton beams.

2.3.3 Collimators

A pair of collimators are usually used in the beamline to trim the beam halo. These are devices made from radiation absorbent material with a custom-sized aperture, designed to limit and define the direction and divergence of the beam. Collimators have been used in several locations along the beamline during the TPE run. The photon collimator was located almost 16 m upstream of the target (just downstream of the tagger magnet). Several cylindrical 12-inch-long nickel collimators with different inner diameters (2.6, 8.6 and 12.77 mm) were installed on a movable stick so that the optimal configuration could be chosen. The 12.77 mm collimator was found to produce the lowest background reading at the CLAS time-of-flight counters. In addition, a 3 cm inner diameter lead collimator was installed after the 3rd chicane magnet and a 6 cm diameter one just a few meters upstream of the target. The combination of these collimators resulted in a combined lepton beam of about 8 cm diameter incident on the target [19, 32].

2.3.4 Scintillating Fiber Monitor

The combined lepton beam quality and position throughout the TPE run was monitored using a scintillating fiber (SciFi) monitor installed upstream of the target. This device was custom designed, built and tested at FIU, and shipped to JLab for installation. Fig. 30(a) shows the schematic of this device. It consists of a 6×6 inch aluminum frame with a 1 inch frame width, supporting 32 square (1×1 mm) multiclad Bicron (BCF-12) fibers with 42 cm radiation length. Half of the fibers are positioned horizontally (x-fibers) and half in the vertical direction (y-fibers) for a two-dimentional readout. Each set of 16 fibers were glued to a 16-pixel Hamamatsu H8711 photomultiplier tube that amplified and transfered the signals gathered by the fibers to readout electronics. Furthermore, a slight modification to the online run monitor software (EPICS), allowed the live display of the SciFi readout during the experiment. Fig. 30(b) shows the result of an ID current scan for individual lepton beams (with the other beam blocked), monitored by the SciFi. This allowed the determination of the ID magnet setting that optimized the centering of the lepton beam spot [19, 39].

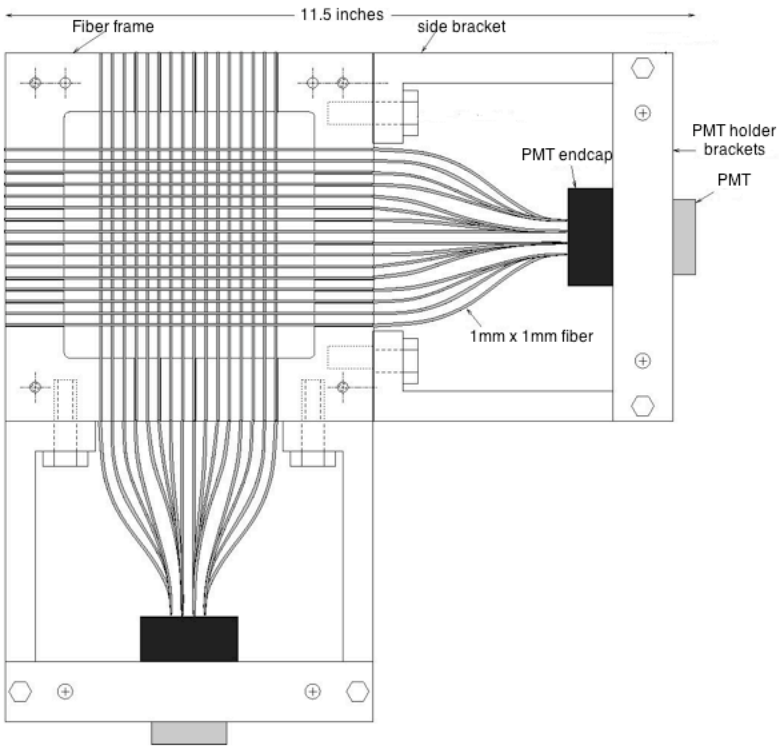

(a)

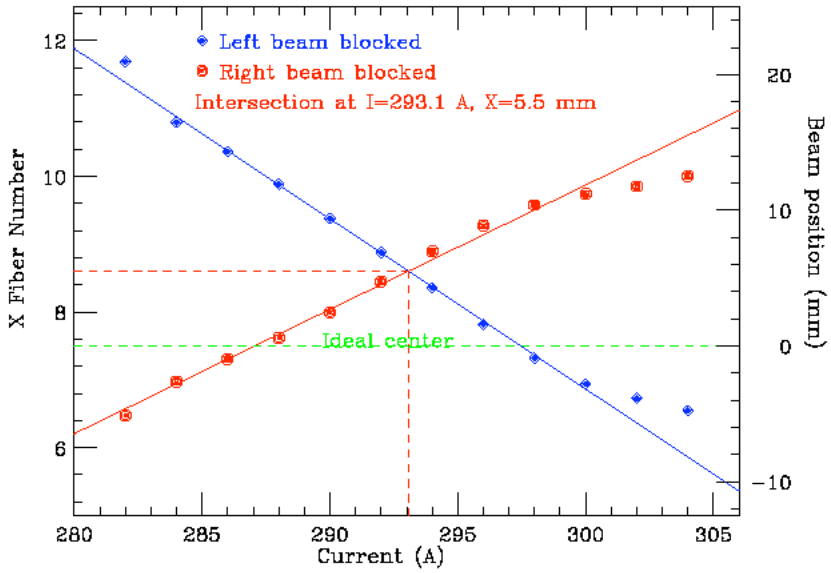

(b)

Figure 30: Schematic of the TPE fiber monitor (SciFi), designed at Florida International University. (a) The PMTs (black squares) are held by supporting frames for x- and y-fibers. (b) Beam position vs. current scan for different ID magnet currents used to find the optimal magnet setting. Lines are fit to points 2-10, with the crossing indicating where the two lepton beams converge.

3 Background Simulations

The issue of excessive background has been a great concern that has threatened the feasibility of the two-photon exchange (TPE) experiment since it was first proposed in May 2004. The production of secondary beams by a large-current primary beam was the main cause of this problem. Several short test runs were performed to address these problems resulting in several conclusions that offered some hope of identifying and eliminating the major sources of experimental background. The experimental observations guided extensive computer simulations that led to the beamline configuration for the test run discussed in this dissertation. Compared to previous test runs, this configuration resulted in a largely improved beam quality and background reduction.

3.1 Brief Test Runs

The first test run was a one-day beam study conducted in July 2004. The goal was to test the background rate observed from a blocked photon beam, using different radiator thicknesses, beam currents and basic shielding arrangements. The effect of using different collimators on the background was also examined. As a result, the sources of background were analyzed by comparing the rates in different detectors such as drift chambers (DCs), time of flight (TOF) counters and electromagnetic calorimeters (EC). Some hot spots were observed in the Region 1 and 3 DC, and sectors 5 and 6 of TOF.

In December 2004 a one-hour long test run took place that focused on the effects of varying the tagger magnet current on the electron beam position (within the tagger) and ultimately on the background rate. The data taken confirmed the direct dependence of the background observed in sectors 5 and 6 of ToF and Region 3 DC, on the tagger magnet current. This was believed to be due to the primary electron striking the tagger vacuum box exit flange.

Moreover, in order to identify the type and intensity of background radiation at different locations of the setup during the photon run with a powered tagger magnet, 20 TLD (ThermoLuminescence Dosimeter) badges were installed in different locations along the

beam and tagger lines. They were tested in June 2005, where the results suggested that thermal neutrons are not a source of concern for the occupancy of sectors 5 and 6 of the TOF counters in that range of luminosity. It was determined that a large source of the TOF background was photons originating from the tagger vacuum box flange. To further study and narrow down the photon and neutron flux sources, four neutron detectors and two scintillators were placed in the hall during an August 2005 test run. The results of this test run, which included more TLDs dispersed throughout the hall, also confirmed the tagger flange to be a source of photons and neutrons. Photon and electron backgrounds were found to originate along the beamline at the collimator and pair spectrometer region.

During successive test runs, some simulations were also in progress. A GEANT3 simulation toolkit was initially used and was later switched to GEANT4 because of the more precise physics and secondary interaction packages. This simulation tool is explained in more detail in the following section.

3.2 GEANT4 Simulation Toolkit

3.2.1 Introduction

GEANT4 is a software toolkit to simulate the interaction of particles with matter. This package was developed at CERN and maintained by a worldwide collaboration of physicists and computer scientists. GEANT stands for **GE**ometry **AN**d **T**racking. This package was originally written in FORTRAN (GEANT3)[40], and was transformed to the more sophisticated object oriented C++ language, by a joint project at CERN and KEK in 1994. Since then GEANT4 has gone through continuous development, with the latest version being 9.0 released in 2007. GEANT4 has numerous areas of application such as particle physics, astrophysics, nuclear physics, medical physics and imaging, radiation studies, and many more. The user friendly geometry construction abilities, along with detailed particle transportation and physics models, make this software an ideal tool to design and test experimental setups. The following two sections contain the relevant features of GEANT4 and are condensed from the GEANT4 manual [41].

3.2.2 Structure

In designing a large software system such as GEANT4, it is essential to partition it into smaller logical units. In object-oriented programming, class categories are used to create logical units. Each of these categories contain clusters of closely related classes. However, the class categories themselves are weakly related. This property assures easier and more efficient software organization and development. The structure of class categories summarized below is shown in Fig. 31.

1. **Run and Event:** In GEANT4 "run" is the largest unit of simulation. It is made up of a sequence of events determined by the user. A run is represented by a *G4run* class object. Also *G4RunManager* handles the actions taken during a run. Similarly a *G4Event* represents an event whose object contains all input and outputs of an event, such as primary vertices, trajectories, hits and digitization collections. This class object is constructed in *G4RunManager* and sent to *G4EventManager*. A set of primary particles need to be sent to *G4Event* via a user supplied *G4VUserPrimaryGeneratorAction* concrete class, that is the event generator for GEANT4.

2. **Tracking and Track:** The *G4TrackingManager* does not handle the direct transportation of particles as it may sound. It serves as a transit between the event manager from which it receives the track and lower hierarchical objects in the tracking category such as *G4SteppingManager*, *G4Trajectory* and *G4UserTrackingAction*. A step is a unit of particle transportation through materials whose length is proposed by discrete or continuous processes. Therefore, *G4UserTrackingAction* plays an important role in particle tracking. *G4Step* stores information such as the coordinates and volumes containing the two endpoints of each step. It also contains the changes in track properties between these points such as energy, momentum, etc. Also *G4Track* keeps the final status of the particle after the completion of each step.

3. **Geometry and Electromagnetic Field:** The detector definition in GEANT4 requires the representation of its geometrical elements, materials and electronics properties. A "Logical Volume" defines the properties of a detector, such as its volume

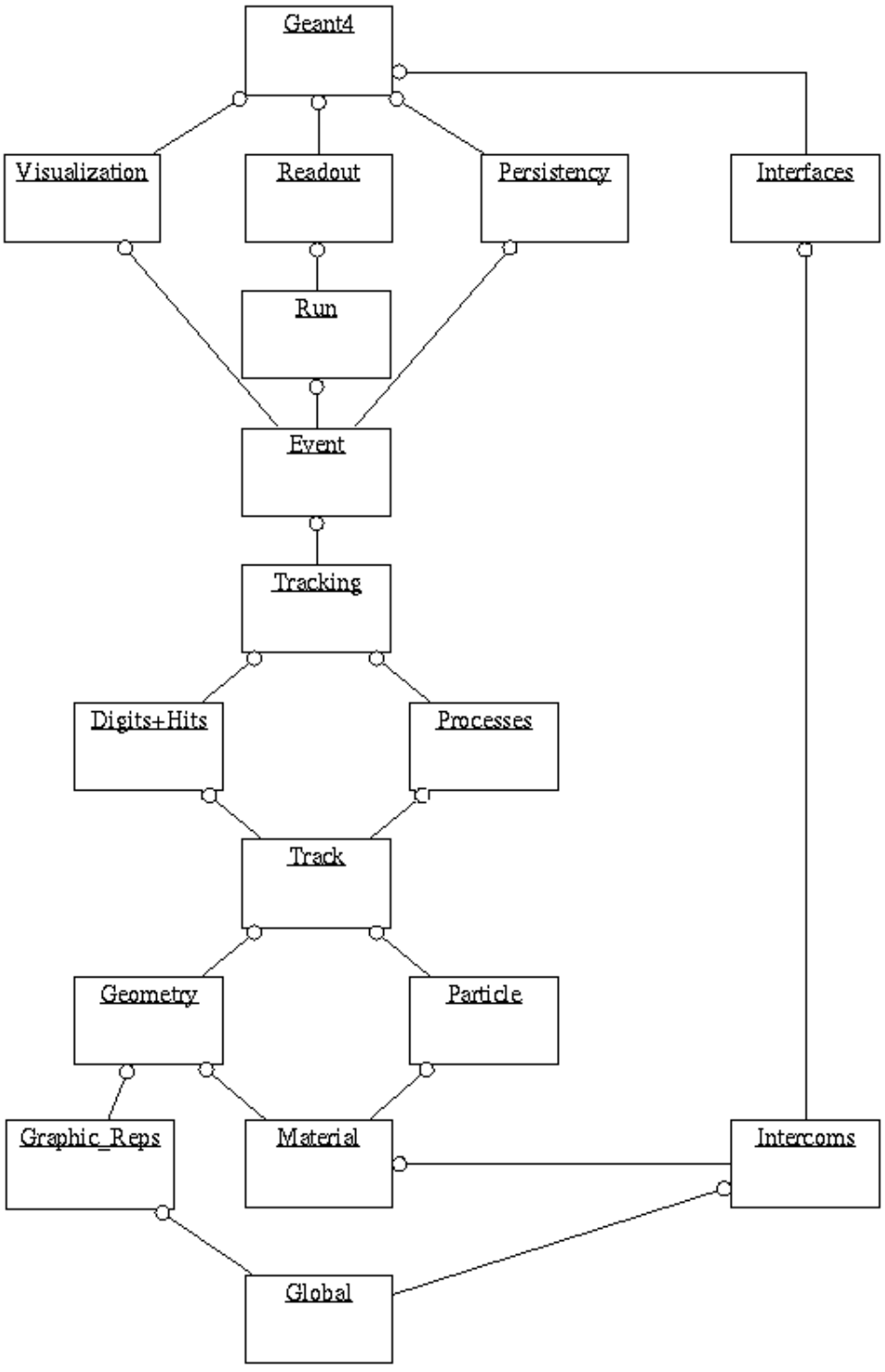

Figure 31: Diagram of GEANT4 class categories and their relations. The circle at the end of a straight line means that the class category with the circle uses the category at the other end of the line.

shape and size, material, visualization attributes, and electromagnetic field. A "Physical Volume" represents the spatial positioning as well as the logical information. The placement of a vlolume also involves the definition of a transformation matrix for the volume to be positioned. As mentioned above, a user-defined electric or magnetic field can be associated with any logical volume. In order to propagate a track inside a field, the equation of motion of the particle in the filed is integrated. The integration accuracy can be adjusted by the user.

4. **Materials:** In nature materials are made of elements, and elements are made of isotopes. Each of these classes in GEANT4 has a data table that describes their properties. For instance *G4Isotope* includes properties of atoms, *G4Element* the properties of elements and *G4Material* the macroscopic properties of matter such as density, temperature, pressure and etc. Many different materials and elements can be created and named by the user, utilizing the above classes to define logical volumes of detector elements.

5. **Particle Definition:** There are a large number of elementary particles and nuclei defined in GEANT4. Various particles are listed in leptons, mesons, baryons, ions quarks and gluons categories. The properties of these particles such as mass, width, spin, isospin, parity, lifetime, etc can be viewed by utilizing the *G4ParticleDefinition* class. Also the kinematic information for a particle such as momentum, kinetic energy, proper time, etc. can be retrieved from *G4DynamicParticle* class.

6. **Physics:** Physics processes describe how particles interact with matter. They play an important role in particle tracking. For instance, the step length from one point in space-time to the next can be determined by calculating the probability of interaction based on the cross section information for each process. This information is in the form of tables of cross sections, energy losses, and other physics values. These tables are built for all the processes before each event loop for each material. Also, production cut values are important for some of the processes such as standard electromagnetic and hadronic interactions.

G4VProcess is the base class for all physics processes. Each process implements virtual methods of this class to determine when an interaction should happen and decribe that interaction.

Some major categories of physics processes implemented in GEANT4 are briefly discussed below. More interactions can be defined and assigned to a particle type by the user.

- *Electromagnetic Interactions:* Standard electromagnetic interactions include photon processes such as Compton scattering, photo-electric effect, gamma conversion and muon pair-production, electron/positron processes such as bremsstrahlung, different types of positron annihilation, sychrotron radiation, ionization, and delta ray production. Standard electromagnetic interactions also include muon and hadron/ion processes and multiple scattering. Low energy electromagnetic processes, interactions of muons and "X-ray production" processes also contain specific sub-groups of interactions.
- *Hadronic Interacions :* Different hadronic processes are implemented in GEANT4 depending on the status of the hadron (at rest, in motion, etc). Each process uses a specific data set that encapsulates methods and data to calculate the total cross sections. User specified data store are also defined to allow the user to combine data sets and arrange their priority for different energy range, particle or material. Each hadronic process such as hadron elastic and inelastic scattering, fission or hadron capture processes, is equipped with a default cross section data store. In case of inelastic collisions, physics models explain the distribution of secondaries. Parametrization driven model is a major group based on the GEANT3 GHEISHA package, that treats both low and high energy interactions. Detailed data-driven and theory-driven models are also available. Some examples are, parametrization (LHEP), Quark Gluon String (QGS) and Kinetic model (Binary Cascade).

- *Decay Processes:* Particle decay can happen either at rest or in motion. Information on the decay modes of each particle is stored in decay tables. Each mode corresponds to various decay channels when coupled with its branching ratio. Many models exist for heavy particle decay that cannot be defined by the GEANT4 decay process, and are provided by event generators or external packages.
- *Optical Photon Processes:* Optical photons whose wavelengths are much greater than the atomic spacing, are treated in a distinct manner from the higher energy gammas. Processes such as reflection, refraction, Rayleigh scattering, Cherenkov effect and scintillation are associated with these photons. The optical properties of the medium are stored in data tables that can be constants or a function of photon's wavelength.

For detailed desciption of all the physics processes and their implementation method, please refer to GEANT4 physics reference manual [42].

7. **Hits and Digitization:** A hit is a snapshot of the physical interaction of a track with the sensitive region of a detector. It records step information in the detector such as position and time of the step, momentum and energy of the track, and energy deposition of the step. *G4THitsCollection* class represents a vector collection of user defined hits. A user defined sensitive detector that is associated with a logical volume, is in fact a trigger to activate the hit objects when a track propagates through it. On the other hand, a digit is created using the information of one or more hits and/or other digits by a digitizer module that is not associated with any volume. Digitizer modules are mainly used in simulating ADC and TDCs, readout schemes, trigger logics and pile-up.

8. **Visualization:** The detector geometries, tracks and hits can be visualized by high quality graphics packages supported by GEANT4 such as OpenGL, DAWN or WIRED. This allows users to utilize a flexible camera to browse through complex geometries, debug the overlaps and view the particle trajectories interactively.

9. **Interfaces:** Various types of user interface commands are available in GEANT4. These include:

   - *Graphical User Interface (GUI):* The GUI creates a control panel to manage the visualization. Different buttons and sliders can be designed for convenient navigation through the graphics window. This inludes rotation in polar and azimuthal angles, translations to four directions, zoom, event triggers and many more.
   - *Macro File (.mac):* Different user controls can also be implemented into macro files via /control/execute *command*. A long list of built-in commands includes /units/, /geometey/, /tracking/, /event/, /run/, /vis/ and etc. Each of these have their own list of sub-commands to specify the required action.
   - *Hard Code(C++):* Commands can be also hard coded using ApplyCommand method of *G4UImanager* class. Output streams from *G4cout* and *G4cerr* are examples of this class controling the flow of the run.

3.2.3 User Definitions

The GEANT4 package does not include all that is required to start with. The content of the main program varies according to the need of a given simulation project. Therefore it must be supplied by the user. Several other initialization and action classes are also mandatory to be defined by the user. These are user DetectorConstruction, PrimaryGeneratorAction and PhysicsList. *G4RunManager* checks for the existence of these mandatory classes. Some other user actions are optional to be supplied. These include, user RunAction, EventAction, StackingAction, TrackingAction and SteppingAction. Both mandatory and optional classes are derived from their respective abstract base classes. These classes are as follows:

- *G4VUserDetectorConstruction* creates and positions different parts of the detector or the experimental setup.
- *G4VUserPhysicsList* provides particle definitions, physics processes, and range cuts to be used throughout the simulation.

- *G4VUserPrimaryGeneratorAction* generates the primary particles and defines their momentum, direction and energy for all events.
- *G4UserRunAction* defines actions to be taken in the beginning, end, or during runs.
- *G4UserEventAction* defines actions to be taken in the beginning, end, or during events.
- *G4UserStackingAction* classifies the tracks according to their simulation priorities.
- *G4UserTrackingAction* allows the user to intervene at specific points during tracking.
- *G4UserSteppingAction* allows the user to specify actions during stepping.

3.3 TPE and GEANT4

The Two-photon exchange (TPE) experiment has taken advantage of the detailed tracking abilities of GEANT4 package to accomplish a great deal of background simulations prior to the run period. The simulation work still continues to gain a better understanding and a more complete estimate of the background for the full TPE experiment. However, this section focuses on methods and results used to prepare for the TPE test run.

The primary simulations that utilized EGS (Electron-Gamma-Shower) and GEANT3 packages, continued by converting to the GEANT4 package for more accurate physics processes down to very low energies, as well as more user friendly visualization and geometry management.

3.3.1 Simulation Specifications

The simulation project can be executed both in interative and batch modes. The interactive mode starts an OpenGL graphics window and a user gui custom-designed for our purpose. After the execution is initialized, the geometry can be inspected closely. An event can be initiated by generating an electron at a defined origin and propagating it toward a defined direction (z axis). After loading the physics libraries, the path and interactions of the track can also be visualized. It is possible to identify different secondary tracks created from the

original one, as they are color coded depending on the particle charge. A example of the interactive tracking for the TPE geometry is shown in Fig. 32.

On the other hand, the batch running mode can be used to execute jobs faster and more efficiently after finalizing the geometry. The number of events to be simulated is specified in the command line. The output of interest is programed to be stored in root tree format for better organization and cut performance. Jobs executed in batch mode are often long-running and memory-intensive. They are submitted to the Jefferson Lab batch farm [43] that consists of 175 dual CPU computer systems. The Load Sharing Facility (LSF) software package manages and schedules jobs in different priority queues.

Several optional user classes are defined in the TPE version of GEANT4 to more easily control the actions throughout the structure of every event. Various physics lists are registered. Standard electromagnetic physics processes are added for different particles individually. The physics package QGSP-BERT was chosen for hadronic processes to combine Quark gluon string model with Bertini cascade model for energies below 3 GeV [42].

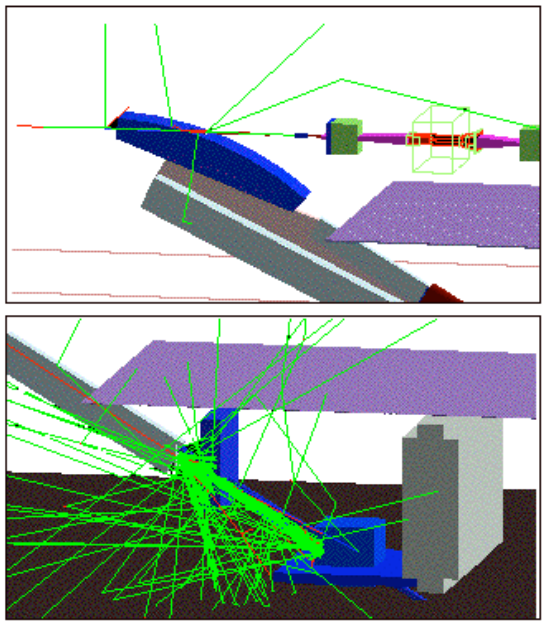

Figure 32: GEANT4 picture of particles scattering at the tagger, Top: A photon is produced by the radiator and scattered at end of the tagger magnet pipe. Bottom: An electron from the radiator is scattered at the tagger vacuum box exit window and produces photon showers.

The TPE geometry is divided into several modules each of which correspond to a different part of the setup. The main modules are Hall B, beamline, tagger, and tracking detectors such as time of flight counters and drift chambers. Hall B represents the actual space of the experimental hall filled with air. It serves as a mother volume that all the other volumes can be place in. The beamline starts at the origin and extends all the way to the target. The beamline module contains all the volumes and components placed within this range. Some important examples are, the radiator, converter, collimators, chicane magnets, beamline pipe, target components and shieldings (to be discussed later). The taggerline is positioned at a 30° angle below the beamline, and extends through the hall floor. It intersects with the beamline at the origin (downstream of the radiator). The most important feature of the taggerline is the tagger magnet that provides a uniform magnetic field and bends the electrons down through the taggerline. The tagger also includes other components such as shieldings, pipes, and the beam dump. The TOF detector was first created as a simple spherical shell made of scintillating material. It has been much further developed into a realistic multi-paddled counter since the early simulations. The six sectors of the drift chamber were also built in great detail with a distinctive wired structure. Fig. 33 shows examples of some of the above geometry more closely. It is worthwhile to note that all the positions, measurements, and materials used in this simulation project have been derived from official Hall B engineering drawings [44].

Along with the mentioned user codes, several input files have been created to control the simulation parameters more efficiently. Most of the geometry modules point to their own input files to configure their user options. Through these inputs one can flag the geometries to be built, sizes, positions and magnetic field strengths, etc. to be specified. This way, different versions of the same input file can be submitted with the same executable in batch mode, to simulate different configurations much faster. A few of the important input parameters used here are:

- Beam energy: 3.3 GeV
- Radiator thickness: 0.005 radiation length
- Converter thickness: 0.05 radiation length

- Tagger magnetic field: 2.355 T

- Pair spectrometer magnetic field: -0.3672 T

- Italian dipole magnetic field: 0.533 T

- Production cut for all processes: 1 mm (This is a range below which secondaries, with corresponding energies for a given material, are not produced.)

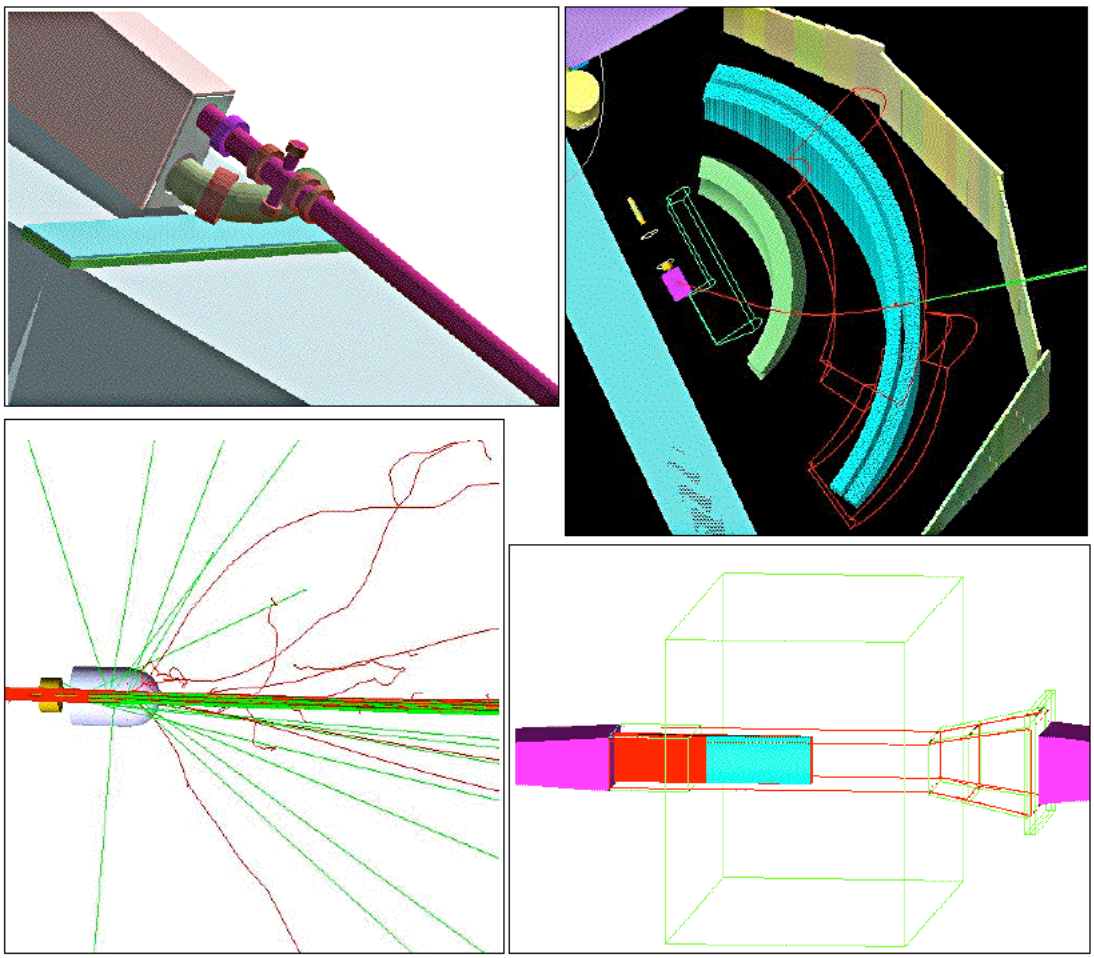

Figure 33: Simulated components of the experimental setup in detail, Top-left: Tagger module. Top-right: shows TOF paddles, DC regions 2 and 3 (region 1 exists but is not displayed here), torus magnet volume (red wired volume) and target components. The magnet (with negative current) is bending an electron track outward. Bottom-left: Target and some tracks produced in it. Bottom-right: Photon blocker embeded in the pair spectrometer magnet (green wired volume).

3.3.2 Background Identification and Remedies

The very first goal of this simulation was to reproduce the background rates and patterns observed by the earlier test runs to evaluate the functionality of the user codes under development. As mentioned in section 3.1, background rates were shown to be the highest at below-the-beam-level paddles (sectors 5 and 6) of the TOF counter and region 3 of the DC (Fig. 34(a)). A similar pattern was obseved in the preliminary simulations as shown in Fig. 34(b). These observations suggested that a major portion of the background initiates below the beamline. Therfore, the studies initially focused on the taggerline components. Fig. 35 represents the position of production vertices (points of creation) of tracks that hit the TOF detector. A large number of secondary tracks were produced around the tagger vacuum box plates, flanges and pipe, the hall floor beneath the pipe and the tagger dump (see color map). High background rates were also observed at the beamline collimator and photon blocker observed from the very preliminary simulated beamline. In each of the above cases, the background was identified and largely reduced by performing intensive and detailed simulation studies.

Taggerline

Looking more closely at the taggerline (Fig. 36), the simulations showed that after scattering off the radiator target and passing through the tagger magnet, the dumped electrons do not travel perfectly parallel to the beam pipe due to their energy spread and get scattered through the pipe and heavy obstacles around it. Some important obstacles are the vacuum box end-plate aperture and tubes, flanges, and shielding stands. Tracks back-scatter and re-scatter from the floor, or shower as they pass through various materials, creating background seen by the TOF detector.

The best solution for reducing this dominant background effect was to literally remove those components from the taggerline. Prior to this decision, many different shielding configurations were simulated and compared. The existing tagger configuration was taken to be the nominal option. It included a combination of lead and iron shielding around the

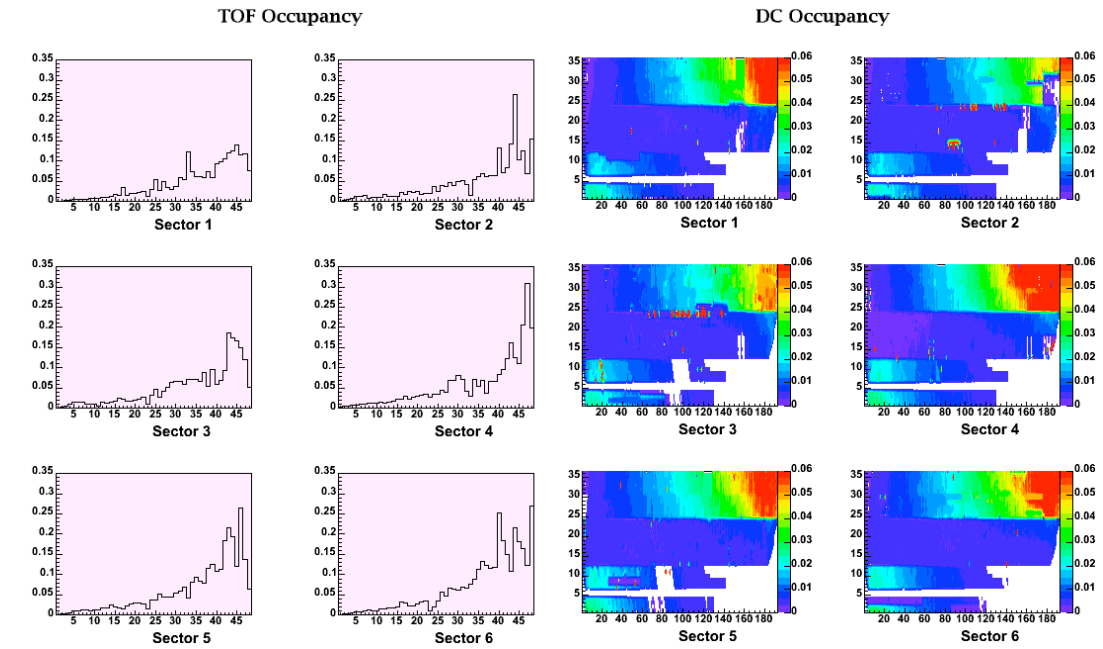

(a)

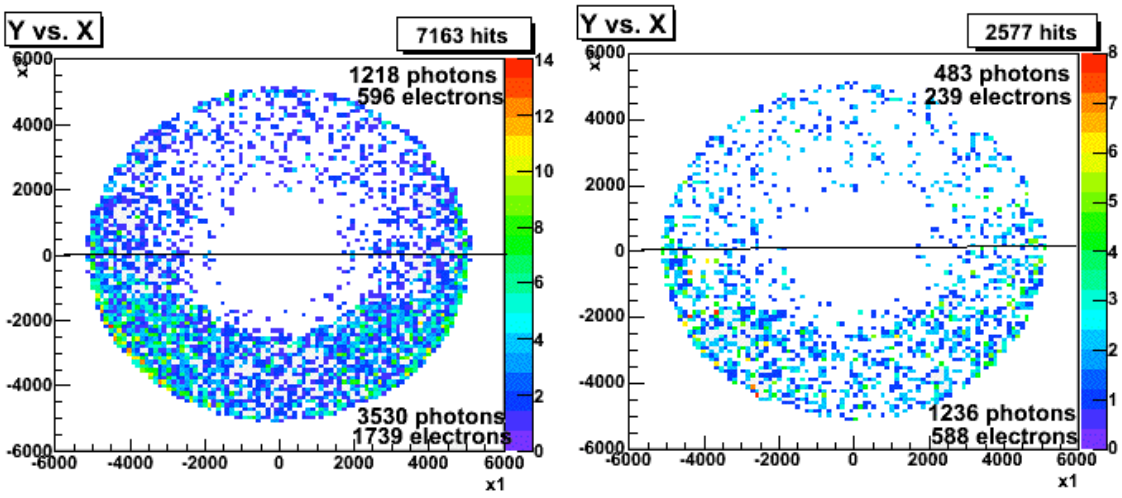

(b)

Figure 34: Experimental and simulated background occupancies, (a) For the 2004 background test run. Left: TOF occupancies for all sectors. Right: DC occupancies for all sectors. (b) Simulation results shows the same pattern of tracks hitting the detectors as for the test run. Note how the simulated background hits decrease from left to right, by removing the tagger flange.

steel beam pipe. The first option proposed was to exchange the pipe with a wider aluminum one and let the electrons travel more freely down the pipe without interacting. In addition,

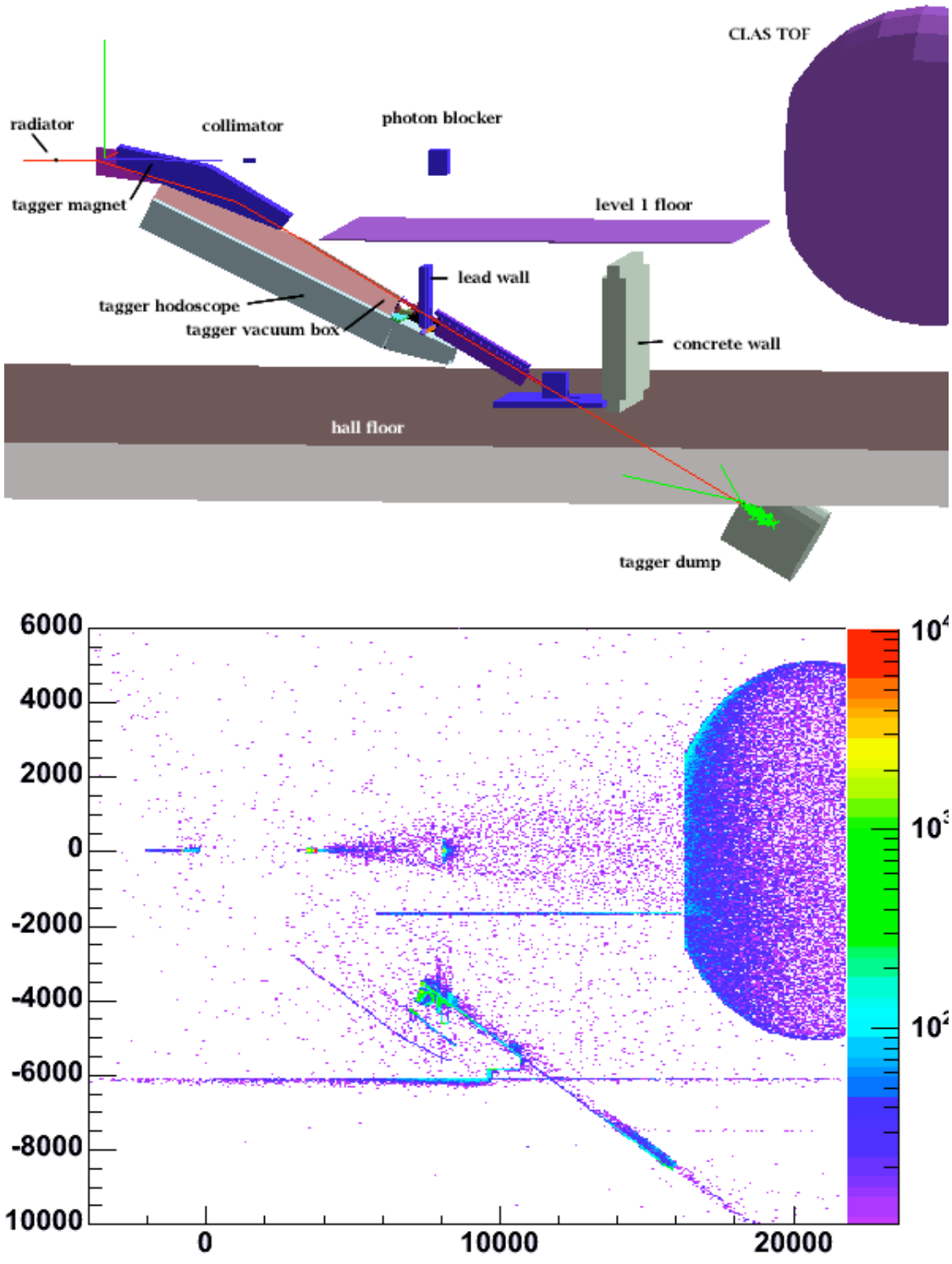

Figure 35: Simulation geometry and corresponding vertex positions, Top: TPE simulation visualized with OpenGL. Bottom: production vertex position of tracks that hit the TOF detector for the shown geometry.

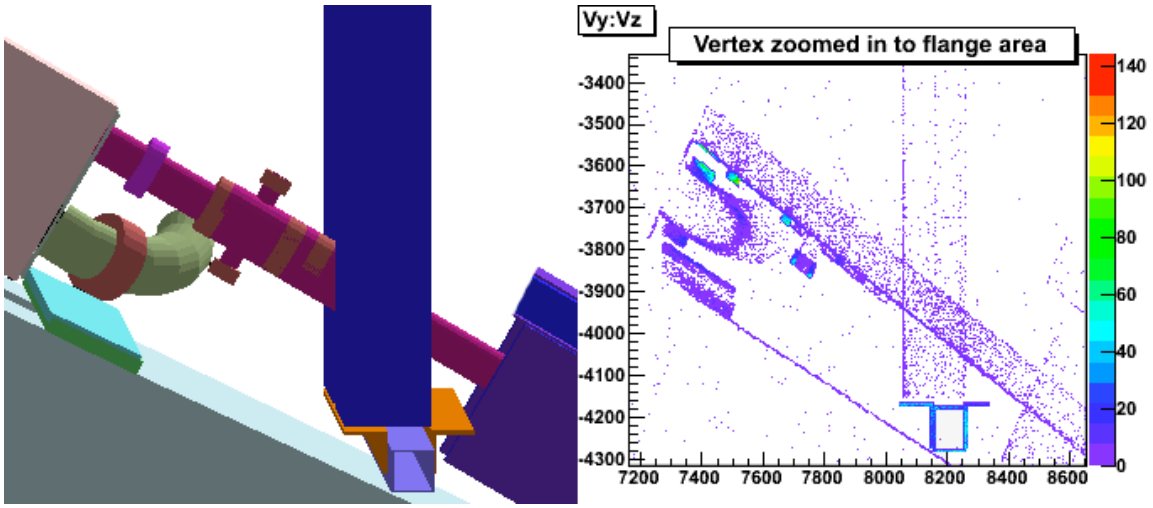

Figure 36: Zoomed view into the taggerline and corresponding vertex positions, Left: Simulation details, Right: Vertex positions of background tracks that hit the TOF detector.

the vacuum box end plate aperture was enlarged. The second option replaced the whole tagger pipe with a complex vacuum box of rectangular cross section made of steel. All the flanges were removed and the vacuum box end plate was kept the same as the first option. The third option was to replace the whole pipe with a wide helium bag. All the flanges and extra obstacles were removed and the vacuum box end plate was transformed into an aluminum frame with a thin window. The helium bag extended all the way to the tagger dump can. The third option was found to cut the background by about a factor of four compared to the nominal.

The next approach to reduce the tagger background was the use of shieldings. Many different shielding volumes of different sizes, materials and positions were designed and simulated. Mentioning them all is out of the scope of this thesis, and only the ones that were used will be discussed. Several lead blocks were placed on the floor downstream of the pipe entrance opening in the hall floor. The blocks were later replaced by a so-called lead "butterfly" shield that wrapped around that opening. Moreover, thin lead walls were positioned further downstream on the floor in horizontal and vertical orientations, and a variety of lengths and widths were tested. However, the most effective of all was a massive hut-shaped shielding placed on the floor that covered almost the entire area of concern along

the taggerline, all the way to the top edge of the vacuum box end plate. This shielding, nicknamed the "bunker", was a combination of concrete, steel, lead and kirksite. Adding the bunker to option 3 effectively decreased the tagger related background by a factor of 20 in the simulation.

At this point it was up to the engineers to bring all this to reality. Section 3.4 is dedicated to the engineering plans and hall modifications.

Beamline

To investigate the beamline related background and actually simulate the production of the secondary lepton beam, a very detailed and fully functional beamline was created. The goal was to examine the expected luminosity and secondary beam spread, to optimize the chicane magnet setting and to remove as much background as possible. Fig. 37 shows a layout of the simulated beamline.

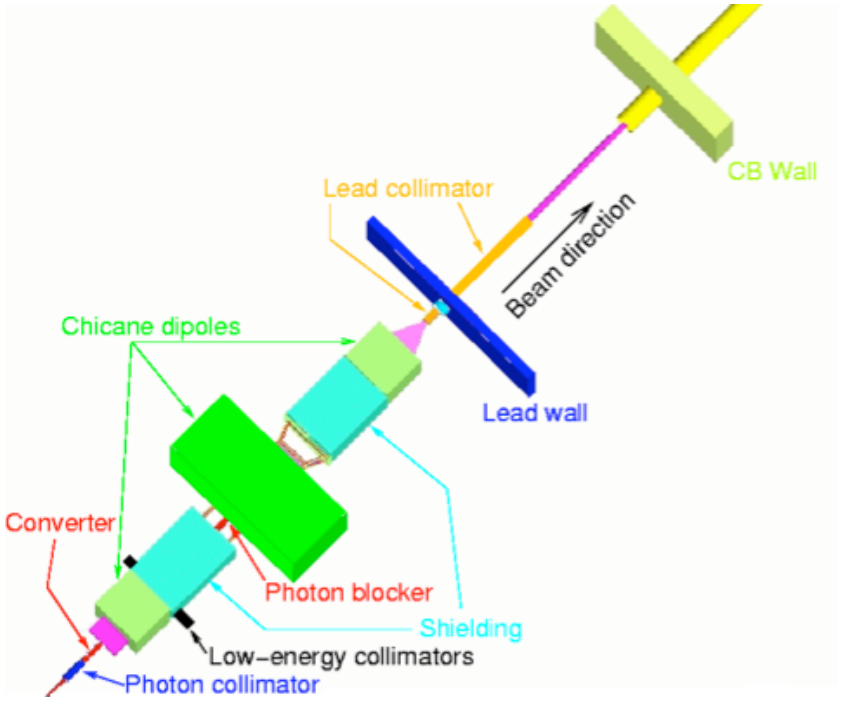

Figure 37: GEANT4 drawing of the improved beamline. The radiator is located further upstream (before the photon collimator).

Background initiated along the beamline display a more uniform distribution on the face of the TOF counter. By examining the vertex positions along the z-axis, seen in Fig.38, the photon collimator and blocker were identified to be major sources of low energy photon and neutron background respectively, whereas the low energy electron background was mainly related to the beam pipe and entrance/exit of the chicane dipole magnets. The background positron rate, however, did not seem significant enough to be of much concern. Investigations also showed that most of these particles were re-scattered and re-directed to hit the TOF counter, as their line of site was obscured by other objects.

Numerous shielding configurations were designed and simulated in order to find the ones that reduce the mentioned TOF background as much as possible. Walls and cylindrical shields were placed downstream or around the photon collimator for instance. The bare beam pipe just downstream the tagger magnet was covered. The effects of a lead/borated-polyethylene shield placed right downstream of the chicane dipoles was tested by varying it's dimensions. Some more successful designs are mentioned below and shown in Fig. 39.

- *Rad-phi wall* is a 4.5 inch thick lead wall with steel cladding, positioned shortly downstream of the second Italian dipole. It cuts the overall background by almost 14%.

- *Beamline tunnels* are made of borated-polyethylene and surround the helium bags that connect the pair spectrometer to each of the Italian dipoles. They contribute in reducing the low energy photon and neutron background by around 15%.

- *Rad-phi collimator* is a lead cylinder that fits into the aperture of the rad-phi wall. Successive studies were done to optimize the diameter and length of this collimator by comparing their signal to background ratios in each case. Reduction levels up to 35% were reached using the best configuration of this collimator. It is worth mentioning that a further modified version of this component played a key role in reducing the background during the TPE test run.

Background occupancies in regions 1 and 3 of the drift chambers were also investigated. As can be seen in the top Fig. 38 plot, the projection of the production vertex positions onto the beamline direction (z-axis), region 1 of drift chambers was mostly affected by

background from the target components. These are target walls, cooler, condenser and some more downstream devices such as scattering chamber, exit window and air. Background particles are mainly low energy Møller/Bhabha electrons.

Two important shielding additions designed to stop these electrons are the following.

- *Bullet shield* is a lead bullet-shaped device placed downstream of the target. It mainly helped to cut down the amount of very low energy electrons.

- *Møller shield* is a plastic tube that surrounds the target scattering chamber. As indicated by it's name, this shielding significantly reduced the low energy Møller/Bhabha electrons produced in the target area. When combined with the lead bullet discussed above, it proved to be extremely effective.

Region 3 of DC was found to be occupied by low energy photons, that were partially eliminated by the shieldings already mentioned for TOF studies (Fig. 38). More shielding was installed during the test run and will be discussed in section 3.4.

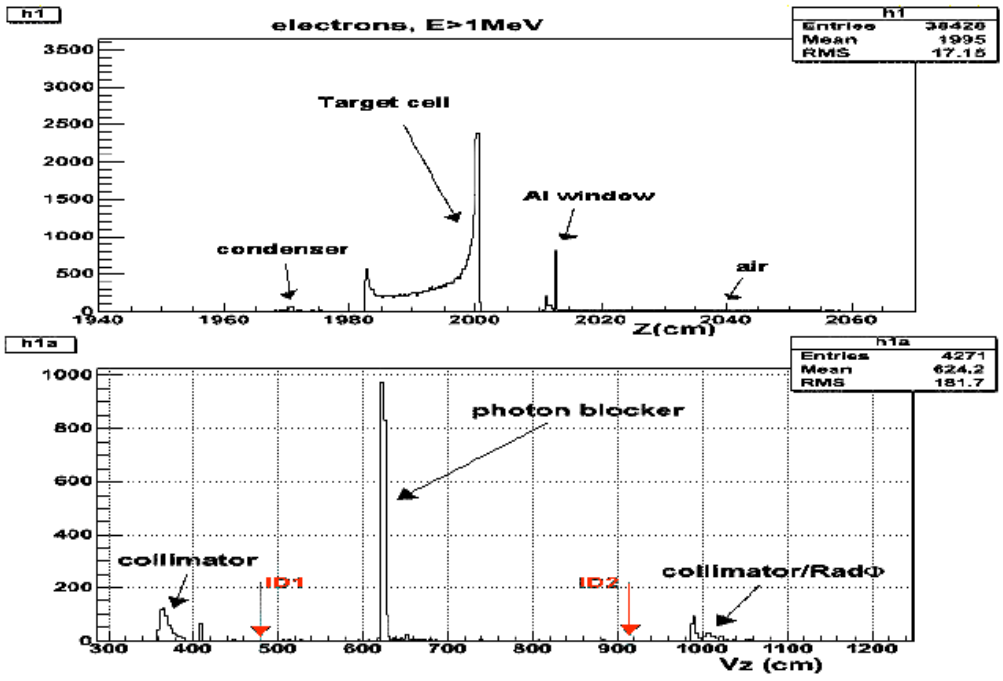

Figure 38: Projection of background track vertices, Top: for electrons that occupy region 1 DC, Bottom: for all particles that occupy region 3 of DC.

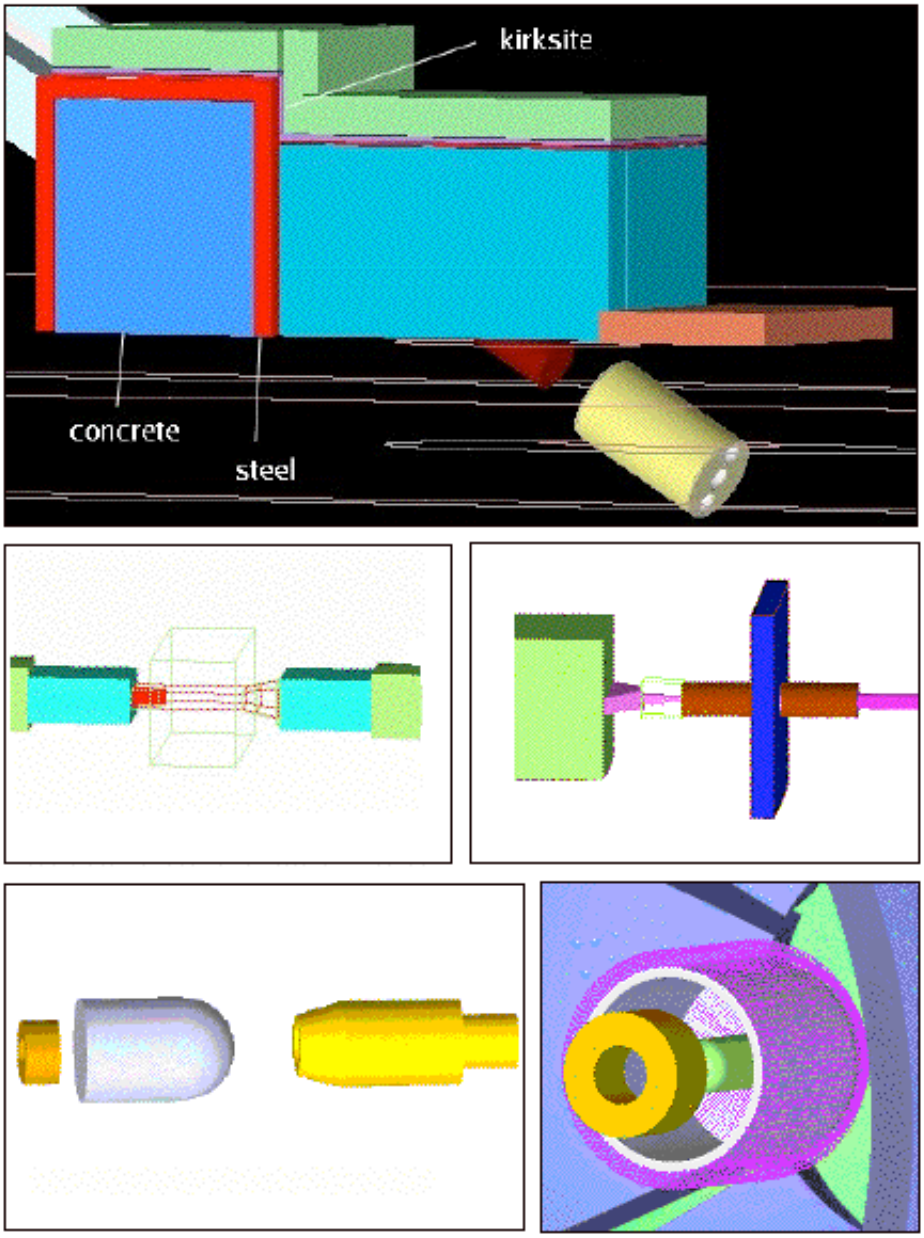

Figure 39: Simulation images of different shieldings, Top: Tagger bunker shield (hall floor is transparent here), Mid-left: chicane tunnels (blue) and Italian dipoles (green), Mid-right: rad-phi wall (blue) and rad-phi collimator (brown), Bottom-left: from left to right (beam direction) are condenser, scattering camber surrounding the target and bullet shield, Bottom-right: Møller shield (pink wireframe) around the scattering chamber.

Throughout the test run, the relative beam luminosity, which is a product of radiator thickness, converter thickness and beam current, was carefully monitored. The desired

shielding configurations were the ones that allowed for the luminosity to be maximized without letting the detectors be overwhelmed by background. This subject will be discussed in more detail in the next chapter.

3.3.3 Secondary Lepton Beam Studies

In addition to background studies, GEANT4 has been utilized to configure and optimize the chicane functionality and the secondary lepton beam production and tuning. Fig. 40 visualizes the simulated chicane dipoles and the idealized lepton paths within these magnets.

The main purpose of this part of the simulation was to minimize the beam spot size on the target, while eliminating as little high energy leptons as possible. The preliminary simulations concluded that the increase in the spot size compared to a primary beam is, in part, due to the beam divergence at the converter. A careful choice of converter thickness with proper collimation was required to improve this condition.

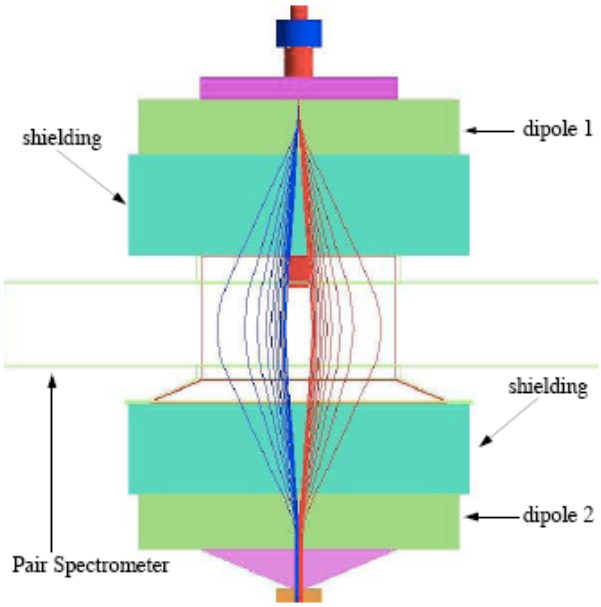

Figure 40: The TPE chicane magnet, which includes 2 italian dipoles (green) and a pair spectrometer dipole (green wired) with a photon blocker within it (red). Beam travels from top to bottom.

The effect of different radiator, collimator and converter thicknesses on the lepton beam spread was investigated in detail. After choosing the best combination that led to the smallest spot size with the highest signal to background ratio, it was time to think of additional solutions. Several extra collimators that were tested for this purpose are:

- *A downstream collimator* that consisted of an inner and an outer lead cylinder (the inner being slightly longer) placed downstream of the beamline helium bag and upstream of the target cooler. The simulations showed that in addition to reducing the detector background, it is an effective device in shrinking the beam spot size.

- *A cleanup collimator* that was a 12 inch long square hollow lead block placed right after the rad-phi wall. This collimator that was added during the test run and simulated later, effectively removed the low energy lepton band on the face of the target. It also assisted in cutting out some region 1 background that initiated downstream of the target cooler.

Fig. 41 shows the horizontal projection of the simulated lepton beam profile versus beam energy on the target. It shows how the downstream collimator reduces the beam spot size.

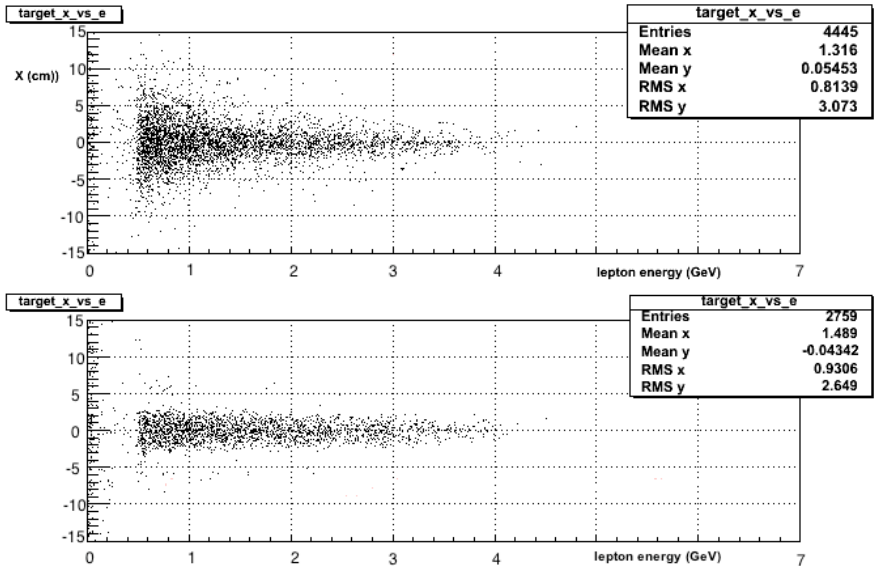

Figure 41: Simulation results of the horizontal beam profile on the target vs. beam energy, Top: without, and Bottom: with a downstream collimator. Beam energy is 5 GeV here.

3.4 Experimental Setup Modifications

Prior to TPE test run, the Hall B engineering staff helped convert the simulated shielding and beamline geometry into reality. They built, installed and modified several pieces of equipment that had been fully simulated. Most of these modifications were already discussed in the previous section, such as reshaping the taggerline by widening the tiny apertures, removing the pipe and excess devices and replacing them with a helium bag, building a bunker shield around this bag, designing a rad-phi wall and collimator, building chicane tunnels and target area shieldings, and adding several extra collimators to the beamline.

Figure 42: Photographs taken during engineering work, Top-left: from right to left are second chicane tunnel, second Italian dipole, rad-phi collimator, rad-phi wall and helium bag. Top-right: cleanup collimator downstream of rad-phi wall, Mid-left: tagger flanges and vacuum pipe, Mid-right: tagger vacuum box window and helium bag, Bottom-left: tagger bunker shield, Bottom-right: tagger dump can. Photos are provided by [45].

A number of extra shielding elements were stacked in the hall during the experiment run time and proved helpful as well. They are mentioned here in order of installation: A 12-inch thick concrete block wall was placed on the CLAS cryo-ring that reduced the relative EC sector 5 and 6 background rates by a factor of 2 and DC sector 5 and 6 occupancies by about 30%. Lead blocks were added to the chicane magnets and tunnels to seal the gaps. Additional shielding was placed on the floor around the tagger dump area. A large 12-inch thick concrete wall was installed on the CLAS insertion cart that cut the large angle background down substantially, allowing an increase in the beam current and a higher luminosity. Some photographs taken during the installation period are presented in Fig. 42.

3.5 Conclusion

The simulation work was a success. The secondary electron/positron beam was created exactly as expected. The increased target radius was proven to be necessary, as the beam spot size was wider than usual. All the rates and occupancies monitored during the experiment agreed with the simulation results and predictions. They were reduced significantly compared to the previous short test runs. The issue of high background due to producing a secondary beam plus dumping the electron beam, that threatened the feasibility of the TPE experiment is now under control. Ongoing simulations aim to further improve the experimental conditions and prepare for the full experiment in a few years.

4 Data Processing and Analysis

The two-photon exchange (TPE) test run collected data for almost three weeks, from October 3rd through 23rd of 2006. A 20-cm long, 6-cm diameter liquid hydrogen target (LH2) was used, with a 3.3 GeV polarized electron beam incident on the tagger radiator. The beam polarization was a requirement for adjacent experimental halls and did not have an effect on this experiment. The beam current was varied from 20 to 150 nA with an average of about 60 nA. The luminosity achieved was about 5.2×10^{31} cm^{-2}s^{-1}. The CLAS toroidal magnet had a current of 1500 A for all the "production" runs, and its polarity was reversed 4 times to minimize the systematic uncertainties. The data rate was fluctuating from 300 to 3500 Hz, depending on the run configuration. Table 1 summarizes the run conditions.

There was a total of 116 production runs during this experiment. About 30% of these runs, however, were not considered useful due to their high background contamination. This background was greatly reduced during the first week of the run period by placing an extra collimator (rad-phi collimator) downstream of the chicane magnet. Each run contained between 5 to 63 files depending on the number of triggers and run length. All the files within a run were of uniform characteristics as the settings were modified in between runs.

The data files collected during the TPE run period, like any other experiment, were in "raw" format. This means the information from time to digital converter (TDC) and analog to digital converter (ADC) outputs of different detectors were directly recorded and saved onto tapes (mass storage system). The data on these files needed to be calibrated and then processed in order to reconstruct the particle tracks, momenta and energy. The reconstruction process is called "cooking" and is usually done by one "chef" for consistency, whereas the calibration is done by a different person for each detector.

Primary beam energy/average current	3.3 GeV/ 60 nA
Secondary beam energy/average current	$0.5 - 3.3$ GeV/20 pA
Luminosity	5.2×10^{31} cm^{-2}s^{-1}
Target	6 cm D, 20 cm L, LH_2

Table 1: TPE test run conditions.

To correct for the detector timing offsets that affect the track reconstruction, the CLAS time of flight (TOF) and drift chamber (DC) systems were individually calibrated. These calibrations are briefly mentioned in the next section followed by a detailed description of the drift chamber DC calibration performed by this author.

4.1 Data Cooking

The TPE data were cooked using the CLAS REConstruction and analySIS package (RECSIS). During this procedure the raw detector information was converted to physical quantities such as momenta, times and vertex positions. A preliminary cooking took place after each calibration iteration. After the calibration was completed, the information on reconstructed hits by the detector modules was passed to the Simple Event Builder (SEB) for final event reconstruction. The SEB package is designed to find the geometrically matched tracks and hits, get the trigger particle and trigger time, identify particles, build the events and write the output in "BOS" [1] format [47]. The cooking process is as follows:

- **Geometric hit/track matching**

  This process mainly refers to finding the relative distance between the detector hit and position on the detector plane generated by a master track. The master track for charged particles is defined by matching the DC track with a hit in the CC or EC, whereas for neutral particles (no DC tracks), the track is defined by a straight line drawn from the origin to the EC hit position. For each hit, the best match for the track is identified as the one that minimizes C_i [48].

$$C_i^2 = \sum_{i=x}^{z} \frac{(r_{pl} - r_i)^2}{\sigma_{r_i}^2} \tag{28}$$

  where r_i is the detector hit position, r_{pl} is the master track hit position on the detector plane, σ_{r_i} is the uncertainty of r_i, and i is the axis indicator ($i = x, y$ or z).

[1] BOS is a format used for dynamic data management, written in standard FORTRAN77. It consists of a modular structure called banks that contain a set of data that belong together. Some examples are HEAD, EVNT, PART, VERT, SCPB and etc. Banks with the same name have the same data format. BOS is also useful for input/output of sets of data. For detailed description of BOS data format please see [46].

- **Trigger identification and timing**

  As discussed in Chapter 2, the triggering criteria was modified for this experiment, as the usual single electron trigger would miss the large angle events and as a result would limit the ϵ coverage. Therefore, the TPE trigger particles were two charged particles that hit the TOF in opposite sectors. As soon as this requirement was met, the event was recorded.

  After the trigger particles were identified, the trigger time (time that trigger particles left the target) was determined for each event by using:

$$t_{trk} = t_{det} - \frac{R_{det}}{\beta c} \tag{29}$$

  where t_{det} is the time measured by the TOF, R_{det} is the path length of the trigger particle from the target to the detector determined by the tracking reconstruction algorithm, and β is the particle velocity [48].

- **Particle identification**

  In the next step, the particle identification (PID) was determined for each particle within a certain event by using the detector time and track momentum. The detector timing information was obtained from the TOF for charged particles and from the EC for neutral particles. Neutral particles with velocities within 5% of β=1 were identified as photons and all other neutrals were identified as neutrons.

- **Event building**

  The information for all identified particles were combined into event blocks, starting with the trigger particles followed by a predefined order of particle types.

- **Output**

  In the final step, all the information acquired for all groups of geometrically matched hits and tracks was loaded into BOS banks along with their detector hit values to be used for further data analysis.

4.2 Detector Calibration

The time-of-flight and drift chamber systems were calibrated prior to analysis of the TPE test run. The TOF calibration is performed in a specified sequence starting with pedestal and TDC calibration and ending with RF offset calibration, performed in the correct order. A detailed explanation of the TOF calibration procedure is given in [49]. The electromagnetic calorimeters are usually calibrated as well. However, TPE used the EC constants optimized by the previous experiment, because the data from this detector was not used in this analysis. The DC calibration followed the TOF and is discussed in detail.

4.2.1 Drift Chamber Calibration

As explained in the second chapter of this document, the CLAS drift chambers consist of three regions positioned at different radial distances from the target. Each of the DC regions are divided into two radial superlayers (each consists of 4-6 layers of sense wires) and six azimuthal sectors. Each superlayer of every sector was calibrated separately to improve the track reconstruction efficiency. As a result, there were 36 sets of 24 parameters that needed to be optimized.

As a track passes through the 34 drift chamber layers of a sector, several hits are registered. A track can be reconstructed by performing a least squares fit using the mentioned hit positions inside the CLAS reconstruction program. At this point it is worth introducing some frequently used terminology:

- FITDOCA: The distance of closest approach between the fitted track and the sense wire.
- CALCDOCA: The distance of the track to the sense wire calculated using the drift time information.
- RESI: The residual is the primary means to determine the drift chamber resolution, whose sign is determined by any systematic time shift:

$$RESI = |FITDOCA| - |CALCDOCA| \tag{30}$$

The reconstruction of the charged particle tracks is done in two stages. The first stage is called "hit-based" tracking where the individual DC wire hits are fit to form a track segment in each superlayer. Then the segments are combined to reconstuct the full track across the three regions. The tracking can be further refined during the second stage of track reconstruction, which is called the "time-based" tracking. In this stage the timing information from the TOF counter is used to correct the measured drift times. These corrected drift times are then converted into drift distances (CALCDOCA) using the calibrated drift velocity parameters. The drift time is calculated as follows:

$$t_{drift} = t_0 - t_{start} - t_{TDC} - t_{flight} - t_{prop} - t_{walk} \tag{31}$$

where t_0 is the time delay caused by cables and electronics, t_{start} is the event start time, t_{TDC} is the raw drift chamber TDC time measurement, t_{flight} is the flight time of the particle from the vertex to the struck DC layer, t_{prop} is the signal propagation time along the DC wire, and t_{walk} is the time walk correction [50].

The DC calibration is performed in several iterations. During each iteration the CALCDOCA is calculated from the drift time by using a parameterized drift velocity function, depending on the values of track entrance or local angles (angle between the track and the side of the drift chamber hexagonal cell) and the magnetic field settings. These calculated distances are then fit to give rise to the FITDOCA, which is plotted versus the drift time and fit with a pre-determined drift velocity function. The first iteration uses some initial drift velocity (x vs. t) parameters usually copied into the run-indexed calibration database (CalDB) [2] from the previous experiment, that are then refined during several calibration iterations. Each iteration uses the parameters from the previous one to convert the drift time into drift distance. The parameters can be further improved by fitting the residual distributions (RESI) plotted versus the drift times. This procedure is usually performed after the drift velocity fit parameters stop converging.

[2]The so-called run index table is an SQL-based system divided into sections called "*systems*", each of which are grouped into "*subsystems*" and even further into "*items*". All the parameters necessary for detector calibration are stored in this table that is uniquely created for every experiment. For more information about the calibration database and the DC calibration parameters see [50].

The drift velocity function chosen for a given track entrance angle depends on what region the track is traversing. A power law function works best for region 3 tracks and has the form:

$$x(t) = v_0 t + \eta \left(\frac{t}{t_{max}}\right)^p + \kappa \left(\frac{t}{t_{max}}\right)^q \tag{32}$$

where v_0 is the velocity at $t = 0$, coefficients η and κ, and the exponents p and q are the fit parameters. Moreover, t_{max} is the drift time of tracks that are close to the edge of the drift chamber cells, and for which the path that the ions take to reach the sense wires are independent of the track entrance angles.

The drift velocity function for regions 1 and 2 has a 5th order polynomial form:

$$x(\hat{t}) = a\hat{t} + b\hat{t}^2 + c\hat{t}^3 + d\hat{t}^4 + (cc - a - b - c - d)\hat{t}^5 \tag{33}$$

where $\hat{t} = t/t_{max}$ is the normalized drift time, and a, b, c and d and cc are the fit parameters with $cc = Ccos(30° - \alpha)$ is the maximum drift distance at $t = t_{max}$, and α is the track entrance angle. cc can also be interpreted as the cell boundary constraint, $x(\hat{t} = 1, \alpha) = cc$, where C represents the cell size.

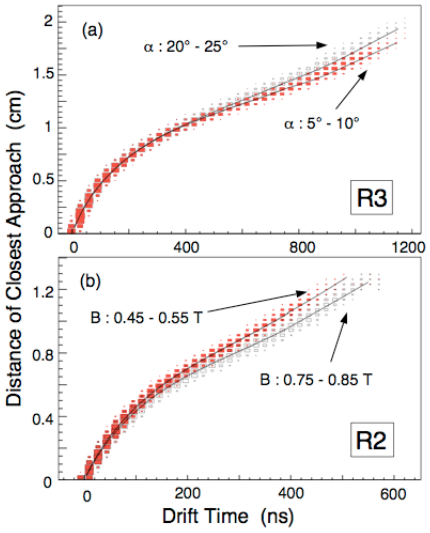

Figure 43: FITDOCA vs. drift time, (a) region 3 showing the entrance angle dependance, and (b) region 2 showing the magnetic field dependence for entrance angles between 23°-25°. The overlaid curves show the fitted time-to-distance function.

Magnetic-field-dependent corrections to the entrance angle (α_c) and the maximum drift time $t_{max}(B)$ are also necessary for region 2, as this region is located in between the toroidal magnet cryostats. As a result, the drift paths are rotated and cause a shift in the above variables. Fig. 43 shows the general shape of the distance versus time distribution for regions 2 and 3. For a more detailed description of how the DC calibration is formulated please refer to [50].

The calibration procedure was performed taking advantage of *trk_mon* and *dc3* software packages, that encapsulated the above procedure; *trk_mon* accepts user specified entrance angle and beta range cuts to produce Ntuples required by *dc3*. The actual calibration was handled by *dc3* where the fitting was done and the resulting parameters were written to the run index table. This process was performed in several iterations, on positive and negative torus polarity data separately.

4.2.2 Monitoring Histograms

The quality of the DC calibration was checked by plotting the weighted mean (centroid) and sigma (standard deviation) of the double-Gaussian fits to the residual distributions, against run number. These plots are called monitoring histograms. This was done after the finalized calibration constants were written to the database for the entire run period. Any erratic behavior of these parameters over time was expected to be minimized through successive calibrations.

Due to smaller statistics of each data file in the TPE test run, multiple Ntuples were combined and the residual histograms were fit manually with double-Gaussian functions, for every sector and superlayer of every run. The finalized monitoring histograms are shown in Fig. 44 for all sectors combined. Different marker colors correspond to parameters for different superlayers as specified. It can be concluded that the drift chambers were well calibrated, as the residuals were consistently minimized for all the runs.

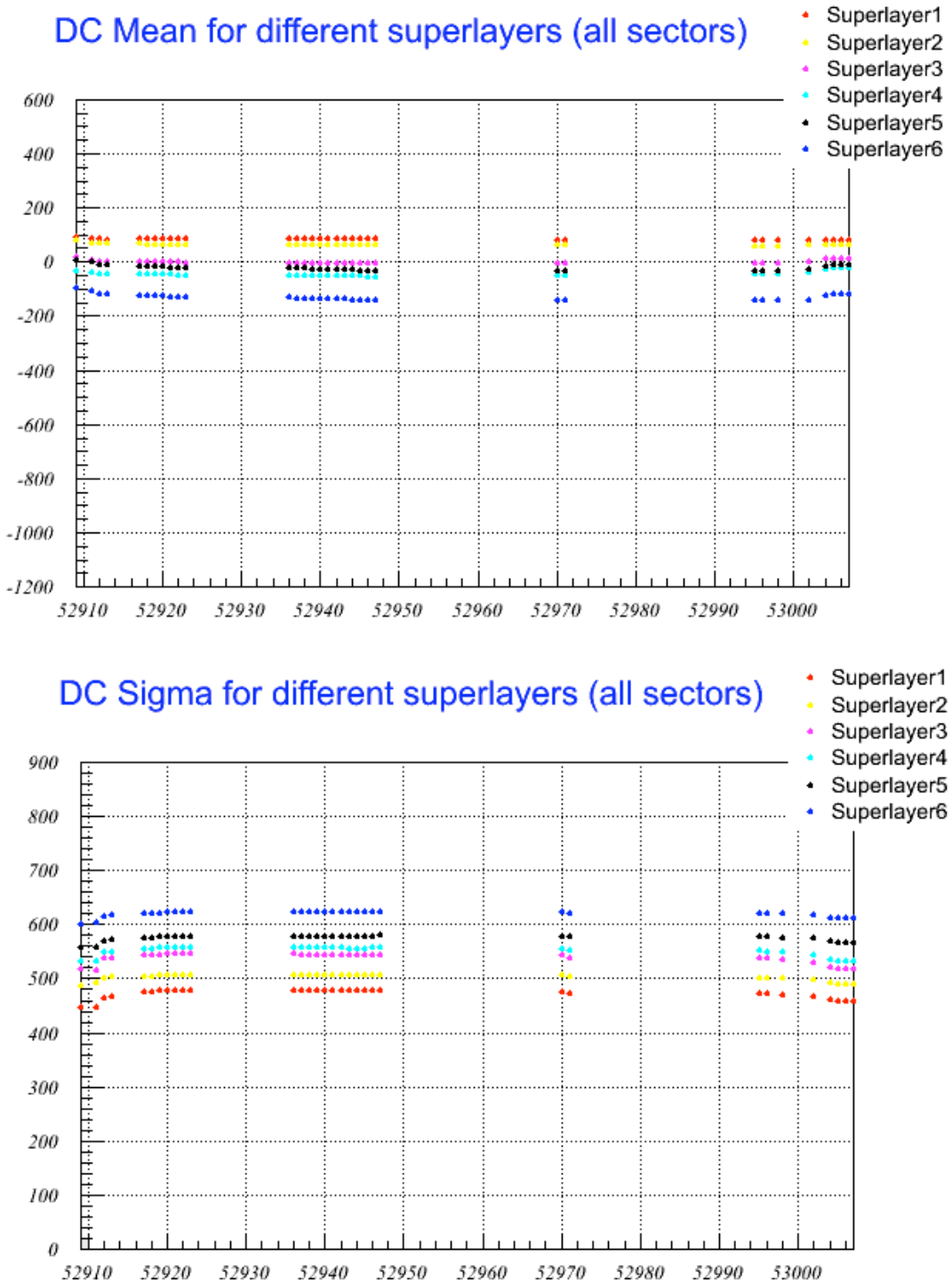

Figure 44: Residual weighted means and sigmas for all sectors and superlayers. Top: mean, Bottom: sigma distributions as a function of run number (positive polarity runs).

4.3 Data Analysis

4.3.1 Elastic Event Identification

The elastic $e^{\pm}p \rightarrow e^{\pm}p$ events of interest were mixed with a large amount of background associated with a wide range of interactions initiated at the target or the detector/beamline components. The large data volume is mainly due to the large acceptance of the CLAS detector, and requires a detailed and thorough event selecting analysis.

The elastic events were identified by introducing different types of "cuts" that serve as filters to gradually remove the events with unlikely kinematic or geometrical specifications. Requiring an event to be elastic automatically reduced the effects of track misidentification. Moreover, no CC or EC restrictions were applied in this analysis, as their angular coverage was limited to smaller angles, which in turn, would limit the kinematics of this study. In addition, the CC can introduce an asymmetry in electron versus positron selection and increase the final systematic uncertainty.

4.3.1.1 Elastic (kinematic) Cuts

The very first step in event identification was to isolate the events with only two particles in the final state. A cut was also placed on the charge of these final state tracks, and only events with positive/negative or positive/positive charge combination were chosen.

The additional cuts included range limitations applied to six individual kinematic variables that correspond to the elastic scattering interaction. As explained below, these cuts were correlated and contribute to finding the cleanest elastic event distributions with minimal background contamination. The final events extracted after all the kinematic cuts, were found to be about 25% of the total data.

- *Z-vertex Cut*

  The interaction vertex along the z-axis (beam direction), was required to be within the range of the target length. A z-vertex cut was placed at $V_z > -10$ cm as the upper limit of $V_z < 10$ cm was already cut out in cooking. Plots (a) and (b) in Fig. 45

and Fig. 47 show the V_z distribution over the entire azimuthal angle range, without and with all cuts except its own, respectively.

- *Azimuthal Opening Angle Cut*

  The azimuthal angle difference between the products of an elastic scattering interaction was observed to be sharply peaked around 180° as expected. A 3σ cut, which was estimated by fitting it with a Gaussian function, was applied to the mean of this peak. This cut ranged $176.57° < \Delta\phi < 183.63°$, to ensure back-to-back scattering. Plots (c) and (d) in Fig. 45 and Fig. 47 show the $\Delta\phi$ distribution without and with all cuts except its own.

- *Transverse Momentum Cut*

  Because the beam travels along the z-axis, conservation of momentum requires the total transverse momentum of the final elastic scattering products to be zero. Therefore, a transverse momentum cut was applied to pick the elastic events. This cut was found by fitting a Gaussian function to the transverse momentum that was peaked close to zero, and was $-0.057 < p_t < 0.083$ GeV. Plots (e) and (f) in Fig. 45 and Fig. 47 present this distribution without and with all cuts except its own, respectively.

- *Beam Energy Difference Cut*

  Due to the over constrained kinematics [3] of this experiment, the secondary beam energy could be determined in two different ways. Equation 34 finds the beam energy using the scattered lepton and proton angles, whereas equation 35 calculates this value from the total momentum along the z direction.

$$E_{beam} = m_p \left(cot\frac{\theta_{e^\pm}}{2} cot\theta_p - 1 \right) \quad (34)$$

$$E_{beam} = p_{e^\pm} cos\theta_{e^\pm} + p_p cos\theta_p \quad (35)$$

[3] Because we measured the energies and 3-momenta for all particles in the final state, our kinematics are over constrained. This allows us to reconstruct the unknown energy of the incident particle.

These two quantities should be the same for an elastic scattering interaction, so taking the difference should give $\Delta E_{beam} = 0$. The range is derived from the σ of a fit to the peak clearly formed at near zero, that is $-0.138 < \Delta E_{beam} < 0.162$ GeV. The ΔE_{beam} distribution is shown in plots (a) and (b) of Fig. 46 and Fig. 48 without and with all cuts.

- *Beam Polar Angle Cut*

  The secondary e^-/e^+ mixed beam was required to travel along the z axis. Any large deviations may have been due to multiple-scattered background leptons misidentified as beam particles. To discard these background events, a beam polar angle cut of $\theta_{beam} < 5^\circ$ was applied. This cut removed the events where the incident particle has a polar angle larger than 5 degrees. The cut is presented in plots (c) and (d) of Fig. 46 and Fig. 48.

- *Distance of Closest Approach Cut*

  The distance of closest approach in this context is defined is the distance that two tracks come closest to one another. These tracks are the elastically scattered lepton and proton. The shortest distance is found using an algorithm that draws a line perpendicular to both tracks and calculates the length of this line by utilizing basic vector algebra. This cut was required to span a range of $-3.6 < DoCA < 4$ cm, and was obtained in a similar fashion to other cuts mentioned previously. It has a relatively large impact on the data selection, shown in plots (e)/(f) of Figs. 46 and 48.

4.3.1.3 Fiducial Cut

The fiducial cut is a purely geometrical cut that was used to not only trim off the events on the detector edges where the detection efficiency changes rapidly in each sector, but to isolate the regions of the solid angle where the electron and positron distributions overlap. In other words, the two flavors of leptons were forced to have similar acceptance to some extent, to insure the reduction of systematic uncertainties. The functional form of this cut

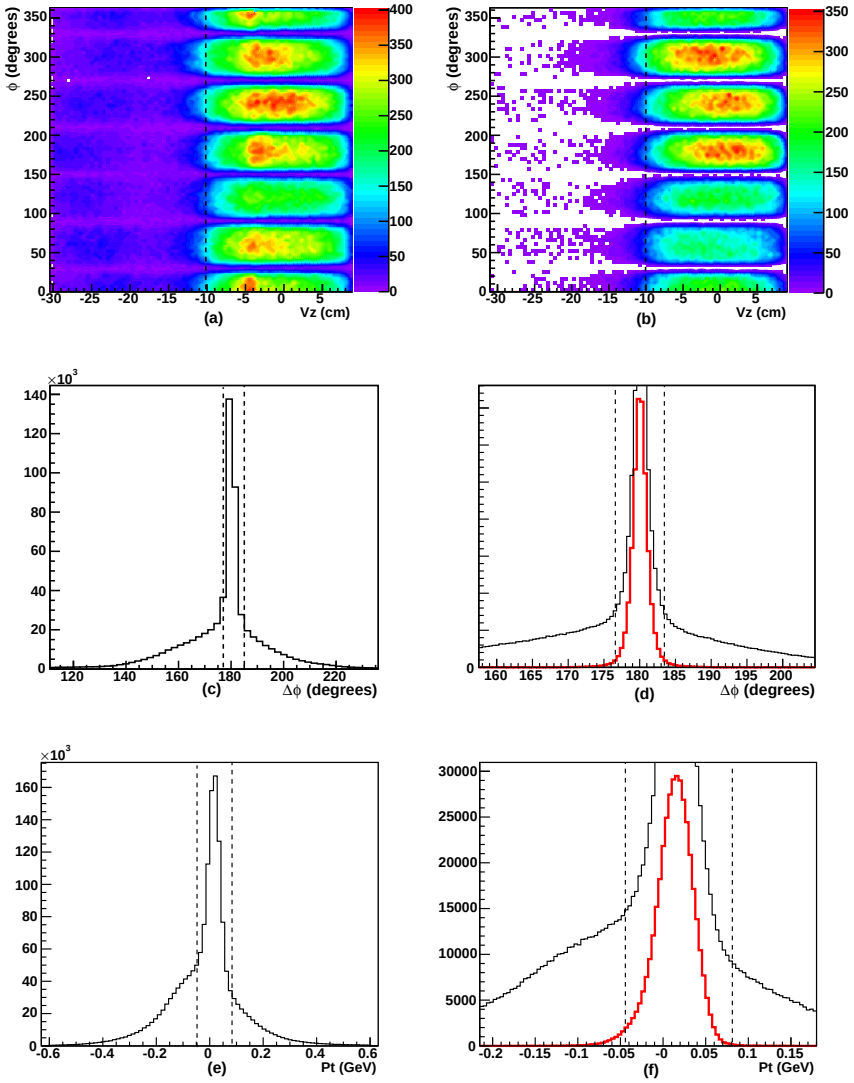

Figure 45: Kinematic cuts (1) for electron-proton events. Event vertex (a)/(b), azimuthal angle difference (c)/(d) and transverse momentum distributions (e)/(f), before/after all the cuts (except their own) respectively, for both polarities.

can be described as the region enclosed between a circle and an ellipse in each sector, where θ and ϕ are polar and azimuthal angles of the elastic scattered leptons.

$$(\theta - 39)^2 + \phi^2 \quad < \quad 625 \tag{36}$$

$$\frac{(\theta - 52)^2}{169} + \frac{\phi^2}{1600} \quad > \quad 1 \tag{37}$$

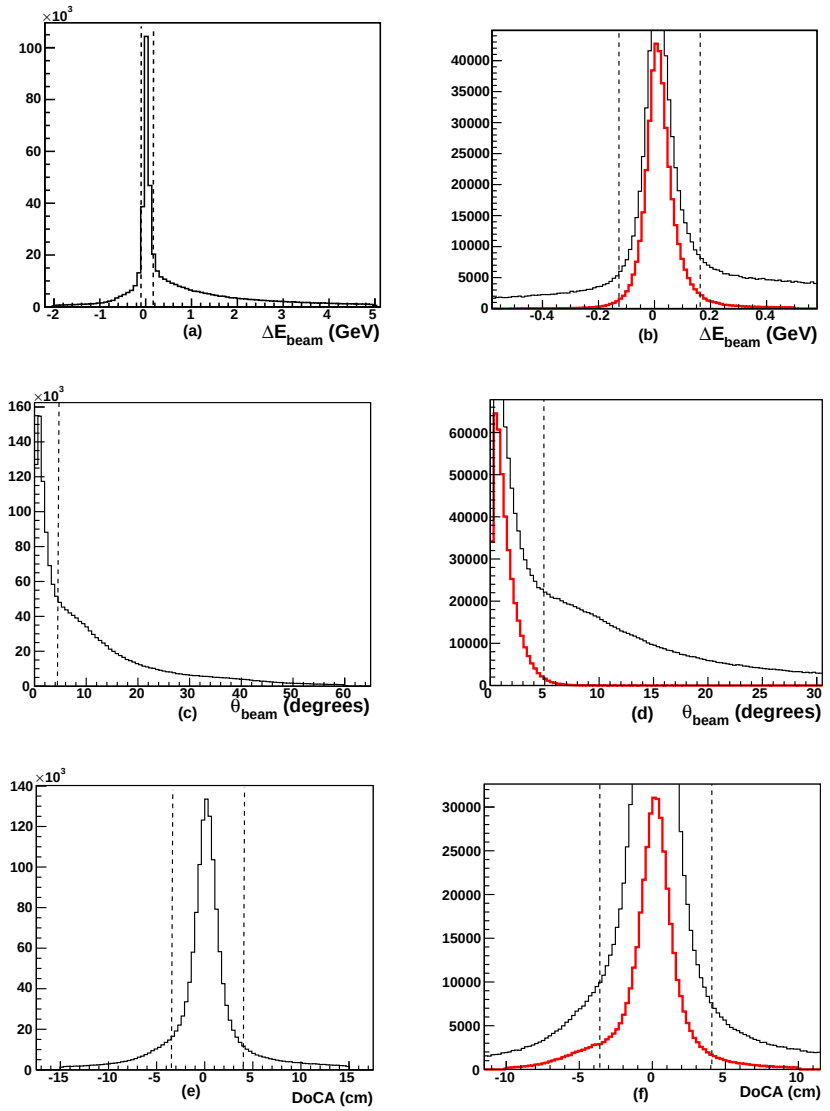

Figure 46: Kinematic cuts (2) for electron-proton events. Beam energy difference (a)/(b), beam polar angle (c)/(d) and distance of closest approach distributions (e)/(f), before/after all the cuts (except their own) respectively, for both polarities.

Fig. 49 shows the coverage of the fiducial cut for each individual sector. The same cut was found to be appropriate for all sectors as the angular distributions were very similar.

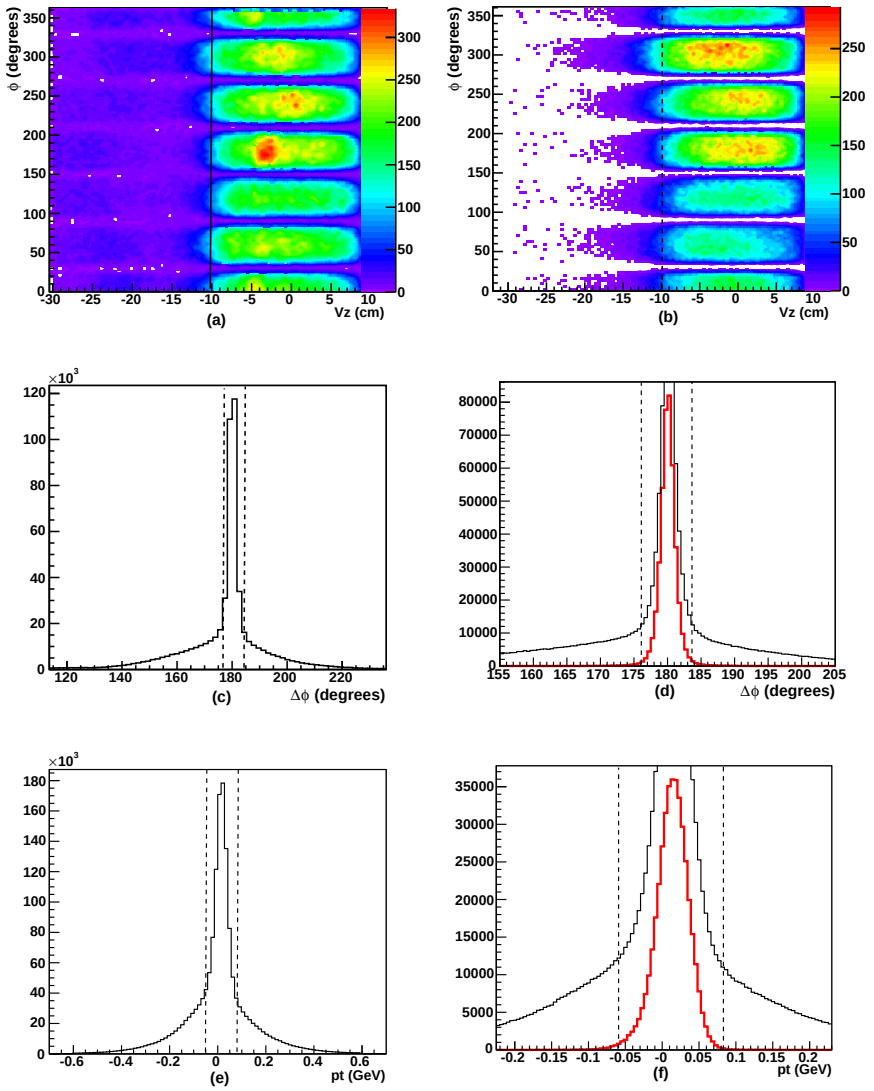

Figure 47: Kinematic cuts (1) for positron-proton events. Event vertex (a)/(b), azimuthal angle difference (c)/(d) and transverse momentum distributions (e)/(f), before/after all the cuts (except their own) respectively, for both polarities.

4.3.2 Elastic Kinematics

The elastic (kinematic) and fiducial cuts when combined, neatly isolated the events corresponding to elastic lepton-proton scattering with no substantial background. This was very encouraging since further background reduction methods could potentially jeopardize the statistical significance of this analysis.

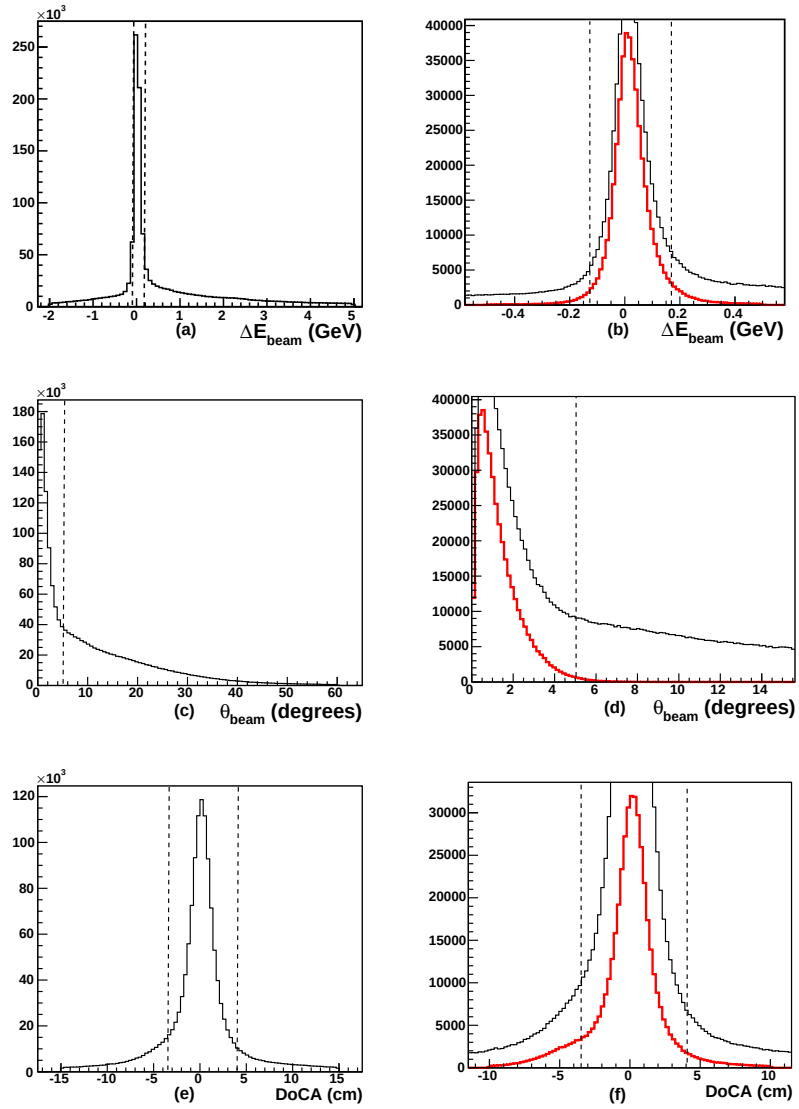

Figure 48: Kinematic cuts (2) for positron-proton events. Beam energy difference (a)/(b), beam polar angle (c)/(d) and distance of closest approach distributions (e)/(f), before/after all the cuts (except their own) respectively, for both polarities.

In order to insure that the remaining events identified as elastic are truly of elastic nature, several other kinematical variables were examined. The invariant mass W in this analysis was defined as the mass of the particle that satisfies energy conservation, reconstructed from the detected lepton, the known target and the reconstructed beam energy

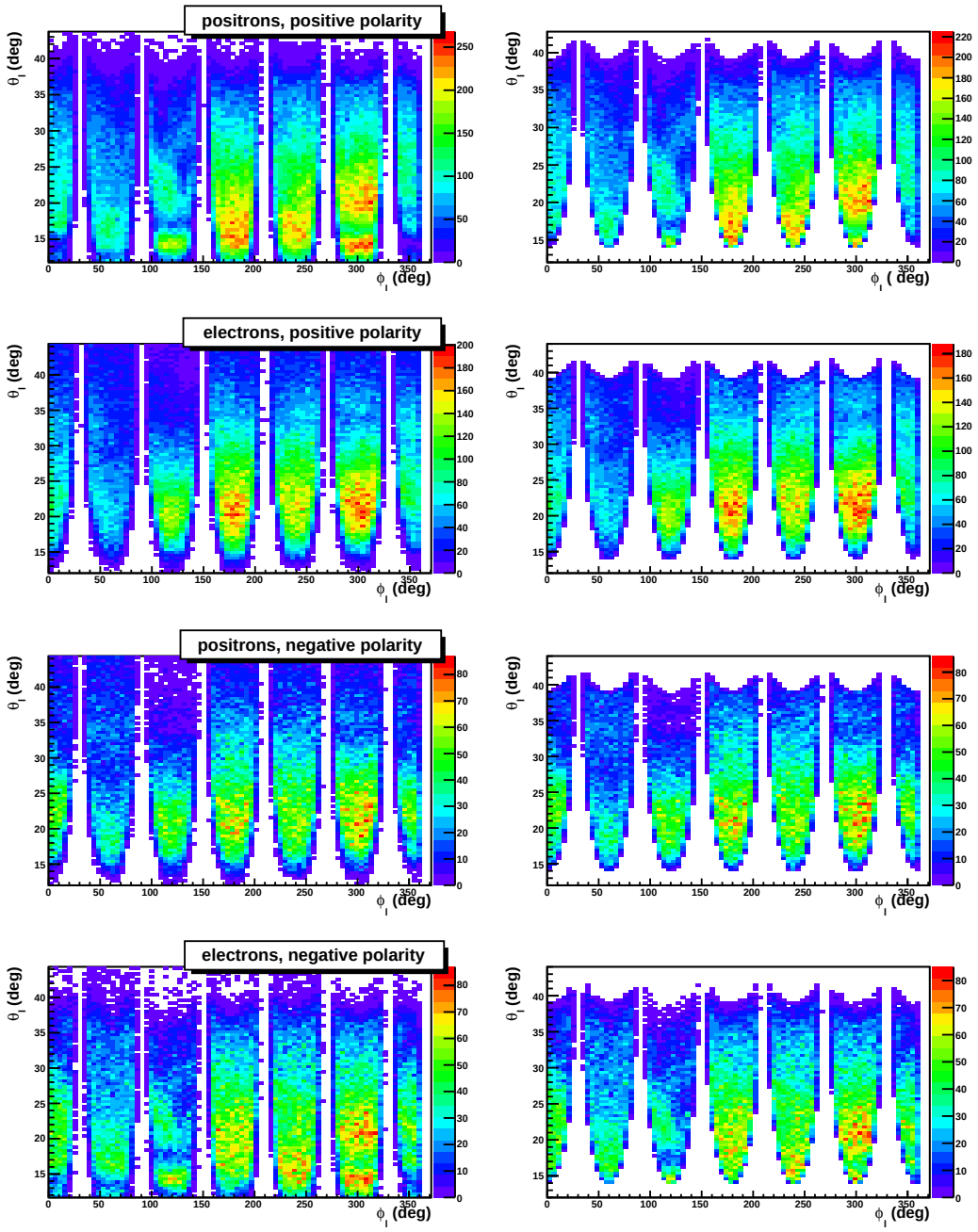

Figure 49: Lepton polar versus azimuthal angle distributions, Left: before, and Right: after the fiducial cuts for different torus polarity and beam types separately. All the kinematic cuts are included in both columns.

distribution. As shown in Fig. 50 this mass is very close to the proton mass after the kinematic and fiducial cuts.

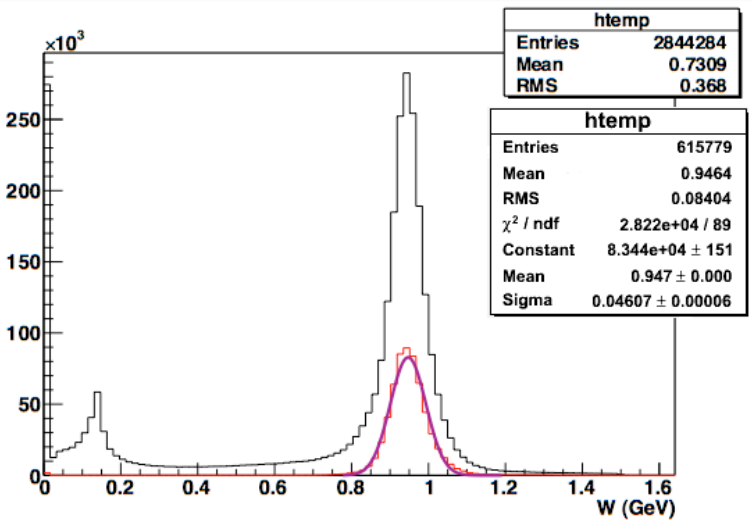

Figure 50: Invariant mass distribution, before (black) and after (red) imposing the kinematic and fiducial cuts.

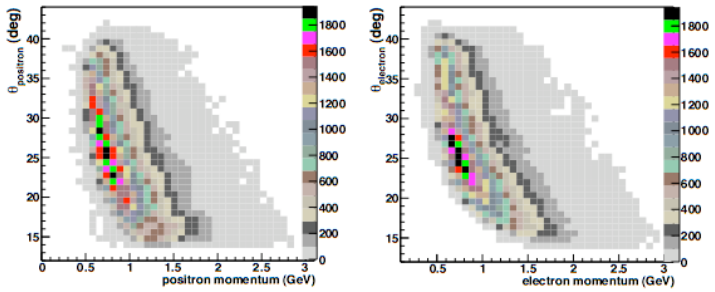

(a)

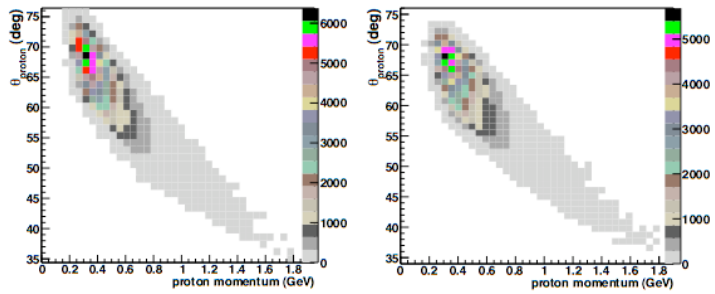

(b)

Figure 51: Scattering angle versus momentum distributions, for (a) leptons and (b) protons, with positive torus polarity.

The scattering angles for the electrons and positrons were investigated as well as the recoil angle of the protons. Applying all the cuts leaves the angular distributions well defined and within sensible ranges. As expected, the elastic leptons scatter at small laboratory angles, where the corresponding protons recoil toward larger polar angles. Fig 51 shows the polar angle distributions versus momentum for leptons and protons for both event types.

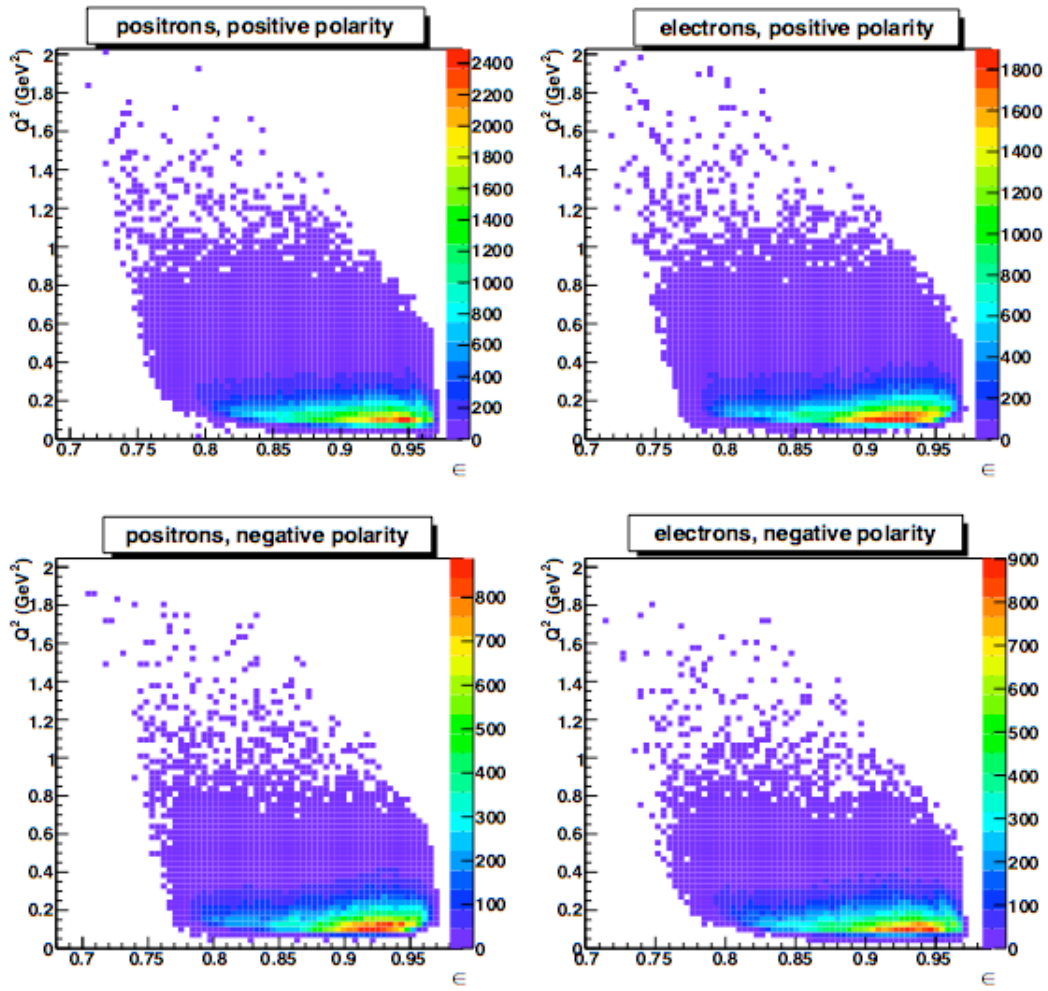

Figure 52: Q^2 versus ϵ distributions, compared for different torus polarity and beam type settings, after implementing all the kinematic and fiducial cuts.

The Q^2 vs. ϵ distributions for the two event types are shown in Fig. 52. Most of the data points are concentrated in low Q^2 and high ϵ ranges, which is expected due to the small scattering angle and low beam energy limitations.

$$Q^2 = \frac{4E^2 \sin^2(\theta/2)}{1 + (2E/M_p)\sin^2(\theta/2)} \tag{38}$$

$$\epsilon = \frac{1}{1 + 2(1 + (Q^2/4M_p))\tan^2(\theta/2)} \tag{39}$$

Here, E is the beam energy, θ is the lepton scattering angle, and M_p is the mass of proton.

4.3.3 Kinematic Bin Selection

After implementing the kinematic (elastic) and the volumetric fiducial cuts, the remaining events were binned into nine epsilon and four Q^2 bins in order to study the dependency of the cross section ratio on each of these variables. The bins were initially selected in such a way to have comparable statistical significance. Therefore, bins at higher event density regions of the Q^2 versus ϵ distribution were chosen to be much smaller than the ones located further out. The occupancy of the final bins ranged from 2-20k events for positive, and 0.6-9k events for negative polarity runs. The bin ranges and centers for each ϵ and Q^2 bin are shown in Fig. 53 and summarized in table 2. Note that partially filled bins have been excluded from our final results, since the acceptance for in-bending and out-bending particles tends to vary greatly at the edges of the distribution.

ϵ	Q^2 (GeV^2)	
Range	Range	Bin center
0.780 to 0.820	0.075 to 0.125	0.103
0.820 to 0.840	0.125 to 0.185	0.152
0.840 to 0.870	0.185 to 0.350	0.246
0.870 to 0.890	0.350 to 0.800	0.472
0.890 to 0.907		
0.907 to 0.921		
0.921 to 0.935		
0.935 to 0.950		
0.950 to 0.965		

Table 2: Bin ranges for ϵ and Q^2.

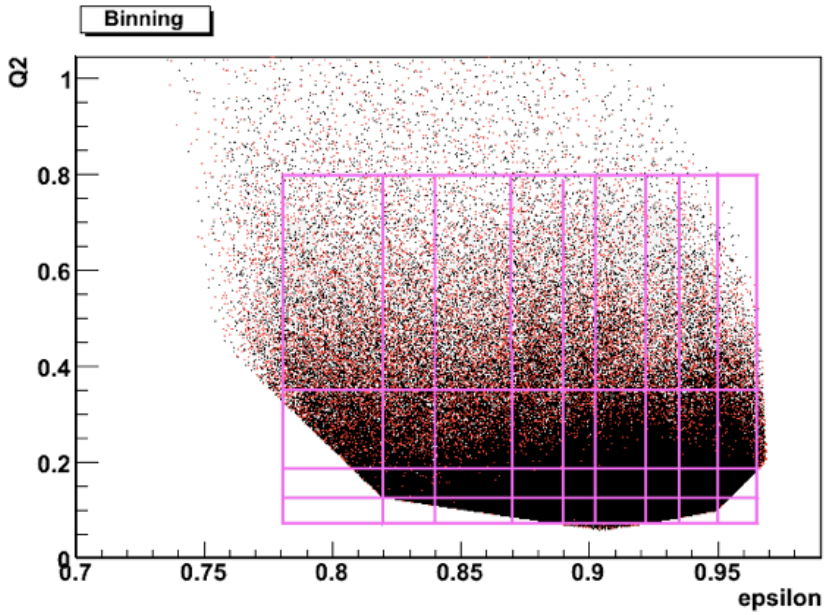

Figure 53: Binning scheme, shown for negative polarity for electrons (black) and positrons (red).

4.3.4 Acceptance Matching

Because this experiment was designed to precisely measure the electron-proton and positron-proton charge asymmetry ratio, it is extremely important to ensure that the range of acceptances over which these two types of events are detected are exactly the same. One way to check this was to incorporate a "swimming" algorithm into the analysis software. This algorithm was capable of calculating the particle trajectories through the CLAS detector geometry and magnetic field. It could also determine the hit positions on the detector planes. The acceptance matching was done as follows. In each event the charge of the identified lepton was reversed but its momentum and scattering angle were kept unchanged. The lepton and its charge-conjugate were "swum" (traced out) to the SC paddles. Both of these particles were required to intersect a good scintillator paddle (more than 85% efficiency). Otherwise, that event was discarded altogether. Fig. 54 shows this procedure for a primary positron that was switched to an electron for a negative torus polarity. It can be seen that they bend differently through the torus filed, and therefore, have different acceptance.

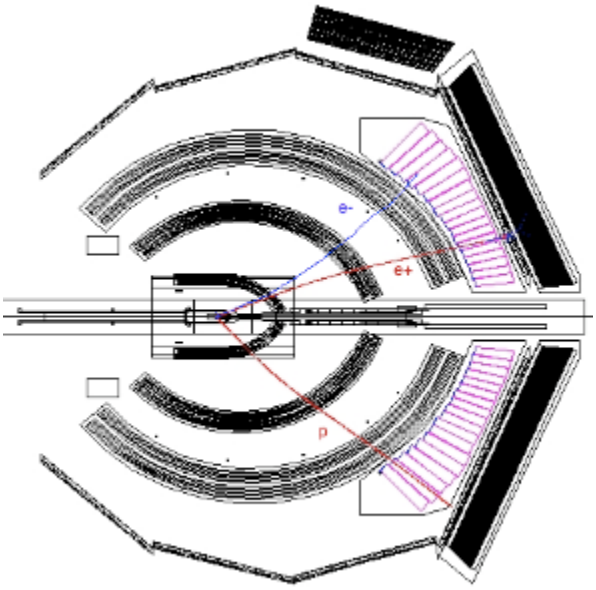

Figure 54: Sectional view of CLAS visualizing the swimming technique, for negative torus polarity.

In other words, the acceptance matching basically enforced both positrons and electrons to have the same chance of getting detected by a good SC paddle regardless of the torus polarity setting. The main purpose was to minimize the acceptance effect and the systematic uncertainty associated with this effect in the ratio calculation [51].

4.3.5 Acceptance Corrections

A more conventional method of incorporating the acceptance effects in the cross section calculations is through acceptance correction simulations. Because the cross section ratio is extremely sensitive to any possible acceptance asymmetries, simulation studies were done in addition to the swimming method described in the previous section.

The **G**EANT based monte-carlo **Sim**ulation package (GSIM) was used to perform the acceptance correction [52]. This simulation aimed to consider both the CLAS geometrical coverage and the detector efficiencies to extract the acceptance factors to normalize the cross section calculations, and involved several stages.

First, the elastic events were generated using ELAST-GEN package for electron-proton and positron-proton scattering separately. This event generator produces events with the elastic peak modified by vertex corrections according to the Mo-Tsai equation (II.6) and internal bremsstrahlung (radiative tails) calculated by Monte-Carlo sampling [53].

The simulation was further modified for this study by making it capable of using a continuous beam-energy distribution (instead of a single valued beam energy) close to what was reconstructed in the analysis after imposing the kinematic and the fiducial cuts. This distribution, however, still had the detector acceptance built into it, and was normalized by a factor found through a separate set of simulations with a flat beam energy distribution. The normalized distribution was fit by a Landau function and regenerated by the event generator. Fig. 55 further clarifies the above description.

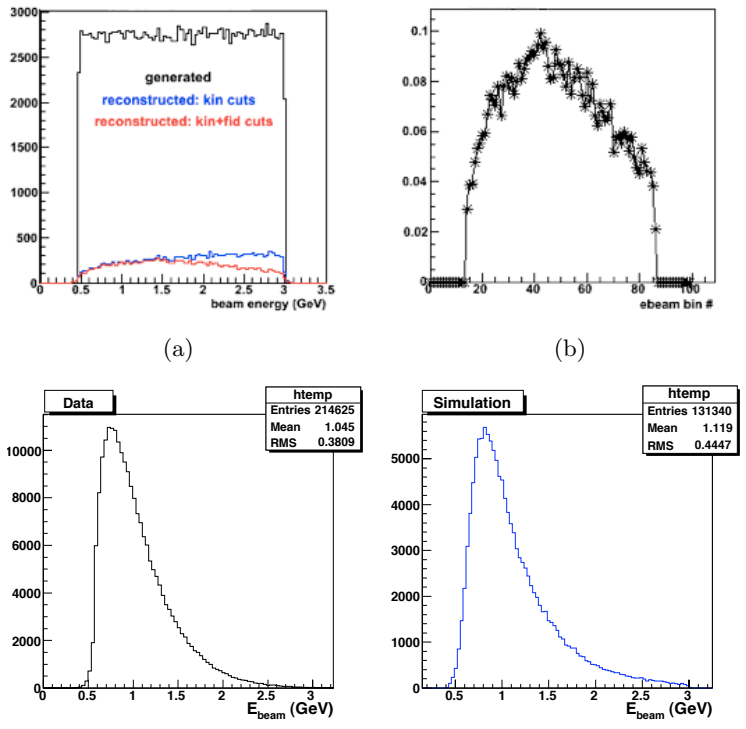

Figure 55: Beam energy distributions, (a) generated (flat) compared to the reconstructed, and (c) data (left column) versus simulation (right column), for electron beam with positive torus polarity. Also the extracted normalization factor per bin is shown in (b).

A total of 8M events were generated, 4M events for each beam particle. The generated events were then fed to the GSIM package for the detector response simulation. The tracks were swum through the detailed CLAS elements and produced hits on the corresponding detectors. The polarity of the torus magnet was reversed in the simulation just like the testrun. Therefore, there were four different settings simulated: positron beam/positive torus polarity, positron beam/negative torus polarity, electron beam/positive torus polarity and electron beam/negative torus polarity.

The simulated data were then run through the **G**SIM **P**ost **P**rocessor (GPP) package, used to smear the detector resolutions by adding a random time delay to different detector components. Also the dead or low efficiency detector channels were removed in order to resemble the actual running conditions. The detector efficiency information needed for this step of the simulation was kept in distinguished tables in the calibration database for the TPE experiment.

Finally, the smeared results were processed using the RECSIS package with the exact same criteria as were used to cook the actual data. In this step, the tracks were reconstructed in the same manner as they would be for the raw data set, and run through the "bos2mu" software [54] for formatting and compression. The simulated data were analyzed by the same analysis code and same set of cuts used for the data. As seen in Fig. 56 there is reasonable agreement between data and simulation scattering angles, as well as in Q^2 vs. ϵ distribution.

The acceptance correction factor was calculated for each Q^2 and ϵ bin, by taking the ratio of the reconstructed and generated events that fall within that specific bin. The uncertainty associated with the acceptance factor is also calculated for each bin as follows:

$$A_i = \frac{N^i_{rec}}{N^i_{gen}} \tag{40}$$

$$\delta A_i = \sqrt{\frac{A_i(1-A_i)}{N^i_{gen}}} \tag{41}$$

where A_i is the acceptance correction factor for the ith bin, N_{rec} and N_{gen} are the reconstructed and generated number of events respectively. These values where extracted for

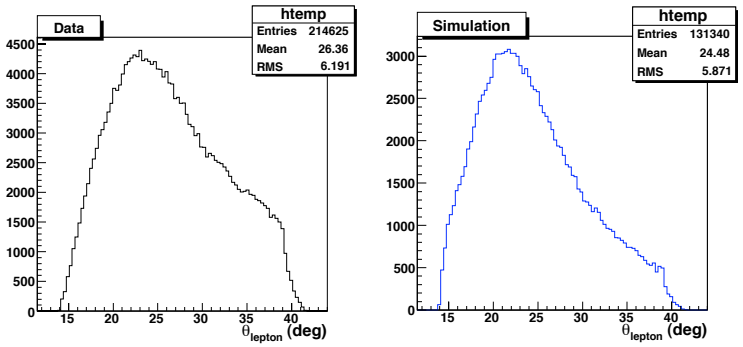

(a)

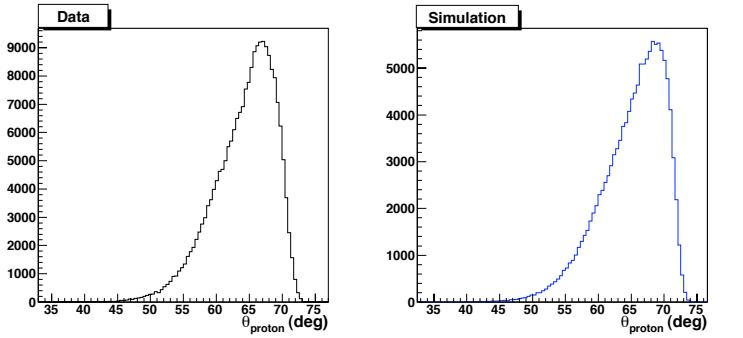

(b)

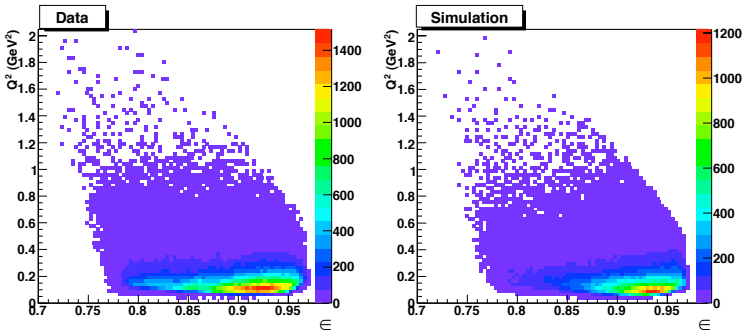

(c)

Figure 56: Scattering angle and Q^2 vs. ϵ distributions. (a) Lepton, and (b) proton scattering angles. (c) Q^2 vs. ϵ for data (left column) and simulation (right column), for electron beam with positive torus polarity.

each experimental setting as shown in Fig. 57. As expected, the acceptance for e^+p positive polarity is similar to the e^-p negative torus polarity, as is for all the other kinematic distributions.

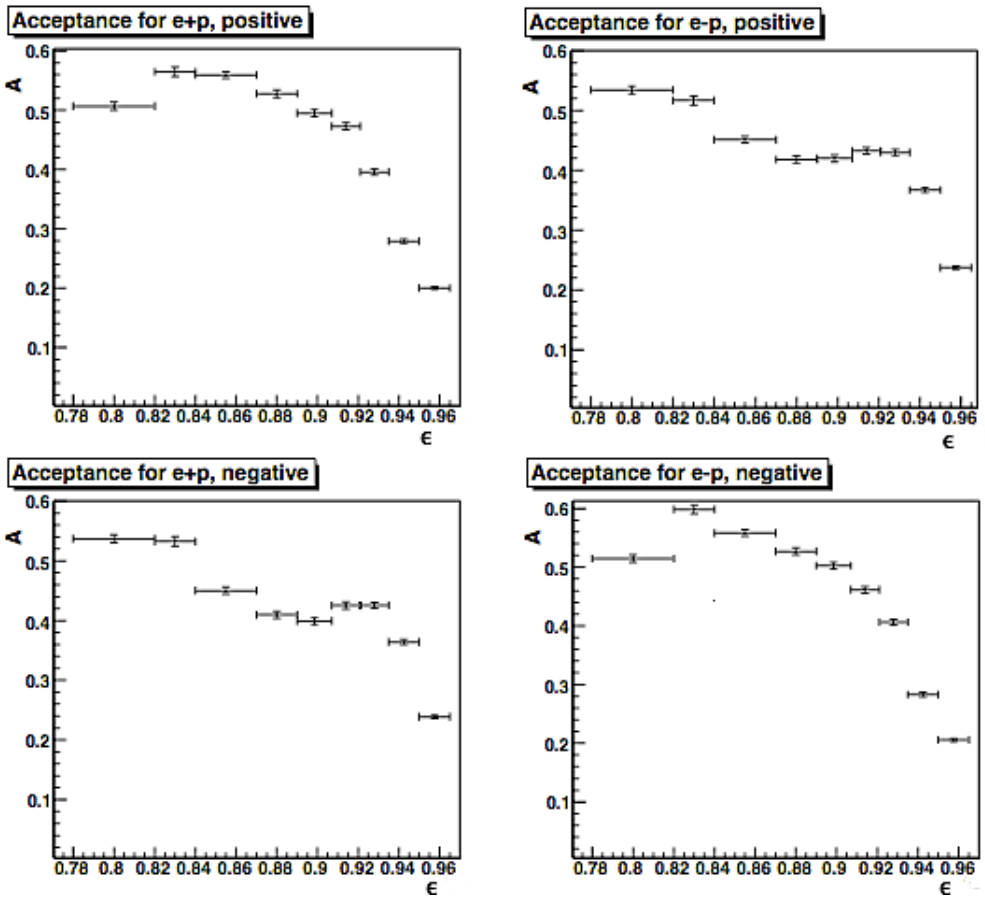

Figure 57: Acceptance factors for different beam type and torus polarities, for a single Q^2 bin ($0.185 < Q2 < 0.35$).

4.3.6 Detector Inefficiency Corrections

The detector inefficiencies were accounted for in both acceptance simulations and acceptance matching methods separately. Inefficiency means the involvement of any dead, broken or weak detector subsystem in the event selection, and most importantly, the ratio extraction. In fact, a large asymmetry in cross section ratio was observed in opposite torus polarities. Therefore, the mentioned inefficient detector channels were simply excluded from the analysis and the acceptance simulation, to neutralize their biased effect on electron versus positron detection. The two most important detectors in this analysis were the ToF scintillator paddles and the drift chambers, each corrected separately as discussed in this section.

4.3.6.1 TOF Scintillator Paddles

A set of sector-dependent cuts were implemented in the acceptance matching technique and the acceptance correction simulations described previously. The ToF scintillator paddles that had unexpectedly lower count rates than the neighboring paddles, were removed by these cuts. As a result, all events where the scattered lepton was incident on these paddles were discarded. Fig. 58 shows the lepton momentum versus paddle number for each sector of the ToF detector. The low-efficiency (bad) paddles, which have extremely low occupancy for the entire momentum range, can be visually identified. These paddles are listed in table 3. Note that sector 3 has the largest number of bad paddles.

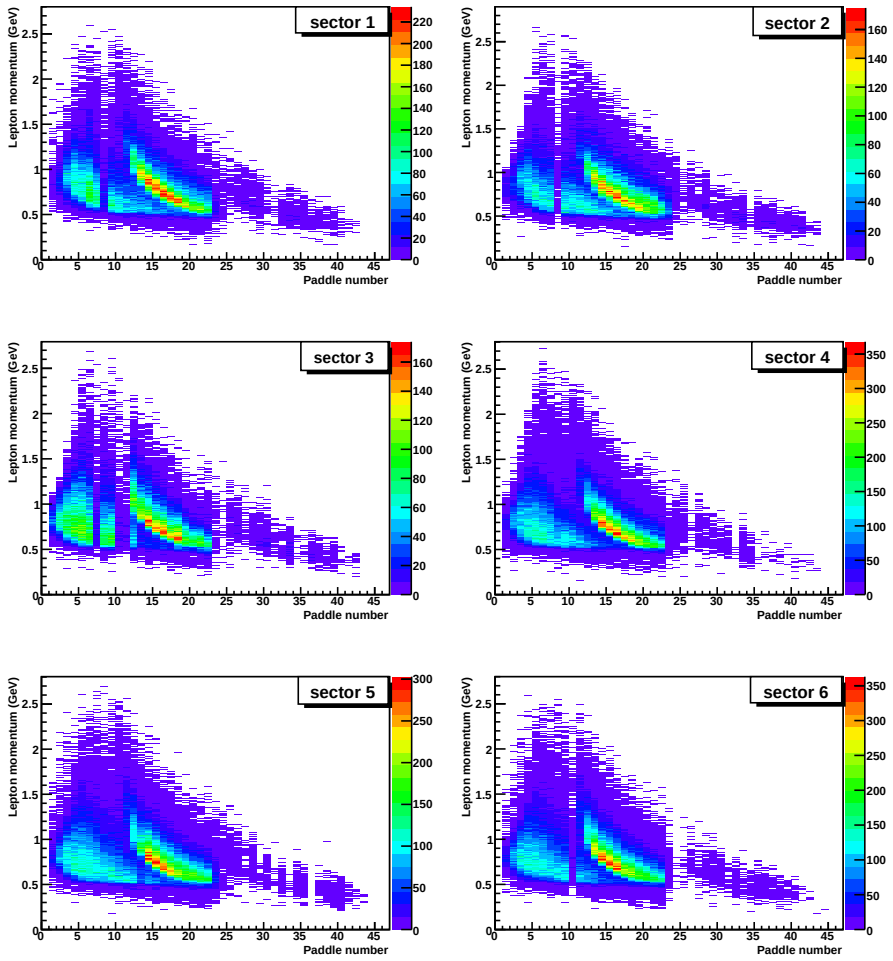

Figure 58: Lepton momentum vs. TOF paddle number, for individual sectors and all beam types and torus polarities.

sector	bad paddles
1	6,8,32
2	8,25,34
3	7,10,11,24,34,35
4	22,26,32
5	36
6	10,24,25

Table 3: Bad paddle list for the TPE experiment.

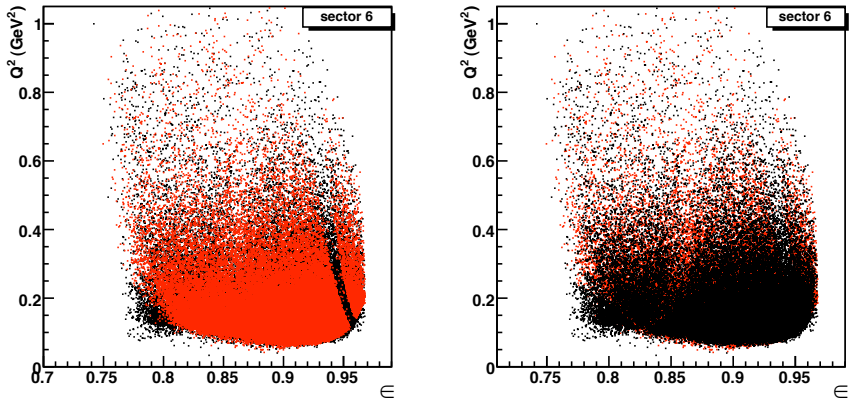

(a)

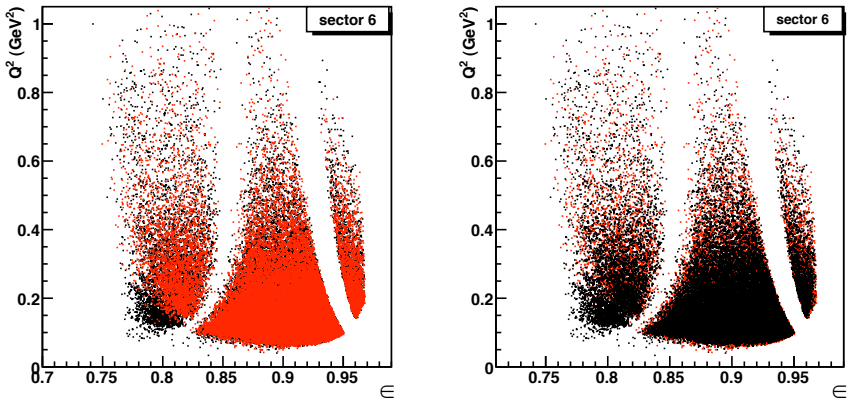

(b)

Figure 59: Bad paddles in Q^2 vs. ϵ distribution, (a) before, and (b) after the acceptance matching, for sector 6 and positive torus polarity only. The electrons are shown in black and positrons in red, which are drawn in reversed order in each subfigure. The holes corresponding to bad paddles are clearly cut out by the acceptance matching.

This correction was of key importance in the acceptance matching method, due to the fact that for the same torus polarity, different lepton types see a different set of bad paddles on the path they traverse. The bad paddle cut, knocks out the same bad paddles for both leptons, no matter how they bend through the magnetic field. This can be clearly seen in the Q^2 vs. ϵ distribution plotted in Figs. 59(a) and 59(b). The bad paddles were knocked out separately while analyzing the acceptance simulated data, in order to correctly resemble the true experimental conditions.

4.3.6.2 Drift Chamber Wire Mapping

The drift chamber dead or inefficient wires were also taken into account mainly for acceptance simulation purposes. The first step was to identify these wires during the data cooking process. The processed "pdu" files were used to calculate the efficiency for the wires and find correlations between them.

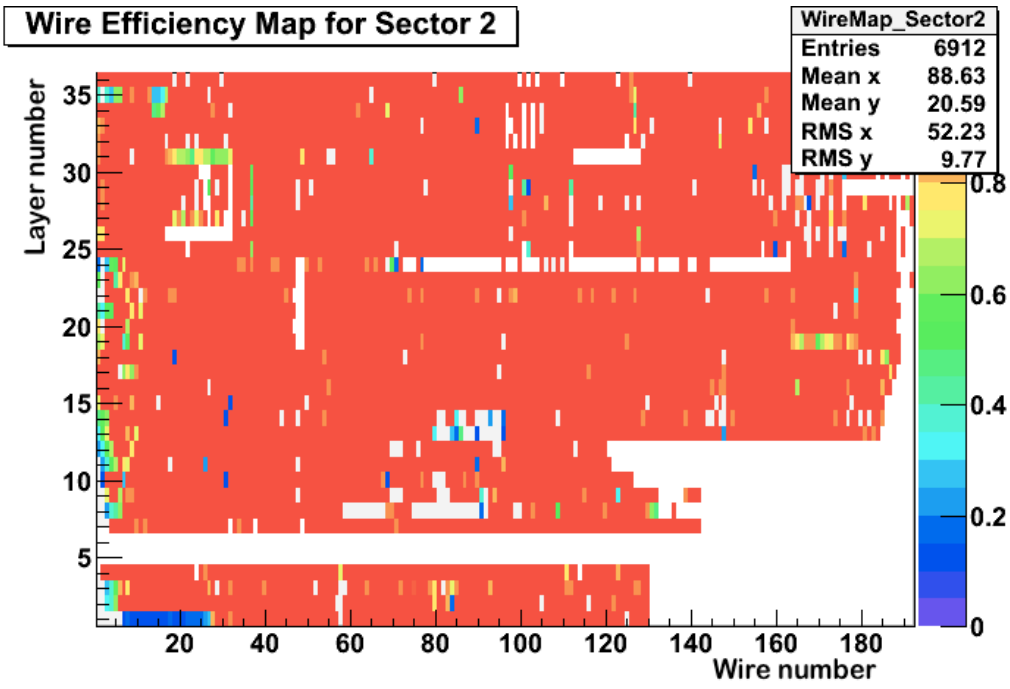

Figure 60: The drift chamber mapping for sector 2, performed by [54].

The "Ungaro-Li" algorithm was utilized for this calculation [55]. This algorithm compares the occupancy of a certain wire to its neighboring wires and the corresponding ones in all other sectors. Then it assigns an expectation value to the group by finding the wire with the most "buddies" (buddy means the number of wires in that group with occupancies within a certain percentage of that wire), and averaging over their occupancies. The efficiency of any wire in this group is simply its occupancy normalized by the expectation value. The wire efficiencies were then copied to the calibration database and were read and implemented by the GPP routines, during the simulation smearing process.

4.3.7 Summary

The elastic scattering events were cleanly extracted by applying several cuts described in this chapter. Implementing these direct cuts did not critically reduce the statistical significance of this study. After performing a number of corrections to take the acceptance differences into account, the study of the cross section ratios began.

In the following chapter, the ratios are extracted, their dependencies are investigated and the results are presented. Also the systematic uncertainties are evaluated and discussed in detail.

5 Results and Discussion

5.1 Charge Asymmetry Ratio

The elastic cross section,

$$\sigma = \sigma_{Mott}\left(\frac{1}{1+\tau}\right)\left[G_E^2(Q^2) + \frac{\tau}{\epsilon}G_M^2(Q^2)\right], \tag{42}$$

can be found directly by normalizing the number of detected events by several factors such as the acceptance corrections, A, the luminosity, $\mathcal{L}$, and radiative corrections, f_{rad}.

$$\sigma \propto \frac{N}{A\mathcal{L}f_{rad}} \tag{43}$$

Using this description, the yield ratio was calculated by dividing the acceptance corrected number of events (yield) for the final positrons by the one for the final electrons. The acceptance effect was found to be the single most important factor that dramatically changed from one lepton beam type to another. The ratio of the beam flux for the electrons to positrons was simulated and found to be unity to within 1%. This factor is included in the systematic uncertainty estimation and will be discussed more in section 5.5. The detector efficiency changes for the two particles are taken into account both by the acceptance calculations and by reversing the torus polarity setting during the experiment, as discussed before. Also the standard radiative correction effects for positrons and electrons are the same. Therefore, only the acceptance factor was considered in extracting the e^+/e^- ratio.

For each kinematic bin, the number of events after all cuts were found for positron- and electron-scattering events and for each polarity setting separately. The ratio and its uncertainty are then;

$$R_\pm = \frac{N_\pm^{e^+p}}{N_\pm^{e^-p}}, \tag{44}$$

$$\delta R_\pm = R_\pm.\sqrt{\left(\frac{\delta N_\pm^{e^+p}}{N_\pm^{e^+p}}\right)^2 + \left(\frac{\delta N_\pm^{e^-p}}{N_\pm^{e^-p}}\right)^2} = R_\pm.\sqrt{\left(\frac{1}{N_\pm^{e^+p}}\right) + \left(\frac{1}{N_\pm^{e^-p}}\right)}, \tag{45}$$

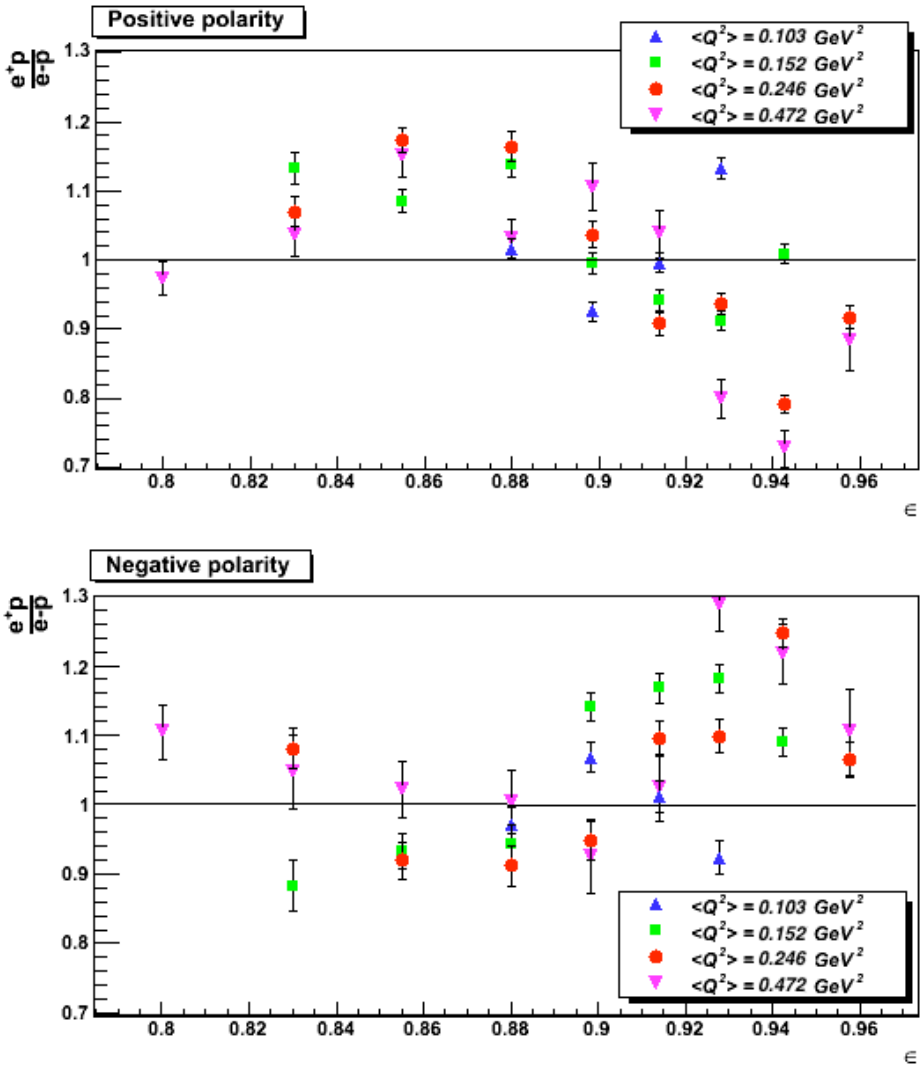

Figure 61: Positron- to electron-proton event ratio vs. ϵ before any corrections, for Top: positive, and Bottom: negative torus polarities. Q^2 bins are shown in different markers and colors.

where $\pm$ corresponds to the torus polarity setting in each case. Figure 61 shows the ϵ-dependence of the this ratio for different Q^2 bins with no acceptance corrections.

5.1.1 Acceptance matched Ratio

If the acceptance matching (swimming) restriction is imposed on the binned data, the asymmetry differences between in-bending and out-bending leptons in each polarity is reduced.

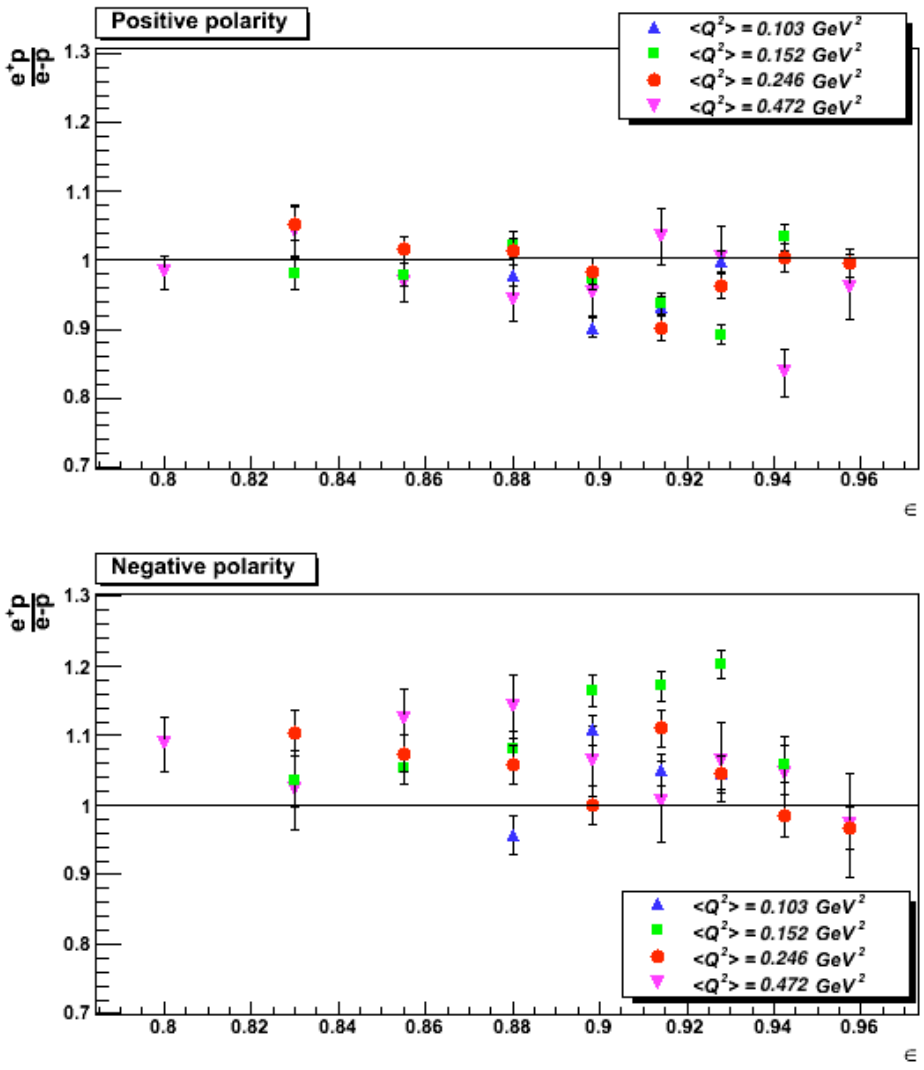

Figure 62: Positron- to electron-proton event ratio vs.ϵ after acceptance matching, for Top: positive, and Bottom: negative torus polarities, and different Q^2 bins.

The detector inefficiencies were built into this technique. Fig. 62 illustrates the reduced acceptance-related-asymmetry between the two polarities, as compared to Fig 61.

In order to factor out the remaining acceptance related difference in the $\frac{e^+p}{e^-p}$ ratio, the results for the two polarities were combined to yield the polarity independent ratio:

$$R = \sqrt{(R_+)\,(R_-)} \tag{46}$$

$$\delta R = \left(\frac{1}{2R_-\sqrt{R}}\right)\sqrt{\delta R_+^2 + (R^2\delta R_-)^2} \tag{47}$$

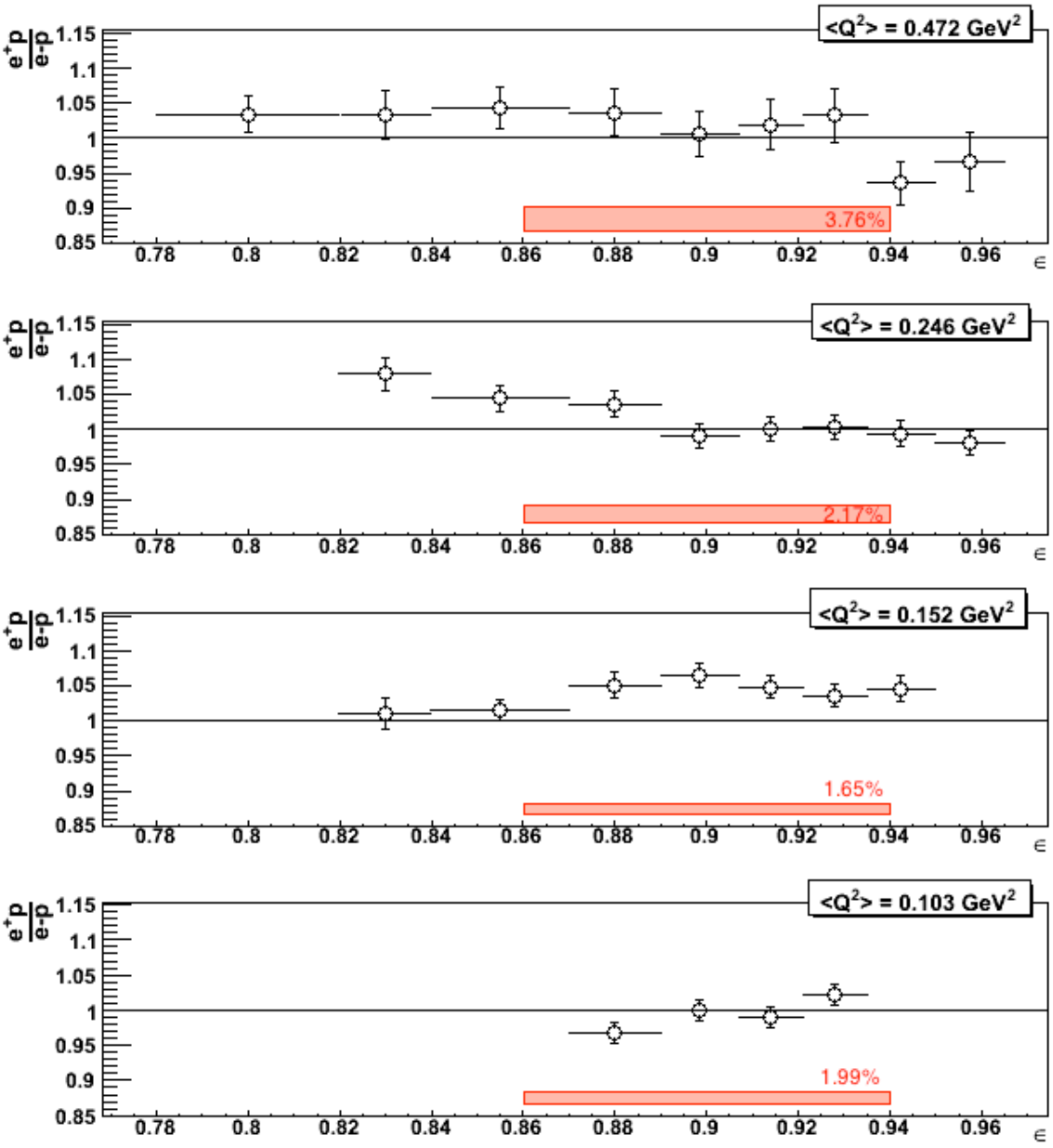

Figure 63: Charge asymmetry ratio for the acceptance matched data, separately shown for different Q^2 bins as a function of ϵ. The size of the total systematic uncertainties (1σ) are shown by the height of the boxes for each Q^2 bin, and will be discussed in detail in section 5.2.

The results of this calculation is presented in Fig. 63 for each Q^2 bin individually. This total ratio is also called the charge asymmetry ratio.

5.1.2 Acceptance Corrected Ratio

The bin occupancy was also normalized by the acceptance correction factor found in section 4.3.5, as a cross check for the acceptance matching results. The acceptance ratio was found by taking the ratio of the positron and the electron acceptance factors for each bin of each polarity. The uncorrected charge yield ratio was then divided by the acceptance ratio to yield the corrected charge asymmetry ratio. The statistical uncertainty for the acceptance ratio and the corrected charge asymmetry were derived as seen in equations 49 and 51.

$$R_{\pm}^{acc} = \frac{A_{\pm}^{+}}{A_{\pm}^{-}} \tag{48}$$

$$\delta R_{\pm}^{acc} = R_{\pm}^{acc}\sqrt{\left(\frac{\delta A_{\pm}^{+}}{A_{\pm}^{+}}\right)^{2} + \left(\frac{\delta A_{\pm}^{-}}{A_{\pm}^{-}}\right)^{2}} \tag{49}$$

$$R_{\pm}^{corr} = \frac{R_{\pm}}{R_{\pm}^{acc}} \tag{50}$$

$$\delta R_{\pm}^{corr} = R_{\pm}^{corr}\sqrt{\left(\frac{\delta R_{\pm}}{R_{\pm}}\right)^{2} + \left(\frac{\delta R_{\pm}^{acc}}{R_{\pm}^{acc}}\right)^{2}} \tag{51}$$

The corrected total charge asymmetry ratio, shown in Fig. 64, has a very similar distribution to the acceptance matched results albeit with larger uncertainties. As shown in section 5.2, these results can be compared to the acceptance matched ratio in order to estimate the acceptance related systematic uncertainties.

5.2 Systematic Uncertainties

An important goal of the TPE test run was to minimize the systematic uncertainties every step of the way, as the charge asymmetry is very small and any systematic uncertainty can easily make it impossible to be measured precisely. In spite of adapting several strategies to reduce these effects, some sources of uncertainty still remain that need to be carefully estimated and accounted for. The most important sources were carefully studied, and are presented in this section.

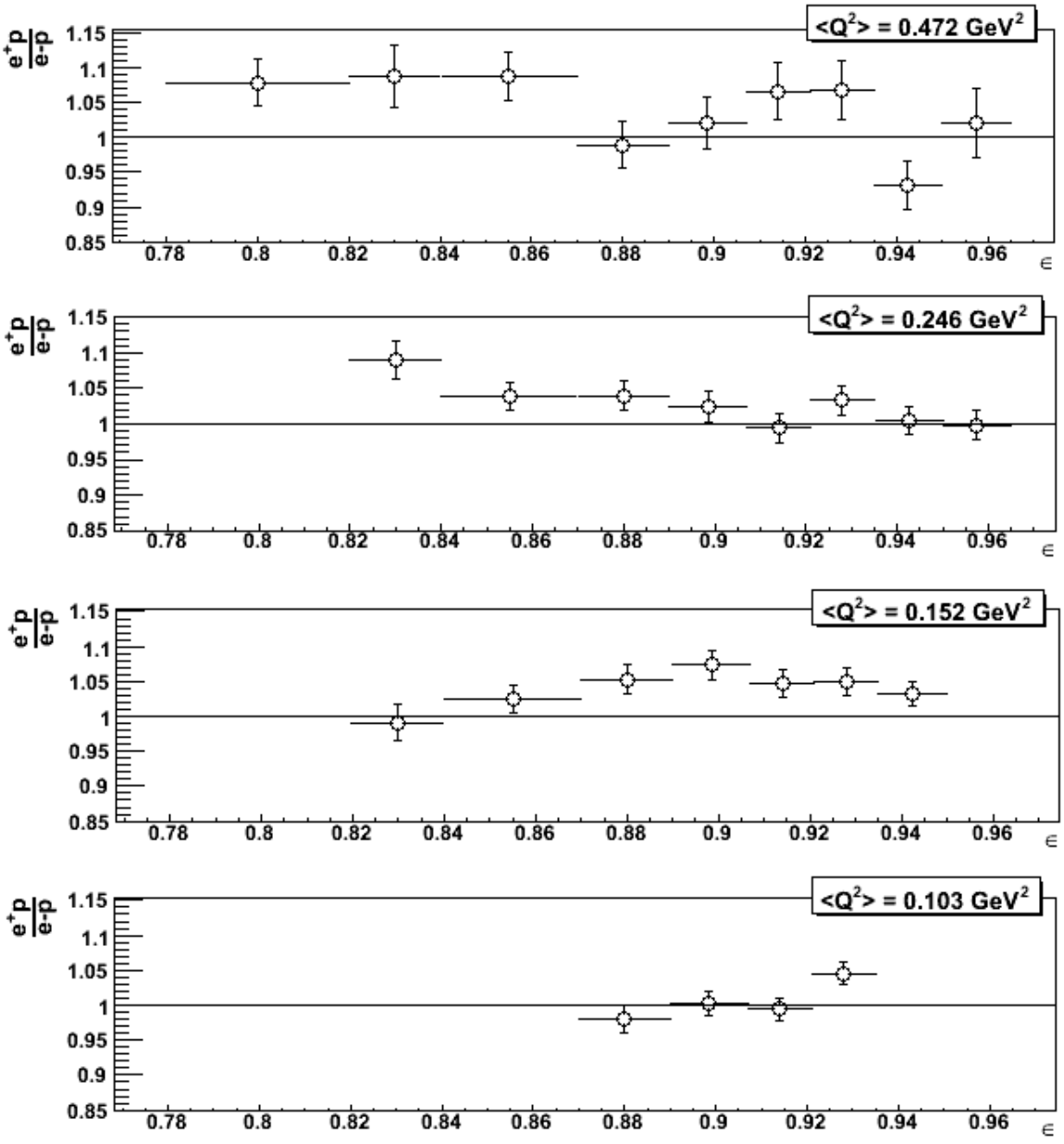

Figure 64: Charge asymmetry ratio after performing acceptance corrections, separately shown for different Q^2 bins as a function of ϵ.

- **Luminosity Differences**

  The difference in the electron and positron luminosity was entirely due to their incident flux. Despite the fact that the beam flux was monitored live throughout the run period, asymmetries are inevitable and can introduce an uncertainty to the results.

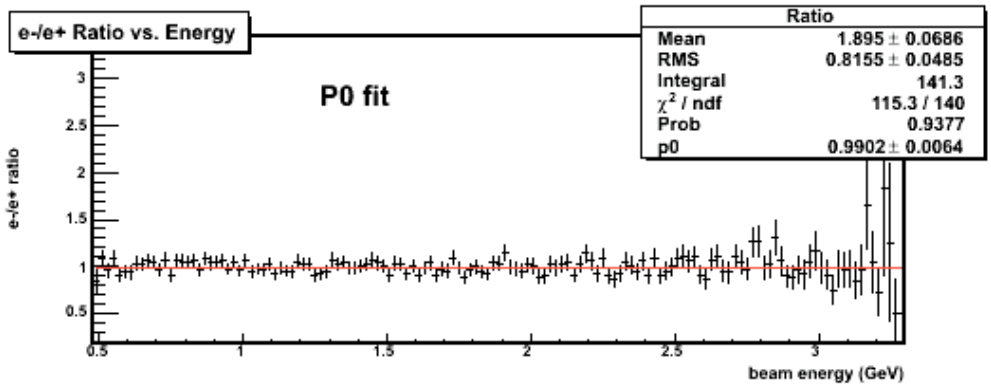

Figure 65: Electron to positron beam flux ratio vs. beam energy, fit with a linear function.

Although the leptons are produced as a pair in the converter, there are possible differences in their attenuation in different beamline materials and their trajectories through the magnetic field [19]. This subject was studied further by performing a detailed monte-carlo simulation of the beam from the moment of its incidence upon the radiator to when the secondary beam was scattered off the target. The beamline was implemented in the simulation in great detail. Figure 65 shows the ratio of the electron and positron flux on the target as a function of beam energy. A constant fit to the ratio indicates a slightly higher positron flux than electron flux. Because there are no known processes that would lead to this asymmetry, it has been assumed that it is a result of statistical fluctuations in the simulation. A 1% systematic uncertainty has been assigned to the flux ratio.

- **Acceptance Differences**

  The acceptance related uncertainties were reduced using several methods. Reversing the torus polarity, enforcing fiducial and acceptance matching cuts and normalizing by the acceptance factor were all effective solutions. However, it was concluded that the acceptance is still the main source of the remaining systematic uncertainty. The contribution of this uncertainty to the total error bar was found by comparing the charge asymmetry calculated using the swimming technique with the results normalized by the acceptance correction. The difference in charge asymmetry ratio is shown

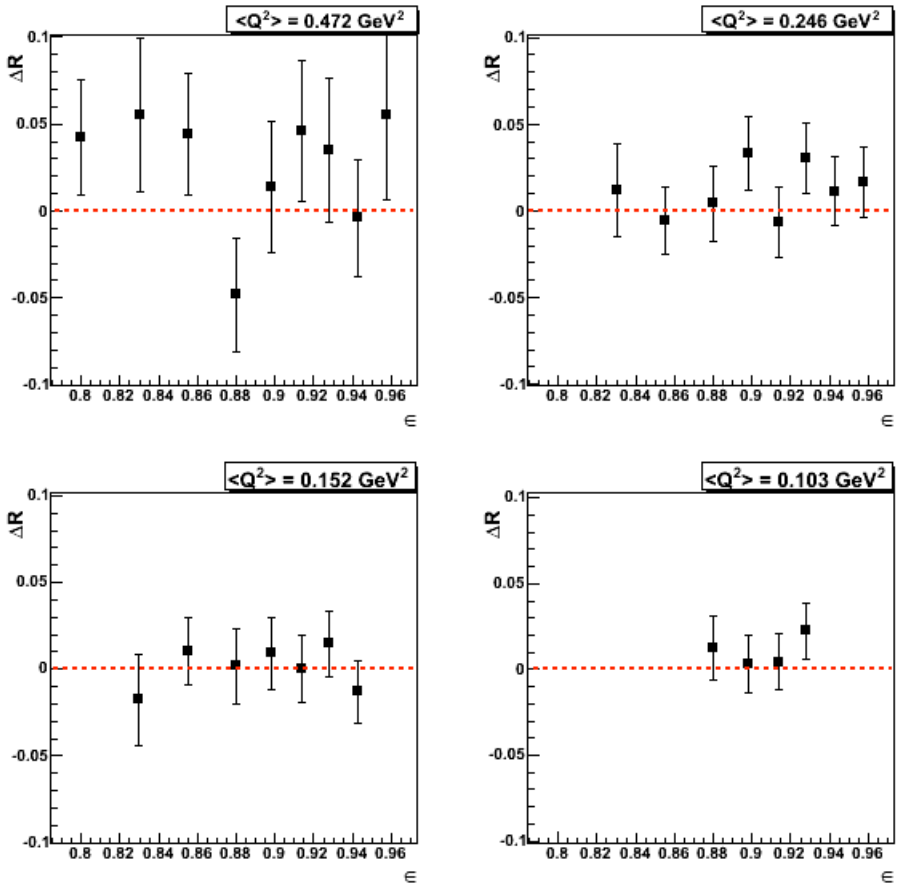

Figure 66: Difference between the swimming and acceptance corrected ratio, for different Q^2 bins.

in Fig.66. The weighted mean of this difference was taken as an estimate for the acceptance related uncertainty for each Q^2 bin.

- **Kinematic Cut Studies**

  The systematic effect related to the choice of elastic kinematic cuts were also studied in detail, by removing each cut entirely and calculating the changes in the charge asymmetry ratio for each Q^2 bin. Removing the entire cut as opposed to adjusting it to different ranges, was actually an over estimate that was assumed to be an upper limit for this uncertainty. As before, the weighted mean of the difference between the ratio with all the cuts and each cut excluded individually, yields the systematic uncertainty per Q^2 bin. The studies showed that the main systematic uncertainties

$< Q^2 >$ (GeV^2)	$\delta R_{\mathcal{L}}$	δR_A	δR_{DoCA}	$\delta R_{\Delta E_{beam}}$	δR_{total}
0.103	0.01	0.0105	0.0055	0.0125	0.0199
0.152	0.01	0.0014	0.0089	0.0096	0.0165
0.246	0.01	0.0116	0.0081	0.0131	0.0217
0.472	0.01	0.0214	0.0071	0.0284	0.0376
Total	0.01	0.0071	0.0088	0.0128	0.0198

Table 4: Systematic uncertainties for each Q^2 bin. "Total" represents the case where all the Q^2 bins are combined for the Q^2 range of $0.125 - 0.4$. The total uncertainty for the combined bins is illustrated in sections 5.4 and 5.5.

are related to the DoCA and ΔE_{beam} cuts that are about 1%. The effects of the rest of the cuts were found to be negligible.

The total systematic uncertainty was the quadratic sum of the individual uncertainties and averaged to about 2.4%. These are summarized in table 4 and illustrated in Fig. 63.

5.3 TPE Correction, $\delta_{2\gamma}$

As explained in section 1.5 of this document, a direct measurement of the TPE correction can be extracted from the charge asymmetry ratios, using $\delta_{2\gamma} = \frac{1-R}{2}$, where R is the charge asymmetry ratio.

The TPE correction factor for each bin was individually determined using the ratio results from the acceptance matching technique and is plotted in figure 67. This value seems to be clearly ϵ dependent. It is also slightly Q^2 dependent as we move to lower Q^2 bins, but consistent for the two higher Q^2 bins. The parameters for the linear fits to the TPE correction factor as a function of ϵ are summarized in table 5.

Q^2 (GeV^2)	0.472	0.246	0.152	0.103
slope	0.236±0.213	0.335±0.168	-0.154±0.188	-0.471±0.417
intercept	-0.215±0.188	-0.309±0.153	0.118±0.169	0.429±0.378

Table 5: TPE correction fit parameters for different Q^2 bins.

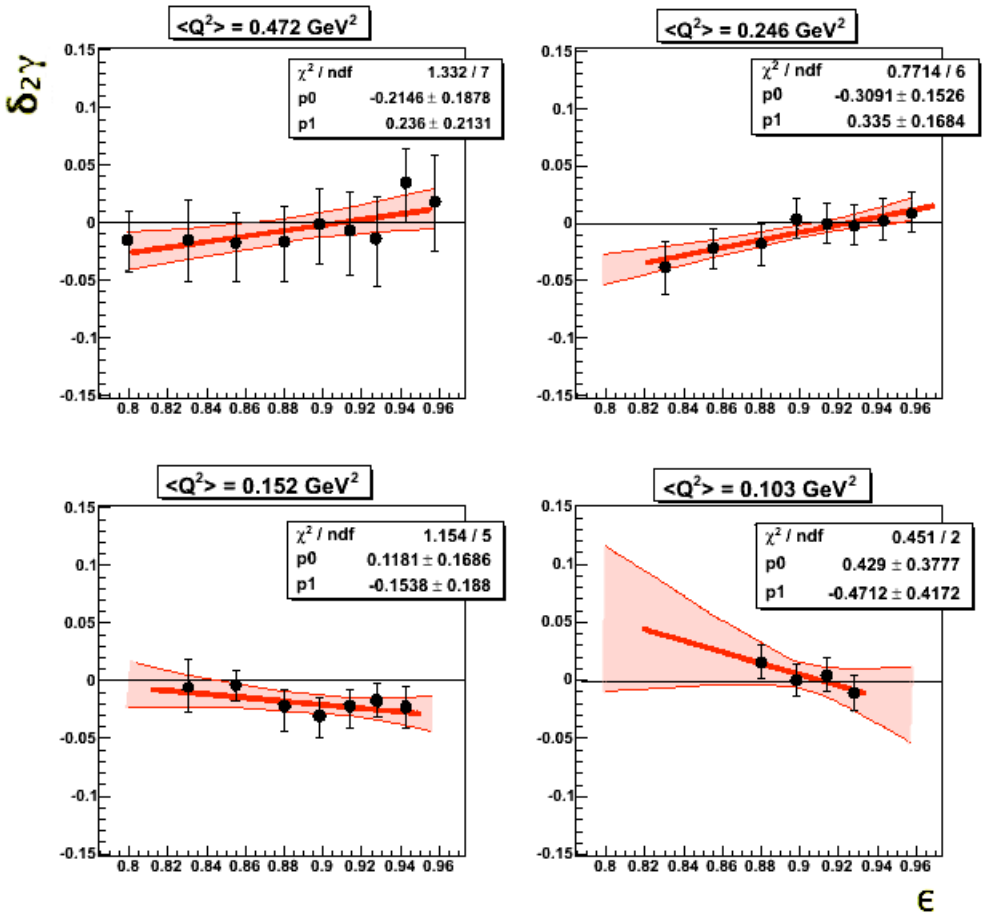

Figure 67: TPE correction factor vs. ϵ, for different Q^2 bins. The 95% confidence intervals for the linear fits are highlighted by the red band. Error bars are purely statistical.

5.4 Comparison to Previous Measurements

The final results of the positron- to electron-proton charge asymmetry ratio shown previously in figure 63 is plotted here against the world data for comparison. This is shown in figure 68, where the red solid circles present the results found by this study for a single Q^2 bin of $0.125 - 0.4$ GeV^2. Note that the lowest Q^2 and the lowest and highest ϵ bins were disregarded in this study due to their partial occupancies. As mentioned in chapter 1, the world data points are measured at a wide range of Q^2 from $0.1 - 5.0$ GeV^2. Therefore, only the points with a Q^2 of $0.125 - 0.4$ GeV^2 (blue) were compared with our results. These points were combined and linearly fit to the TPE ratios to yield a slight ϵ dependence.

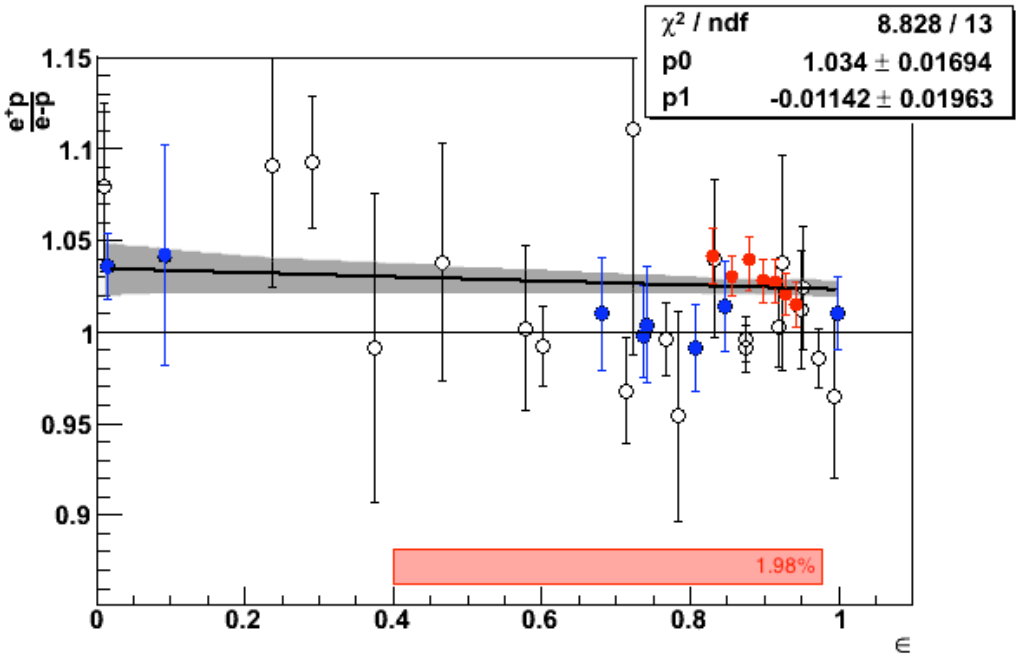

Figure 68: Charge asymmetry ratio overlaid on the world data. The world data points (hollow circles) with a comparable Q^2 (solid blue circles) are fit along with the data of this experiment (solid red circles), to estimate the size of TPE over a larger ϵ range. A linear fit to the world data only, yields a slope of -0.057 ± 0.018 [20].

The magnitude of the TPE data seems consistent with the world data in the respective ϵ range. The error bars shown for this data are purely statistical and look reasonably smaller than the world data. The size of the calculated systematic uncertainty is shown by the box.

5.5 Comparison to Theoretical Predictions

A quick glance at the comparison between the TPE charge asymmetry data for a single Q^2 bin, and the theoretical predictions, reveals some similarities of the shape of the ϵ dependence with the axial-VMD fit. The data from Mar *et* al. studies from SLAC [26], agrees with the TPE points to a good extent. However, these data were collected at a relatively high Q^2 compared to the current data. The factorized partons and GPD models appear to have a weaker ϵ dependence than the TPE data suggests, although it is calculated at $Q^2 = 5$ GeV^2. The elastic model by Blunden, however, seems to fall within the total uncertainty of these data over the ϵ range.

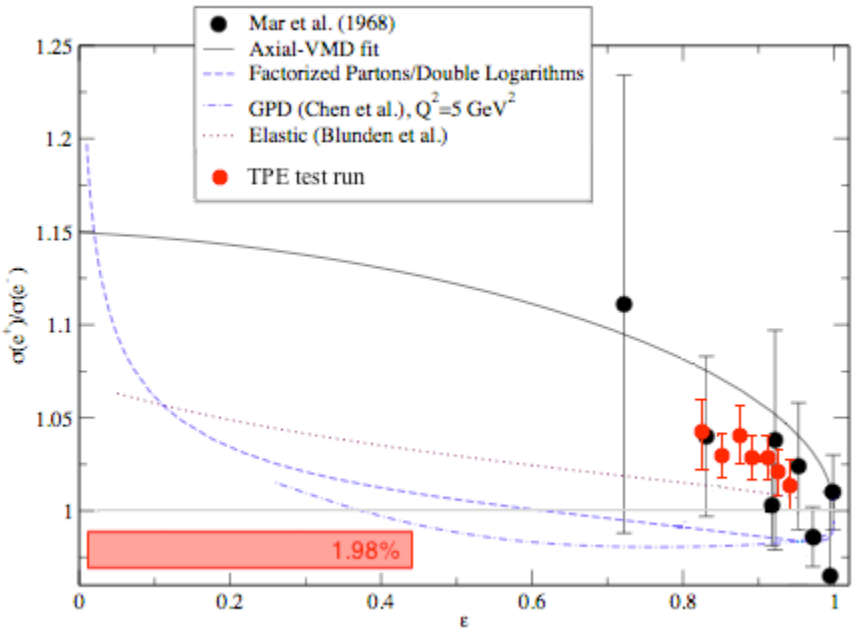

Figure 69: Charge asymmetry ratio overlaid on the theoretical models. The data of this experiment are presented with solid red circles, the models with different lines, and the SLAC data with solid black circles.

5.6 Conclusion

This study was a full analysis of the TPE test run, initially intended to be an engineering test of the beamline design, but turned out to be much more. The charge asymmetry extracted from this dataset not only fell close to the previous measurements, but also displayed an ϵ-dependence similar to the TPE estimates of several models. The Q^2 dependence was negligible at Q^2 values larger than 0.2 GeV^2. This has in fact been predicted by most of the existing models [19].

Although the present results cover an extremely limited range of kinematics, the data can clearly constrain the theoretical models at high ϵ. A none-zero TPE correction factor ($\delta_{2\gamma}$) was observed that was ϵ and Q^2 dependent. Much higher luminosity is needed to scatter the leptons to larger angles, and reach out to lower ϵ values where the TPE effect is predicted to be the largest. This requires a higher beam energy and current, minimum background rates and a longer run period.

The goal of the future TPE experiment is to continue this work and extend the kinematics considerably into higher Q^2 and lower ϵ ranges. The result presented in this dissertation guarantees the future TPE research to be a success.

REFERENCES

[1] R. Feynman. *Quantum Electrodynamics*. Westview press, (1998).

[2] M.N. Rosenbluth. High energy elastic scattering of electrons on protons. *Phys. Rev.79*, 615, (1950).

[3] S. Dubnicka, E. Kuraev, M. Secansky, A. Vinnikov. Polarization transfer measurements of proton form factors: deformation by initial collinear photons. *arXiv:hep-ph/0507242v2*, 2, (2006).

[4] F. Halzen, A.D. Martin. *Quarks and Leptons: An Introductary Course in Modern Particle Physics*. (1984).

[5] I.A. Qattan *et al.* Precision rosenbluth measurement of the proton elastic form factors. *Phys. Rev. Lett.***94**, page 142301, (2005).

[6] J. Arrington. Implications of the discrepancy between proton form factor measurements. *Phys. Rev.C***69**, page 022201, (2004).

[7] V. Punjabi, C.F. Perdrisat. Proton elastic form factor ratios to $Q^2 = 3.5$ GeV^2 by polarization transfer. *Phys. Rev.C***71**, page 055202, (2005).

[8] O. Gayou *et al. Phys. Rev. Lett.***88**, page 092301, (2002).

[9] P.L. Chung, F. Coester. *Phys. Rev. D***44**, page 229, (1991).

[10] M.R. Frank, B.K. Jennings, G.A. Miller. *Phys. Rev. C***54**, (920), (1996).

[11] F. Cardarelli, S. Simula. *Phys. Rev. C***62**, page 65201, (2000).

[12] E. Pace, G. Salme, F. Cardarelli, S. Simula. *Nucl. Phys. A***666**, (33c), (2000).

[13] S. Boffi *et al. Eur. Phys. J.A***14**, (17), (2002).

[14] F. Gross, P. Agbakpe. *nucl-th*, v1:0411090, (2004).

[15] A.V. Afanasev, C.E. Carlson. Two-photon-exchange correction to parity-violating elastic electron-proton scattering. *Phys. Rev. Lett.***94**, page 212301, (2005).

[16] P.G. Blunden, W. Melnitchouk, J.A. Tjon. Two-photon exchange in elastic electron-nucleon scattering. *Phys. Rev. C***72**, page 034612, (2005).

[17] P.A.M. Guichon, M. Vanderhaeghen. How to reconcile the rosenbluth and the polarization transfer method in the measurement of the proton form factors. *Phys. Rev. Lett.***91**, (14), (2003).

[18] J. Arrington, W. Melnitchouk, J.A. Tjon. Global analysis of proton elastic form factor data with two-photon exchange corrections. *Phys. Rev. C***76**, page 035205, (2007).

[19] J. Arrington, W.K. Brooks, L.B. Weinstein *et al.* Beyond the born approximation: A precise comparison of e+p and ep elastic scattering in CLAS. submitted to PAC31.

[20] J. Arrington, V.F. Dmitriev, R.J. Holt. Two-photon exchange and elastic scattering of electrons/positrons on the proton. (proposal for an experiment at VEPP-3). *arXiv:nucl-ex/0408020*, 1(18), (2004).

[21] P.G. Blunden, W. Melnitchouk, J.A. Tjon. Two-photon exchange and elastic electron-proton scattering. *arXiv:nucl-th/0306076*, 2(21), (2003).

[22] Y.C. Chen, A. Afanasev, S.J. Brodsky. Partonic calculation of the two-photon exchange contribution to elastic electron-proton scattering at large momentum transfer. *Phys. Rev. Lett.***93**, page 122301, (2004).

[23] A.V. Afanasev *et al.* The two-photon exchange contribution to elastic electron-nucleon scattering at large momentum transfer. *Phys. Rev. D***72**, page 013008, (2005).

[24] L. Andivahiset *et al. Phys. Rev.D***50**, page 5491, (1994).

[25] J. Arrington. Extraction of two-photon contributions to the proton form factors. *Phys. Rev. C***71**, page 015202, (2005).

[26] J. Mar *et al. Phys. Rev. Lett.***21**, page 482, (1968).

[27] J. Arrington. Evidence for two-photon exchange contributions in electron-proton and positron-proton elastic scattering. *Phys. Rev. C***69**, page 032201, (2004).

[28] C.W. Leemann, D.R. Douglas, and G.A. Krafft. The continuous electron beam accelerator facility: CEBAF at the jefferson laboratory. *Annu. Rev. Nucl. Part. Sci.*, (2001).

[29] B.A. Mecking *et al.* The CEBAF large acceptance spectrometer (CLAS). *Nucl. Inst. and Meth. in Physics Research A*, page 503, (2003).

[30] K. de Jager. Future research program at jlab: 12 GeV and beyond. *Nucl. Phys. A 805*, (2008).

[31] D.I. Sober *et al.* The bremsstrahlung tagged photon beam in hall B at jlab. *Nucl. Inst. and Meth. in Physics Research A*, page 440, (2000).

[32] L. Weinstein. private communication, (2008).

[33] S. Christo. private communication, (2008).

[34] M.D. Mestayer *et al.* The CLAS drift chamber system. *Nucl. Inst. and Meth. in Physics Research A*, page 449, (2000).

[35] M.D. Mestayer. Choosing the correc combinaton of sense, field abf guard wire voltages. *CLAS NOTE*, 92:005, (1992).

[36] G.G. Adams *et al.* The CLAS cerenkov detector. *PACS*, J(95.55), (2000).

[37] E.S. Smith *et al.* The time-of-flight system for CLAS. *Nucl. Inst. and Meth. in Physics Research A*, page 432, (1999).

[38] M. Amarian *et al.* The CLAS forward electromagnetic calorimeter. *Elsevier*, (2000).

[39] D. Schott. private communication, (2008).

[40] GEANT detector Description and Simulation Tool. *CERN Genova*, (1993).

[41] GEANT4 User's Guide. *CERN Genova*, (2005).

[42] GEANT4 Physics Reference Manual. *CERN Genova*, (2005).

[43] Batch Farm User's Guide. http://wiki.jlab.org/cc/external/wiki/index.php/Batch-Farm-User27s-Guideintroduction.

[44] D. Kashy M. Zarecky. private communication, (2007).

[45] D. Tills. private communication, (2008).

[46] V. Blobel. The BOS system for CLAS detector. *CLAS Collaboration*, (1995).

[47] S. Stepanyan. Simple event builder (SEB) in the framework of recsis. http://www.jlab .org/ stepanya/seb-man.html.

[48] H. Baghdasaryan. *Measurements of Correlated Pair Momentum Distributions in 3He(e,e' pp)n with CLAS*. PhD thesis, Old Dominion University, (1995).

[49] E.S. Smith *et al.* Calibration of the CLAS TOF system. *CLAS-NOTE*, 99-011, (1999).

[50] D. Lawrence, M.D. Mestayer. CLAS drift chamber calibration: Software and procedures. *CLAS-NOTE*, 99-018, (1999).

[51] J. Lachniet. *A high precision measurement of the neutron magnetic form factor using the CLAS detector*. PhD thesis, Carnegie Mellon University, (2005).

[52] M. Holtrp. CLAS GEANT simulation. http://www.physics.unh.edu/maurik/gsim-info.shtml.

[53] L.W. Mo, Y.S. Tsai. Radiative corrections to elastic and inelastic ep and μp scattering. *Rev. of Modern Phys.***41**, page 205, (1969).

[54] M. Ungaro. private communication, (2009).

[55] M. Ungaro, J. Li. Procedure for drift chamber inefficiencies. *CLAS-NOTE*, 03-006, (2003).

VITA

MARYAM MOTEABBED

July 2, 1979	Born, Tehran, Iran
1998-2002	B. S., Physics Florida International University Miami, Florida
2002-2009	Doctoral Candidate in Physics Florida International University Miami, Florida
	Research/Teaching Assistant Florida International University Miami, Florida
2002-2009	Member of Users Group Thomas Jefferson National Accelerator Facility Newport News, Virginia
2004-2009	Member of CLAS Collaboration Thomas Jefferson National Accelerator Facility Newport News, Virginia
2008-2009	Member of Sigma-Xi Scientific Research Society
2007-2009	Member of Golden Key Honor Society
2007-2009	Member of American Physical Society (APS)

CONTRIBUTED TALKS

Moteabbed, M. (October 2008). *Measurement of Two-Photon Exchange Effects with CLAS.* APS Division of Nuclear Physics (DNP) meeting, Oakland, California.

Moteabbed, M. (June 2007). *Measurement of Two-Photon Exchange Effects with CLAS.* Hampton University Graduate Studies (HUGS) Workshop, Newport News, Virginia.

Moteabbed, M. (November 2003). *Feasibility Study of Weak Interactions in CLAS.* Southeastern Section of the American Physical Society (SESAPS) meeting, Wilmington, North Carolina.